

Ali Abdali

Gas-phase Synthesis of Silica Nanoparticles:

Reaction Kinetics, Synthesis and Characterization



Cuvillier Verlag Göttingen
Internationaler wissenschaftlicher Fachverlag



Gas-phase Synthesis of Silica Nanoparticles:
Reaction Kinetics, Synthesis and Characterization





*Gas-phase Synthesis of Silica Nanoparticles: Reaction Kinetics,
Synthesis and Characterization*

Von der Fakultät für Ingenieurwissenschaften, Abteilung Maschinenbau und

Verfahrenstechnik der

Universität Duisburg-Essen

zur Erlangung des akademischen Grades

eines

Doktors der Ingenieurwissenschaften

Dr.-Ing.

genehmigte Dissertation

von

Ali Abdali

aus

Manama, Bahrain

Referent: Prof. Dr. rer.-nat. Christof Schulz

Korreferent: Prof. Dr. rer.-nat. Burak Atakan

Tag der Mündlichen Prüfung: 04.11. 2013



Bibliografische Information der Deutschen Nationalbibliothek

Die Deutsche Nationalbibliothek verzeichnet diese Publikation in der Deutschen Nationalbibliografie; detaillierte bibliografische Daten sind im Internet über <http://dnb.d-nb.de> abrufbar.

1. Aufl. - Göttingen : Cuvillier, 2014

Zugl.: Duisburg-Essen, Univ., Diss., 2013

© CUVILLIER VERLAG, Göttingen 2014

Nonnenstieg 8, 37075 Göttingen

Telefon: 0551-54724-0

Telefax: 0551-54724-21

www.cuvillier.de

Alle Rechte vorbehalten. Ohne ausdrückliche Genehmigung des Verlages ist es nicht gestattet, das Buch oder Teile daraus auf fotomechanischem Weg (Fotokopie, Mikrokopie) zu vervielfältigen.

1. Auflage, 2014

Gedruckt auf umweltfreundlichem, säurefreiem Papier aus nachhaltiger Forstwirtschaft.

ISBN 978-3-95404-704-8

eISBN 978-3-7369-4704-7



Acknowledgements

It would not have been possible to write this doctoral thesis without the support of the kind people around me, only some of whom is possible to particularly mention here.

Foremost, I would like to thank my supervisors Prof. Dr. Christof Schulz and Dr. Hartmut Wiggers for providing me the opportunity to complete my PhD at the University of Duisburg-Essen and for their guidance, support and patience during my scientific work at the Institute for Combustion and Gasdynamics.

Above all, I would like to thank my wife Dr. Khadijeh Mohri for her personal support, English language corrections and great patience at all times. My parents have given me their unequivocal support throughout, for which my mere expression of gratitude does not suffice.

I am most grateful to Dr. Mustapha Fikri, Mohammad Aghsaee and Metehan Bozkurt for their help in the shock tube lab, Dr. Hans Orthner, Dr. Ingo Plümel, Dr. Anoop Gupta and Dr. Alessandro Faccinnetto in the nanoparticle lab, Prof. Dr. Thomas Dreier and Dr. Christian Hecht for their support in the laser diagnostics lab and Dr. Irenäus Wlokas and Claudia Weise for the CFD support. Thanks to my colleagues at the Institute for Combustion and Gasdynamics for the excellent teamwork and great time. I am also thankful to the technical team which includes Natascha Schlösser, Beate Endres, Birgit Nelius, Jörg Albrecht, Ludger Jerig and Dieter Hermann for providing valuable assistance. Without the help of these colleagues no experiment could be carried out.

Special gratitude goes to the GIP-project team, especially Dr. Manfred Dannehl from EVONIK Industries AG. I would also like to acknowledge the financial support from Deutsche Forschungsgemeinschaft (DFG, No. PAK 75).





Contents

1.	Introduction.....	1
2.	State of the art	4
3.	Theoretical background of nanoparticle synthesis in the gas phase.....	8
3.1.	Gas-phase kinetics and mechanism of TEOS decomposition	9
3.2.	Particle formation and growth.....	12
3.2.1.	Homogeneous nucleation	12
3.2.2.	Coagulation, coalescence and agglomeration	14
4.	Experiment	16
4.1.	Precursor delivery systems	16
4.1.1.	Mixing vessel method	16
4.1.2.	Pressure-controlled mixing (bubbler system).....	17
4.1.3.	Controlled evaporation and mixing (CEM).....	18
4.2.	Gas-phase reactors.....	19
4.2.1.	Hybrid microwave-plasma hot-wall reactor	19
4.2.1.1.	Overview of hot-wall reactors	19
4.2.1.2.	Overview of microwave-induced plasma reactors.....	20
4.2.1.3.	Microwave-plasma hot-wall reactor.....	23
4.2.2.	Premixed low-pressure H ₂ /O ₂ /Ar flame reactor	24
4.2.2.1.	Overview of flame reactors	24
4.2.2.2.	Experimental setup of the premixed low-pressure H ₂ /O ₂ /Ar flame reactor	25
4.2.2.3.	Particle mass spectrometer (PMS).....	26
4.2.3.	Gas-dynamically-induced particle synthesis	30
4.2.3.1.	3D-Simulation of the production of gas-phase synthesized nanoparticles in the reactor	31
4.2.3.2.	Experimental study of the mixing process of the injected precursor with the reactor gases.....	33
4.2.3.3.	Studying the precursor chemistry and the particle growth	33



4.2.3.4.	Supersonic expansion and water quenching system.....	34
4.2.3.5.	Sampling technique of particles from the reactor.....	34
4.3.	Shock-tube experiments	35
4.3.1.	Principles of shock-tube experiments.....	35
4.3.2.	Shock-tube experiments to determine the ignition delay time of TEOS and HMDSO	38
4.3.3.	Time-of-flight mass spectrometer (TOF-MS)	41
4.3.3.1.	Theory of time-of-flight mass spectrometry	41
4.3.3.2.	TOF-MS for kinetics investigations at the shock tube	44
4.4.	Multiline NO-LIF thermometry in flow reactors	46
4.4.1.	Fundamentals of multiline NO-LIF thermometry.....	46
4.4.2.	Multiline NO-LIF-technique at a low-pressure premixed flame reactor.....	48
4.4.3.	Multiline NO-LIF technique at the microwave-plasma reactor	49
5.	Results and discussion.....	50
5.1.	Kinetics studies of precursor decomposition and oxidation in shock-tube experiments.....	50
5.1.1.	Tetraethoxysilane (TEOS)	50
5.1.1.1.	Studying the decomposition kinetics of TEOS using TOF-MS at the shock tube	50
5.1.1.2.	Ignition delay times of TEOS	59
5.1.2.	Hexamethyldisiloxane (HMDSO)	63
5.1.2.1.	Studying the decomposition kinetics of HMDSO in the shock tube via TOF-MS	63
5.1.2.2.	Atomic Resonance Absorption Spectroscopy (ARAS) of silicon atoms.....	66
5.1.2.3.	The influence of oxygen on the initial gas mixture.....	68
5.1.2.4.	Ignition delay times of HMDSO.....	70
5.1.2.5.	Simultaneous measurements of OH* chemiluminescence and TOF-MS ...	71
5.2.	Microwave plasma reactor.....	73
5.2.1.	Temperature imaging in the microwave-plasma reactor using multiline NO-LIF thermometry	73



5.2.1.1.	Investigating the influence of the main parameters on the plasma temperature	73
5.2.1.2.	Investigation of the plasma temperature by injecting TEOS	77
5.2.1.3.	Investigation of particle formation in the microwave-plasma hot-wall reactor	80
5.3.	Low-pressure premixed H ₂ /O ₂ /Ar flame reactor	88
5.3.1.	Investigation of silica particle formation in the H ₂ /O ₂ /Ar flame reactor using TEOS.....	88
5.3.1.1.	Influence of the height above burner (<i>HAB</i>) on the mean particle size and particle size distribution.....	90
5.3.1.2.	Influence of TEOS concentration on the mean particle size.....	92
5.3.1.3.	Influence of the equivalence ratio ϕ on the mean particle size	93
5.3.2.	Investigation of silica particle formation in the H ₂ /O ₂ /Ar flame reactor with HMDSO	95
5.3.2.1.	Influence of the height above burner (<i>HAB</i>) on the particle size and the particle size distribution.....	96
5.3.2.2.	Influence of the HMDSO concentration on the mean particle size.....	98
5.3.2.3.	Influence of the equivalence ratio on the mean particle size	99
5.4.	Gas-dynamically induced particle synthesis (GIP reactor).....	101
5.5.	Comparison between TEOS and HMDSO	102
5.5.1.	Ignition delay times	102
5.5.2.	Investigation of the particle formation in the flame reactor.....	103
6.	Conclusions.....	105
7.	Recommendation for future work	108
8.	References.....	109
9.	List of own publications	120



List of symbols, abbreviations and acronyms

Latin symbols

A	Pre-exponential factor
A^*	critical cross section area
b_K	Distance between the deflection capacitors
d	Length of the flight path
d_p	Particle diameter
e	Electronic charge
E	Field strength
E_p	Potential energy
E_K	Kinetic energy
G_V	Free energy per unit volume
f	Focal length
f	Frequency of the grid voltage
I	Electrical current
k	Rate coefficient
k_B	Boltzmann constant
l_G	Distance between grids
l_K	Length of deflection capacitor
l_p	Package length
L_{PMS}	Distance between aperture and deflection capacitor
m	Mass
m_p	Particle mass
M	Mach number
M	Molar mass
N	Particle number
N_A	Avogadro's number
N_n	Molar concentration of nuclei
p	Pressure
p_s	Saturation pressure
P_{MW}	Microwave power
q	Particle charge
r	Spherical nucleus radius
r^*	Critical nucleus radius
R	Universal gas constant
S	Saturation ratio
S_0	Ground state energy level
S_1	Excited energy level
t	Time



T	Temperature
T_e	Electron temperature
T_i	Ion temperature
U	Electric potential difference (Voltage)
U_K	Deflection Voltage
v	Velocity
v_{iw}	Incident shock wave velocity
v_{CS}	Contact surface velocity
v_p	Particle velocity
V_p	Particle volume
x_p	Particle size
z	Number of electron charges

Greek symbols

ΔG	Change in free energy
ΔG^*	Critical free energy
Δt_{ms}	Available time for measurement
β	Collision frequency function
λ	Wave length
ϕ	Equivalence ratio
σ_g	Geometric standard deviation
τ	Ignition delay time

Abbreviations and acronyms

ARAS	Atomic resonance absorption spectroscopy
BET	(Brunauer, Emmett, Teller)
CEM	controlled evaporator mixer
CFD	Computational fluid dynamic
CMD	Count mean diameter
EI	Electron impact
FTIR	Fourier transform infrared
GDE	General dynamics equation
GIP	Gas-dynamically induced particle synthesis
HAB	Height above burner
HMDSO	Hexamethyldisiloxane
HRR	High repetition rate
ICCD	Intensified charge-coupled device
LIF	Laser induced fluorescence
MCP	Microchannel plate



MFC	Mass flow controller
MS	Mass spectrometry
MW	Microwave
OMCTS	Octamethylcyclotetrasiloxane
PDF	Probability density function
PMS	Particle mass spectrometer
SAS	Scale adaptive simulation
scm	Standard cubic centimeter per minute
slm	Standard liter per minute
SSA	Specific surface area
TEOS	Tetraethoxysilane
TEM	Transmission electron microscope
TMS	Tetramethylsilane
TOF	Time of flight



Zusammenfassung

In dieser Arbeit wurden die Kinetik des Zerfalls von Tetraethoxysilan (TEOS) und Hexamethyldisiloxan (HMDSO) und von Bildung und Wachstum von Siliziumdioxid-Nanopartikeln in der Gasphase untersucht. Die Zerfallskinetik wurde in Stoßwellenrohrexperimenten mithilfe hochrepetitiver Flugzeit-Massenspektrometrie (TOF-MS) untersucht. Während beim Zerfall von TEOS die Bildung von Si(OH)_4 beobachtet wurde, zeigten die Massenspektren während des HMDSO-Zerfalls die Bildung mehrerer Silizium-haltiger Spezies, wie Si-Atome, SiO und SiCH_3 . Die Verbrennung von TEOS und HMDSO in sauerstoffhaltiger Atmosphäre wurde durch die Bestimmung der Zündverzugszeiten untersucht. Die stark temperaturabhängigen Zündverzugszeiten von TEOS und HMDSO wurden mithilfe des Arrhenius-Gesetzes beschrieben.

Die Bildung und das Wachstum von SiO_2 -Nanopartikeln aus TEOS und HMDSO wurden in einer Kombination von Mikrowellenplasma- und Heißwandreaktor und in einem Niederdruck- $\text{H}_2/\text{O}_2/\text{Ar}$ -Flammenreaktor mit Hilfe in-situ und ex-situ Messverfahren untersucht. Partikelgrößenverteilungen wurden mithilfe der Partikelmassenspektrometrie bestimmt. Die räumliche Verteilung der Gasphasentemperatur wurde mit Multilinienn-NO-LIF-Thermometrie gemessen.

Die vorliegende Arbeit liefert umfangreiche Daten und neues Verständnis für die zerfallskinetik von TEOS und HMDSO sowie Partikelbildung und -Wachstum von SiO_2 -Nanopartikeln aus der Gasphase. Diese Daten können als Eingangsgrößen für die Simulation von Reaktionssystemen und somit für die Konstruktion von Gasphasenreaktoren zur Herstellung hochspezifischer Nanomaterialien eingesetzt werden.



Abstract

In this thesis the gas-phase kinetics of the decomposition of tetraethoxysilane (TEOS) and hexamethyldisiloxane (HMDSO) and the formation and growth of silica nanoparticles were studied. The kinetics study was carried out in shock-heated gases with species measurements by high-repetition-rate time-of-flight mass spectrometry. The mass spectra indicate the formation of $\text{Si}(\text{OH})_4$ from the decomposition of TEOS while during HMDSO decomposition several Silicon-containing species were found, such as Si atoms, SiO and SiCH_3 . The ignition-delay time of the precursors in oxygen-containing bath gases was studied by observing the OH^* emission signal behind the reflected shock wave. The ignition delay times of TEOS and HMDSO are strongly temperature dependent and the Arrhenius parameters were determined.

Silica-particle formation and growth from TEOS and HMDSO were investigated in a hybrid microwave-plasma hot-wall reactor and a low-pressure premixed $\text{H}_2/\text{O}_2/\text{Ar}$ flame reactor by in-situ and ex-situ measurements. Particle sizes distributions were determined by particle mass spectrometry and the spatial gas-phase temperature distribution was measured with multi-line NO-LIF thermometry.

The present research work provides data and new understanding of TEOS and HMDSO decomposition kinetics and particle formation and growth of silica nanoparticles in the gas-phase. These data can be used as input for computational fluid dynamics simulations and hence for the design of reactors for the gas-phase synthesis of highly specific nanoparticles.



1. Introduction

Nanotechnology is proving to play a vital role in many disciplines and can be considered the key of future technologies due to the novel properties of materials in the nanosize range, between 1–100 nm. Nanoparticles are viewed by many as fundamental building blocks of nanotechnology. They are the starting point for many ‘bottom-up’ approaches for preparing nanostructured materials and devices. As such, their synthesis is an important component of rapidly growing research efforts in nanoscale science and engineering [1]. Nanomaterials and ultrathin functional coatings of nanoparticles will determine the utility of many future products such as super-hard materials [2], super fast computers, dirt-repellent surfaces, new cancer treatments, scratch proof coatings and environmentally friendly fuel cells with highly effective catalysts [3, 4]. The properties of materials change as their size approaches the nanoscale and as the percentage of atoms at the surface of a material become significant. It is often observed that the physical (e.g. melting point, conductivity, magnetism) and chemical (e.g. catalytic activity) properties of nanomaterials change depending on the particle size [5]. Most of the worldwide production of nanomaterials on an industrial scale can be assigned to carbon black, silica and titania. Silica nanoparticles have a large range of practical applications. They are widely used as fillers in plastics and coatings to improve material properties such as hardness, tensile strength, abrasion resistance and thermal stability. In particular, applications with demands for high transparency require silica particles with a specific size, morphology, and surface coating [4, 6]. Recent discoveries have reported the use of silica nanoparticles in biotechnology for bio-sensing and drug delivery [7, 8].

Moreover, besides the particle size the quality of the particles such as the particle size distribution and agglomeration index also play an important role on the material properties. Therefore, synthesis of highly defined nanoparticles with specific particle size, size distribution and morphology is desired. Particle agglomeration that commences in the end region of gas phase reactors is an important quality index for a number of applications. For example, agglomerated nanostructured particles are needed for the manufacture of fillers and catalysts [9]. However, if particle agglomeration could be avoided, several advantages could be achieved [10, 11]. Non-agglomerated nanoparticles are essential for many applications such as pigments, nanocomposites e.g. batteries for higher capacity, porous electrodes for energy storage and electronics [9, 12].

Highly specified nanoparticles that have a low agglomeration index and narrow particle size distribution are usually produced using wet-chemistry. However, wet-chemistry requires several processing steps in addition to batch processing and this reduces the production rate and increases the price [13]. Furthermore, these particles may contain impurities from syn-



thesis and post-processing [14]. Gas-phase synthesis has the advantages of allowing continuous production of pure nanoparticles, easy processing control and possibility to be scaled up from laboratory to industrial scale reactors [15, 16]. The two main disadvantages of gas-phase synthesized particles, especially in conventional large-scale production, is the broad size distribution which is due to the inhomogeneous flow conditions, and the large degree of end-product aggregation that is mainly due to the low cooling rates of the product [17].

It has been found that fast cooling in gas phase reactors enables non-agglomerated nanoparticles, with a narrow particle size distribution, to be produced [6]. Based on this concept a novel gas-phase reactor was built for mass production of highly specified metal-oxide nanoparticles within the scope of the project “Gas-dynamically induced particle synthesis”, funded by the German Research Foundation (DFG). The key of this novel process is to provide one-dimensional conditions in the reactor for particle growth with nearly instantaneous decomposition of the precursor, an adjustable time for particle growth and high cooling rates of $-dT/dt = 10^7$ K/s in order to suppress agglomeration [18]. The realization of this concept required several studies such as numerical simulation of the particle formation and growth with integrated reaction kinetics of the precursor [19]. The simulations required detailed experimental data of the precursor decomposition, particle formation and particle growth kinetics which were carried out as part of the work in this thesis.

The primary aim of this work was to investigate the influence of the precursor chemistry on the particle size, size distribution and morphology of the final product. It has been found that the decomposition of a precursor at high temperatures has a negligible influence on the final product [20]. This is due to the very short time scales of the precursor chemistry at the relevant temperature compared to the time required for particle formation and growth. On the other hand, the molecular structure of the monomer that is produced from the precursor decomposition can strongly influence the mechanism of particle formation and growth. In this content, two different silicon containing metalorganic precursors with different molecular structures were chosen for investigation. Tetraethoxysilane (TEOS) and Hexamethyldisiloxane (HMDSO) as halide-free and inexpensive precursor materials are subject to growing interest for particle formation as well as for Chemical Vapor Deposition (CVD) from the gas phase. In this work the precursor chemistry as well as the particle formation were individually studied and the outcome from both studies were then compared. Furthermore, the results of this work provided essential data for the CFD-simulations and construction of the reactor for the Gas-dynamically Induced Particle or so called “GIP reactor”.

In this thesis the gas-phase kinetics of TEOS and HMDSO decomposition were investigated in shock tube facilities due to their capacity to instantaneously heat a gas mixture within a wide range of temperatures and pressures that cannot be obtained in other types of testing facili-



ties. The objective of the shock tube experiments was to study the kinetics of the precursor decomposition and oxidation at high temperatures. The thermal decomposition of TEOS and HMDSO was achieved by combining the shock tube with a time-of-flight mass-spectrometer (TOF-MS). This system was established for the study of complex reaction systems. The fast detection method of high-repetition-rate TOF-MS provides time resolved information about the change in composition of the investigated mixture. Furthermore, the ignition delay times of TEOS and HMDSO were investigated by measuring the onset of OH*-chemiluminescence behind the reflected shockwave in shock tube experiments. Because gas-phase synthesis for nanoparticle formation is often based on flame-synthesis that contains high moisture levels in the flame off-gas, the ignition delay times of TEOS and HMDSO have been investigated in dry as well as moist synthetic air.

Since the focus of these experiments was to investigate the formation and growth of silica nanoparticles, a microwave-supported plasma reactor and a premixed H₂/O₂/Ar-flame reactor were chosen. These two reactors can provide high temperatures at the initial reaction step. The experiments were performed at reduced pressure (30 –70 mbar) to stretch the spatial axis for a detailed analysis of particle formation and growth. The particle formation and growth of silica nanoparticles from TEOS and HMDSO were investigated by measuring the particle size, particle size distribution and particle morphology by systematically varying the main reactor parameters such as temperature, precursor concentration and residence time. Several methods were used in this thesis for in-situ and ex-situ particle characterization such as Transmission Electron Microscopy (TEM) and Particle Mass Spectrometry (PMS).

Due to the lack of information on the microwave-plasma temperature and the influence of the reactor parameters, e.g., reactor pressure and microwave power, the multiline NO-LIF thermometry technique was applied to measure the gas temperature under different conditions. The data from these measurements can support better understanding and interpretation of particle formation and growth in the microwave-plasma reactor.



2. State of the art

Silicon (Si) is one of the most abundant elements in the Earth's crust, second only to oxygen. In nature silicon is combined with oxygen, in the form of silicon dioxide which is commonly referred to as silica and silicate. Silica is one of the most important silicon compounds occurring in nature as sand and quartz [21]. Bulk silica is used primarily in the production of glass, fused quartz and crystal. Today, through the revolution of nanotechnology, silica nanoparticles are considered an important material for a wide range of practical applications such as additives in plastic and rubber to improve their mechanical properties. Rubber toughening [22] and scratch resistance of polymer coating [23] are some examples. For environmental applications silica nanoparticles have been used as an additive in concrete to reduce the cement content in concrete mixtures [24]. More recently, mesoporous silica nanoparticles (MSN) have gained attention for their potential as controlled release systems and vehicles for the delivery of chemotherapeutics due to their high surface areas, large cavity volumes, and ability to be functionalized with biomolecules for the targeting of specific tissue populations [25, 26]. Such sensitive applications require particles of highly specific size, morphology and surface characteristics. In order to design a new reactor and to control the particle properties, it is essential to understand the detailed precursor kinetics as well as the mechanism of formation and growth of these nanoparticles.

Nanoparticles are generally produced using one of the two so-called “bottom-up” synthesis methods in industry. The first method is liquid-phase synthesis where chemical reactions are applied to solvents. This leads to a colloid, in which the resulting nanoparticles can be stabilized against aggregation by surfactants or ligands. Reviews in this area have been presented by Grieve et al. [27], Trindade et al. [28], and Murray et al. [29]. The second method is gas-phase synthesis which is the subject of this thesis. Gas-phase processes for particle synthesis are usually continuous processes, while liquid-based synthesis processes are often performed in a batch form. Moreover, gas-phase processes are generally purer than liquid-based processes since even the most ultra-pure water contains traces of minerals, detrimental to electronic grade semiconductors [16]. Flame processes are by far the most widely used ones for the manufacture of commercial quantities of nanoparticles. The most important products today are carbon black (Cabot, Columbia), fumed silica (Cabot, EVONIK), pigmentary titania (DuPont, Kerr-McGee) and optical fibers (Heraeus, Sumitomo) [30]. Nonetheless, a scientific understanding of gas-phase synthesis of particles remains a major challenge even though a variety of scientific communities have studied it closely. Swihart [31] critically reviews the state of the art in vapor synthesis of materials, focusing on methods and processes. Strobel et al. [32] review how flame aerosol technology can be used to make various sophisticated materials for sensors, biomaterials, electroceramics, and even nutri-



tional supplements. Biskos and colleagues [33] review aerosol generation and characterization methods for nanoparticles. Athanassiou and colleagues [34] show how ceramics and even metals are made in scalable flame aerosol reactors.

Fumed silica is the third largest industrial aerosol commodity by value and the fourth largest by volume [35]. The dominant route for synthesis of fumed SiO_2 relies on the oxychloride process for oxidizing various silica precursors, especially SiCl_4 . Recently, the interest for tetraethoxysilane (TEOS) and hexamethyldisiloxane (HMDSO) as halide-free and inexpensive materials is growing for gas-phase production of silica. Many experimental and theoretical papers have been involved with the thermal decomposition of TEOS in inert conditions. Herzler et al. [36] investigated the thermal decomposition of TEOS in a heated single-pulse shock tube and analyzed the reactants and final stable products. The distribution of gaseous products was monitored by gas chromatography, and the main gaseous stable by-products were found to be ethylene and ethanol. The only source of thermochemical data for TEOS originates from Kee et al. [37] who calculated species enthalpies of some silicon-based species. In the same manner, Kraft and co-workers [38-40] generated thermochemical data for TEOS. Recently, Kraft proposed a reduced kinetics model and particle inception pathways for the flame synthesis of silica nanoparticles from TEOS. They show that the main product of TEOS decomposition is silicic acid ($\text{Si}(\text{OH})_4$), which forms silica nanoparticles by condensation reactions [38]. Chu et al. [41] also studied the thermal decomposition of TEOS in a static system with species detection by Fourier-transform infrared spectroscopy (FTIR) in the temperature range between 700 and 820 K. The main by-product they found was ethanol and the decomposition could be described assuming a six-ring elimination mechanism. Takeuchi et al. [42] studied the thermal decomposition of TEOS in a low-pressure CVD reactor at 13 Pa and 950 K. Reaction products as well as the rate of film growth were determined and fitted with a new model. This model quantitatively accounts in the first step for the ethylene formation and the condensation of silanol with TEOS, which finally leads to the formation of ethanol as a stable by-product. Chagger et al. [43] were first to investigate HMDSO combustion in opposed diffusion flames and proposed a reaction mechanism for the formation of SiO_2 . Despite the intensive use of this precursor in industry for materials synthesis, there is few or no information about the kinetics and thermochemistry of HMDSO. Wavhal et al. [44] have studied the gas-phase species of HMDSO decomposition in a plasma using optical emission spectroscopy, whereas Carles et al. [45] used a movable mass spectrometer. The production of both, ionized and neutral fragments, occurs through charge transfer between the Ar^+ ion and HMDSO that can be followed by subsequent ion-molecule reactions and the dissociative recombination of the fragment ions. Carles et al. [45] measured the absolute rate coefficients for the dissociative recombination of hexamethyldisiloxane (HMDSO) and pentamethyldisiloxane (PMDSO) cations with electrons. Their results show also several Si-



containing molecules produced from HMDSO decomposition such as CH_3SiH_2 , $(\text{CH}_3)_2\text{SiH}$ and $(\text{CH}_3)_3\text{Si}$. Recently, Burkert et al. [46] detected the emission of several excited species such as OH^* , CH^* , Si^* and SiO^* of a rich HMDSO/propane/air flame. They have concluded that up to heights of 10 and 40 mm, Si and SiO can be detected, respectively.

Various studies have been conducted on the synthesis of silica nanoparticles from the gas phase using different methods. Ulrich and his co-workers [47, 48] conducted some of the earliest work on the characterization of silica particle formation in flames. Their work focused on the agglomeration processes following the formation of silica particles. Using silicon tetrachloride as the silicon source in a variety of burner configurations, their work suggested that nucleation and surface growth effects were not crucial for controlling the final particle size. Particle growth was governed by coagulation effects. More recently Ahn et al. [49] and Jang [50] have investigated the synthesis of silica nanoparticles from TEOS in diffusion flames, while Goortani et al. [51] have worked on the formation of SiO_2 nanoparticles from quartz in an RF-plasma reactor. They all found that, depending on temperature and precursor concentration, silica nanoparticles with different morphologies and sizes arise along the reaction coordinate ranging from spherical, spatially separated particles to large agglomerates and aggregates. Abdali et al. [52] studied silica particle formation in a microwave plasma reactor using gaseous TEOS as a precursor. They used a hot-wall furnace to extend the residence time in the high temperature region. Their results indicate that the silica particles are dispersed in the gas phase, whereas the same particles start to aggregate in the filter downstream of the reactor. They suspect that this is due to the high number of hydroxyl-groups on the particles' surfaces. In the same microwave-plasma reactor Hecht et al. [53] measured the gas temperature distribution in the plasma using multi-line NO-LIF thermometry.

Zachariah and Semerjian [54] found that the choice of precursor affects the mechanism of particle formation and growth. They carried out *in situ* light scattering dissymmetry measurements of the particle size and number density in a counter-propagating non-premixed flame with silane and HMDSO as precursor. Their experiments showed that particle nucleation sets in earlier when using silane compared to organometallics like HMDSO or TMS (tetramethylsilane) but reaches nearly the same number concentration by coagulation further downstream. Briesen et al. [55] studied the effect of the silicon precursor source concentration and oxidant composition on the specific surface area of nanostructured silica particles produced in a non-premixed and premixed $\text{CH}_4/\text{O}_2/\text{N}_2$ flame reactor. For these experiments, hexamethyldisiloxane (HMDSO), octamethylcyclotetrasiloxane (OMCTS) and SiCl_4 were used. They found that particles generated by oxidation of organometallic compounds tend to have a smaller specific surface area than the ones made from SiCl_4 as precursor. This is attributed



primarily to the increase of the flame temperature by the additional fuel coming from the organometallic compound.

Several studies have shown that the mechanisms of the particle growth depend on the reactor environment and the temperature history. As Ahn et al. have shown, an initially high temperature seems to support the formation of non-agglomerated and spherical particles. Tsantilis and Pratsinis [6] calculated that fast cooling results in soft agglomerates while in systems with low cooling rates hard agglomerates are formed. Kusters and Pratsinis [1] showed that an increase in the operation temperature generally increases the reaction rate but decreases the surface tension. This provided an excellent way to improve monodispersity. However, they also showed that a high reaction rate and a low surface tension resulted in larger aerosol concentrations and smaller particle sizes. Xiong et al. [56] showed, in theory, that electrical charges during the gas-phase particle generation process reduce the average particle size and narrow the size distribution of particles. Furthermore, Schiel et al. [57] and Reuter et al. [58] studied the influence of the hot-wall temperature on the particle charge, so-called thermionization, and investigated its effect on the particle growth. Their results illustrated that the increase in particle charge that is accompanied with increasing hot-wall temperature hinders particle collisions. Ehrman et al. [59] calculated the characteristic sintering time of silica (for viscous flow) from property data while accounting for the effect of hydroxyl groups. Xiong et al. [60] and Ehrman et al. [59] examined the effects of temperature on the characteristic sintering time of the silica particles. Recently Goertz et al. [61] studied the influence of water vapor concentration on the structural changes of SiO₂ aerosol nanoparticle agglomerates during tempering at a temperature range of 1100–1500 K. They found that the presence of water vapor in the carrier gas strongly accelerated the kinetics.

3. Theoretical background of nanoparticle synthesis in the gas phase

The synthesis of highly specified nanoparticles with specific control of the nanoparticle size and morphology, particle size distribution and agglomeration index requires good theoretical and experimental knowledge of the underlying process mechanisms and their influencing parameters. This can be studied in two separate steps that occur as a subsequent process in particle synthesis: the initiating precursor chemistry, and particle formation and growth. Figure 3.1 gives an overview of the mechanism of the gas-to-particle conversion using TEOS as a precursor for the production of silica nanoparticles. Providing a certain amount of energy that is higher than the activation energy is essential to initiate the reactions. The energy source can be for example a flame, electric heating or microwave discharge. The decomposition of the precursor produces Si-containing molecules (monomers). Supersaturation of monomers leads to condensation or nucleation and subsequent particle formation and growth through surface reactions and coagulation. A comprehensive understanding of the synthesis process of silica nanoparticles requires the successful coupling of the theoretical as well as experimental details of the precursor kinetics in the gas-phase and the dynamics of the particle formation and growth.

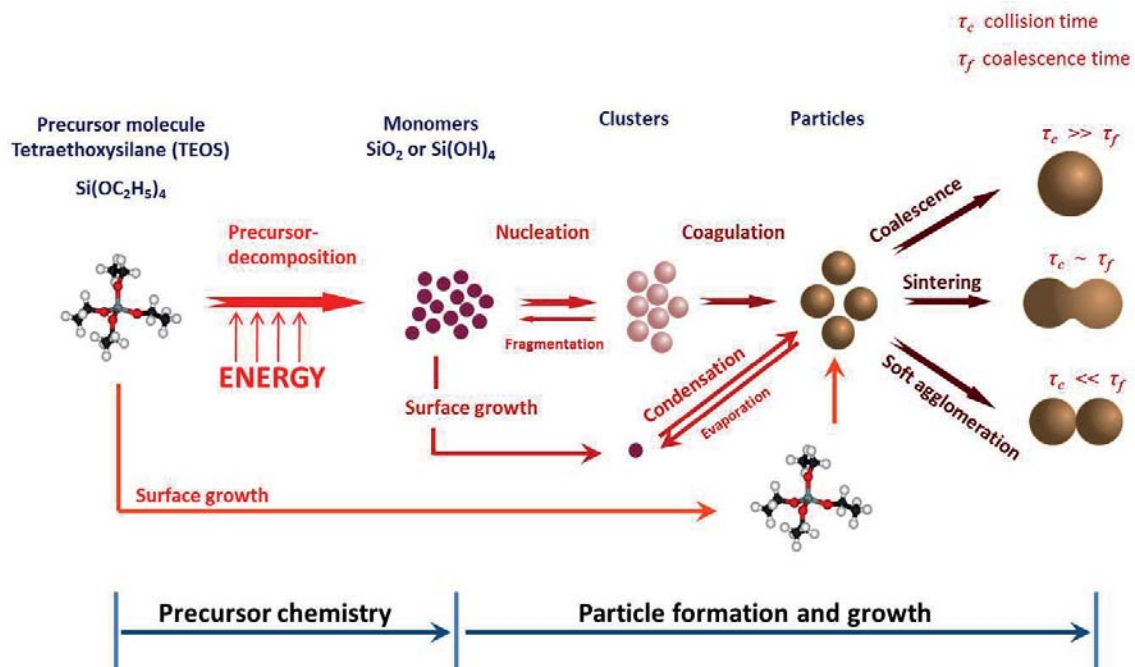


Figure 3.1: Simplified scheme of the gas-to-particle conversion of silica nanoparticles using TEOS as a precursor



3.1. Gas-phase kinetics and mechanism of TEOS decomposition

Particle synthesis depends on various process parameters such as temperature, pressure and flow properties. A deep understanding of the decomposition kinetics of the precursor and the subsequent particle formation and growth is essential for tailor-made nanoparticles. It is always beneficial to separate the chemistry from the transport processes. Knowledge about reaction kinetics is therefore necessary to understand the underlying mechanisms which can be further implemented into computer simulations for particle synthesis optimization. These can also support the design of new reactors or the improvement of existing reactors. On the other hand, these data are essential to understand under which conditions, e.g. temperature, the reaction should be initiated to control the synthesis.

Based on experimental and theoretical studies of the precursor chemistry, the reaction mechanism as well as the reaction pathways can be illustrated in a kinetics model. Detailed kinetics models represent the molecular interactions that occur when chemical bonds are broken and new chemical compounds are formed. Such kinetics models are sometimes referred to as micro-kinetics models. Kinetics models that are based on elementary reactions offer the best accuracy and reliability. Moreover, knowledge of a specific elementary reaction can be universal for completely different operating conditions and in different species mixtures. Thus, knowledge acquired about reactions at this level accumulates as a re-usable asset. In contrast, more approximate methods (e.g., “operational” kinetics) have the parameters determined strictly by fitting to a set of experimental data and have very limited applicability. Although global reaction expressions can be included in detailed kinetics mechanisms, more fundamental expressions provide more accuracy and extensibility.

For TEOS two kinetics models were mainly developed. Herzler et al. [36] studied the decomposition of TEOS using a single-pulse shock tube and analyzed the reactants and final stable products using gas chromatography. This well-established method is especially suited for studying the quantitative detail of the initial unimolecular decomposition process of large polyatomic compounds [62]. Herzler et al. presented a fully-irreversible kinetics scheme for the decomposition of TEOS. The main products were shown to be ethanol and ethylene. They proposed a reaction pathway involving the decomposition of TEOS to form silicates and silyl acids and the rates were determined through fitting to their experimental data. This model predicted the activation barrier for the formation of ethanol and silicate from silanol to be less than 200 kJ/mol. Figure 3.2 shows the reaction pathway of the decomposition mechanism of TEOS. Each arrow in the kinetics model represents an elementary reaction of a silicon intermediate. The thicker arrows represent higher decomposition rates than the thinner ones. This kinetics model shows that the main Si-containing product from the decomposition of TEOS is SiO_2 . The gaseous SiO_2 molecules are highly supersaturated, leading

to very fast nucleation reducing the concentration of SiO_2 molecules, and subsequent silica particle formation. Therefore, they are likely to exist only in very low concentrations and at very short times.

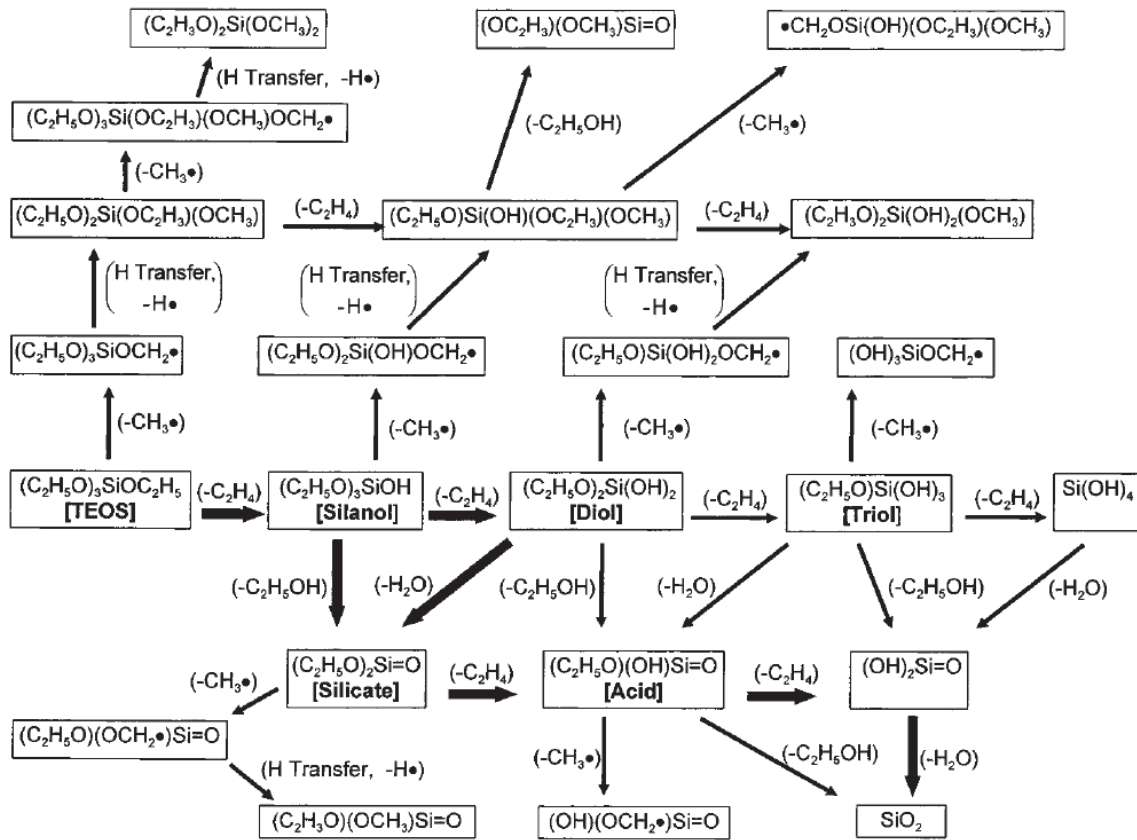


Figure 3.2: Herzler kinetics model of TEOS decomposition mechanism [36]

Recently, Kraft and co-workers [38] proposed a new kinetics model and a novel inception pathway for the flame synthesis of silica nanoparticles from TEOS. They developed the kinetics model for the decomposition of TEOS by generating reactions involving species that were reported in high concentrations at equilibrium such as ethoxy and methoxy silane. The identification of the main reaction pathways were performed by flux and sensitivity analyses. As a result they found that the main product of TEOS decomposition is silicic acid ($\text{Si}(\text{OH})_4$). They also reduced the kinetics model by determining the level of importance of each species and retaining only the important ones to increase computational efficiency. Furthermore, a new particle inception and a surface growth were incorporated into the particle model in which particles form and grow through interaction of $\text{Si}(\text{OH})_4$ monomers. The further coagulation and sintering of particles are also included in their model.

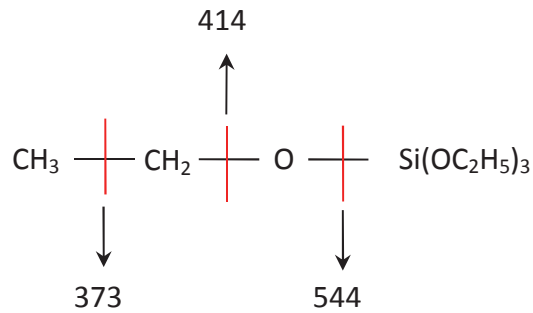


Figure 3.3: Bond energies in TEOS in kJ/mol [63]

Based on the results from equilibrium calculations and the dissociation energies of different bonds in the TEOS molecule (cf. Figure 3.3 and [63]), a TEOS decomposition mechanism that leads to production of $\text{Si}(\text{OH})_4$ was systematically developed. The main elementary reaction pathway proposed by Herzler et al. [36] is also included in the mechanism of Kraft as an alternative route for TEOS decomposition that leads to formation of SiO_2 in the gas phase. The resulting flux diagram from the kinetics modeling is illustrated in Figure 3.4. The thickness of each arrow in this diagram is proportional to the flux associated with the corresponding reaction. Figure 3.4 shows that the net elemental flux of Si in the direction of $\text{Si}(\text{OH})_4$ formation is appreciably higher than in the direction of SiO_2 formation.

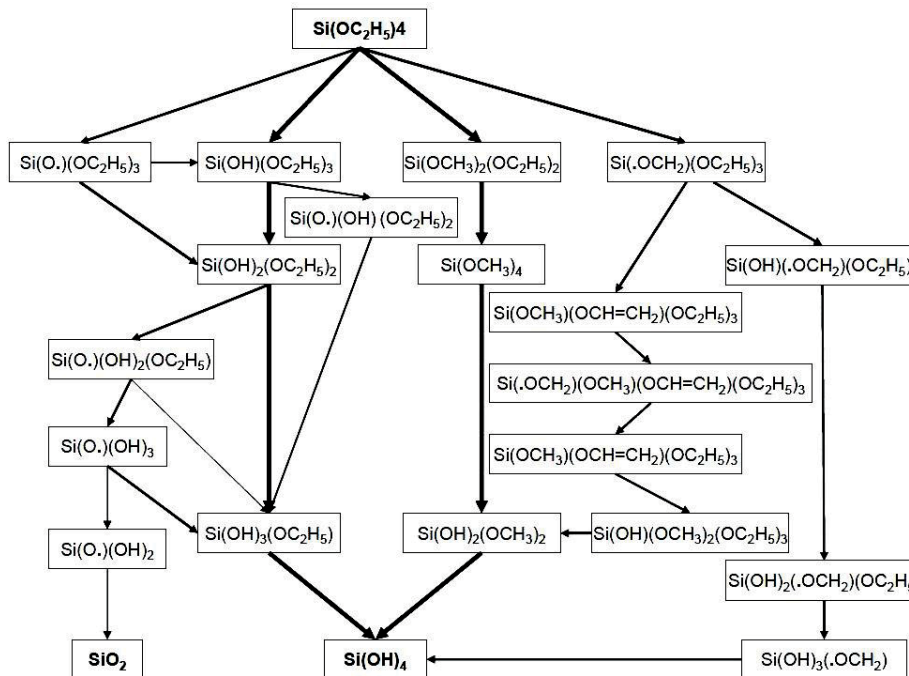


Figure 3.4: Integrated flux diagram depicting the main reaction pathways of TEOS decomposition [38]



3.2. Particle formation and growth

Gas-phase chemical reactions of the decomposition or combustion of precursors will generate a condensable species e.g. SiO_2 from TEOS combustion. Once a condensable species has been formed in the gas phase, the system is in a non-equilibrium state. It may progress toward equilibrium by the generation of new particles (homogeneous nucleation) or by condensation on existing particles (heterogeneous nucleation). If all collisions between particles are effective, the process resembles aerosol coagulation [64]. Notwithstanding that a number of different gas-phase processes exist, they all have in common the fundamental aspects of particle formation mechanisms that occurs once the product species is generated from precursor reactions [47, 65, 66].

3.2.1. Homogeneous nucleation

Homogeneous nucleation occurs once sufficiently high supersaturation is achieved as a result of formation of condensable species. The supersaturated vapor is inherently unstable and tends to form a condensed phase. The initially formed molecules and clusters will form particles through homogeneous nucleation. Clusters are generally finite aggregates of a few to several thousands of atoms or molecules. A cluster is metastable and its properties such as stability depend exactly on the number of atoms or molecules that compose it. If the clusters are thermodynamically stable, the nuclei are formed through coagulation. In the case of unstable clusters, mostly depending on temperature and concentration, the nuclei are formed through a balance between condensation and evaporation of molecules or atoms to and from the clusters until thermodynamically stable particles that are larger than a critical particle size are formed [67].

Two mechanisms of nucleation with different driving forces take place, these being physical and chemical nucleation. However, it is often not clear which mechanism is occurring and there is some debate over the distinctions between the two phenomena [66]. Physical nucleation involves only weak attractions such as van der Waals forces and is important only for species with partial pressures near their vapor pressures [68]. On the other hand, chemical nucleation involves the formation of chemical bonds with the surface and can occur at any temperature and pressure [69]. This is the mechanism by which many solid particles grow.

The precursor decomposition produces a supersaturated vapor of primary growth-species (monomers) and they generate clusters (nucleus) when a few monomers collide. The change in free energy by the formation of a spherical nucleus of radius r is given by McDonald [70]

$$\Delta G = 4\pi r^2 \sigma + \frac{4}{3}\pi r^3 \frac{1}{V_M} RT \ln S \quad (2.1)$$

where σ is the surface energy, V_M the molar volume of the monomer, R the universal gas constant, T the temperature and S the saturation ratio. The saturation ratio is defined as

$$S = \frac{p}{p_s} \quad (2.2)$$

where p is the partial pressure and p_s is the saturation pressure of the monomers. Supersaturation occurs when S is higher than 1, and brings about a change in free energy per unit volume, G_v , between the gaseous and the newly created liquid/solid phase. This change in free energy is balanced by the energy gain of creating a new volume, and the energy cost due to creation of new interface. When the overall change in free energy, ΔG , is negative, nucleation is favored (cf. Figure 3.5).

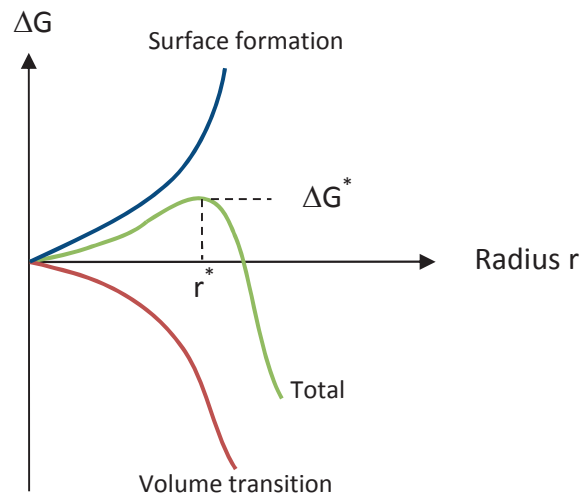


Figure 3.5: Change in free energy due to nucleation [71]

Some energy is consumed to form an interface, based on the surface energy of each phase. If a hypothetical nucleus is too small (known as an unstable nucleus), the energy that would be released by forming its volume is not enough to create its surface, and nucleation does not proceed. The critical nucleus size can be denoted by its radius, and it is when $r = r^*$ that the nucleation proceeds.

$$r^* = \frac{2\sigma V_M}{RT \ln(S)} \quad (2.3)$$

The critical free energy ΔG^* is the energy barrier for the nucleation process and given by

$$\Delta G^* = \frac{16\pi\sigma^3 V_M^2}{3(RT \ln(S))^2} \quad (2.4)$$



The random collisions in a supersaturated vapor of monomers generate nuclei of different radii. The rate of nuclei with radii greater than or equal to r^* is an important parameter in the gas-phase synthesis of nanoparticles. This rate is called nucleation rate and is given by

$$\frac{dN_n}{dt} = A \exp\left(-\frac{\Delta G^*}{k_B T}\right) \quad (2.5)$$

where N_n is the molar concentration of nuclei, A is the pre-exponential factor and k_B is the Boltzmann constant. The exponential term is the probability of the formation of a critical nucleus. The value of A is given by Friedlander [64]

$$A = \left(\frac{2\sigma}{\pi M N_A}\right)^{1/2} \left(\frac{P}{k_B T}\right)^2 \frac{V_M}{N_A} \quad (2.6)$$

where N_A is Avogadro's number and M is molar mass of the monomer. The nucleation rate has substantial influence on the primary particle size.

3.2.2. Coagulation, coalescence and agglomeration

Following nucleation of condensable material in high-temperature processes, particles are formed, which then grow further through coagulation. Particle coagulation is the process in which small particles (assumed to be spherical) collide with each other and coalesce completely to form larger spherical particles. Coagulation influences the overall particle size distribution, whereby the particle number, and the specific surface area decreases due to the formation of larger particles [6, 9]. The rate of change of the number density of particles N is

$$\frac{dN}{dt} = -\frac{1}{2} \beta * N^2 \quad (2.7)$$

where β is the collision frequency function. When the chemical reaction and nucleation times are significantly shorter than the total formation period, the particle growth will be independent of the earlier history and thus can be determined using only the frequency of Brownian collisions [47].

Depending on the temperature-residence time history and the material properties, particles formed in this way may have different morphological structures and sizes. They may hold together by weak physical van der Waals forces (soft agglomerates) or by stronger chemical or sintering bonds (hard agglomerates or aggregates) [6]. The individual particles that compose the agglomerates are called primary particles [64]. If the rate of particle collision is faster than that of their coalescence, non-spherical (agglomerate, aggregate) particles are formed (cf. Figure 3.1). If the sintering rate is faster than the particle collision rate, regularly



shaped, monolithic (dense) particles are formed. The sintering rate depends strongly on the material, primary particle size, and temperature. The materials properties that influence the particle morphology and the sinter process are, for example, the surface tension σ , and the viscosity η , or the solid state self-diffusivity D of the coalescing particles at the respective temperature [72, 73]. Furthermore, short residence times (higher flow rates) at sufficiently high temperature lead to smaller primary particles since growth takes place over a shorter time in the reaction zone. Higher reaction temperatures tend to have the same effect, by increasing the nucleation rate, and hence decreasing the amount of monomers available for each particle to grow.

The difference between soft and hard agglomerates is frequently due to the temperature at which the particles aggregate. If aggregation takes place at high temperatures during the synthesis, sintering, viscous flow and interparticle diffusion will lead to strong bonds between the primary particles [61]. If aggregation can be suppressed until the temperature has decreased sufficiently, then readily dispersed agglomerates may be formed. Other mechanisms such as vapor deposition into the necks between aggregated primary particles may also contribute to the formation of hard agglomerates. This process also takes place primarily in the high temperature region of the reactor [67].

4. Experiment

4.1. Precursor delivery systems

For highly defined reactions of metalorganic precursors and controlled synthesis of silica nanoparticles in gas-phase reactors, a precise amount of the gaseous precursor that is homogeneously mixed with the required gases must be supplied. Evaporation of the liquid precursor and premixing with the desired gases were achieved in this work utilizing three different precursor delivery systems. The selection and suitability of each method was based on the vapor pressure of the precursor at room temperature, the precursor flow rate and the experiment time.

4.1.1. Mixing vessel method

The method of preparing the initial gas mixture in a mixing vessel is based on the partial-pressure of gases, as well as on the assumption due to the low total pressure that the gases and vapors behave like ideal gases. This method has been used in this work to prepare the initial gas mixture for the shock-tube experiments as well as supplying the flame reactor with diluted precursor. The setup of the mixing vessel that has been used for the flame reactor is illustrated in Figure 4.1. It consists of a 50 liter stainless-steel tank, which is ultra high vacuum (UHV) sealed, and a combination of a rotary pump and an oil diffusion pump. Oil diffusion pumps are known as fluid entrainment pumps and work without mechanical movement. They produce extremely high vacuums (10^{-6} mbar) by diffusing the gas into the vapor of heavy oil. The gas is carried off and separated from the oil vapor by condensation [74, 75]. This setup was specifically used for the experiments with the flame reactor. In the shock tube experiments a turbo molecular pump was used instead of an oil diffusion pump. The liquid precursor is prepared in a little UHV-tank made from stainless-steel and evacuated from other gases. Membrane valves are used to separate the precursor tank and the argon cylinder, or any other required gases, from the mixing vessel.

The mixing vessel is initially evacuated, using a combined pump system, down to a pressure of 10^{-6} mbar. Subsequently, vapor from the precursor tank is sent into the mixing vessel by opening the valve (V1) until the desired pressure, typically 2 mbar, is reached. The precursor vapor in the mixing vessel is then diluted with argon to a mixture pressure of 1000 mbar. To ensure a homogeneous mixture the gases are left to diffuse for about two hours. This technique provides the highest accuracy in the precursor delivery methods used.

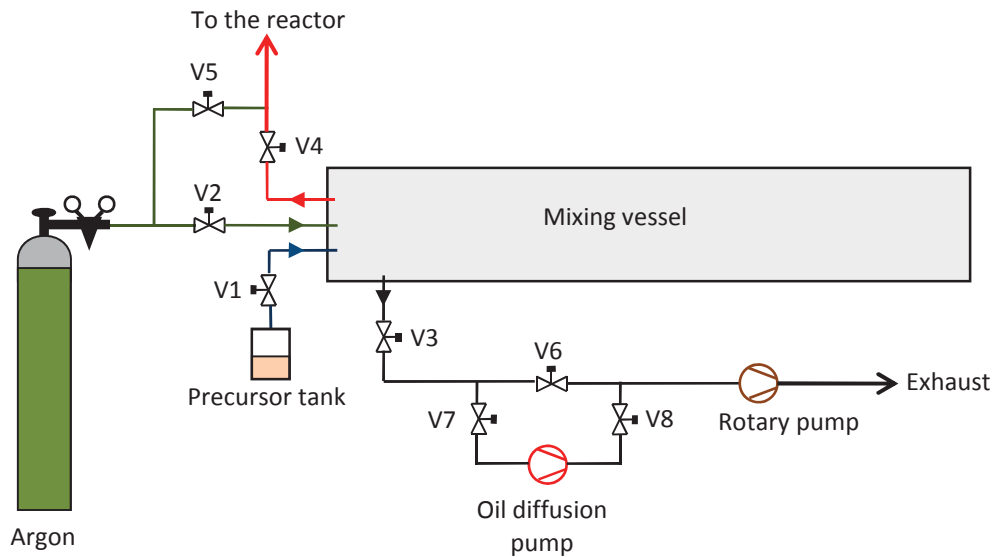


Figure 4.1: Schematic of the precursor mixing vessel setup

4.1.2. Pressure-controlled mixing (bubbler system)

The pressure controlled or bubbler-based system consists of a precursor tank, two mass flow controllers and a pressure control system. Figure 4.2a shows a simplified illustration of the bubbler system setup that has been used in this work for the supply of gaseous TEOS into the microwave-plasma reactor. The mass-flow controller MFC 1 was used to control the mass flow of nitrogen as a carrier gas through the precursor tank. A certain amount of precursor vapor is extracted by bubbling nitrogen through the liquid precursor. The pressure inside the tank was controlled with means of a combined setup of pressure transducer and a feedback control valve from Bronkhorst. The second mass flow controller MFC 2 was used to dilute the precursor to avoid condensation prior to the reactor.

The concentration of the precursor vapor in the precursor tank is estimated from the vapor pressure of the precursor at the measured temperature of the liquid inside the tank. The flow of vapor is controlled by the carrier gas and by keeping the pressure constant inside the bubbler. Variation in the concentration of precursor vapor can also be achieved by altering the pressure inside the precursor tank. This precursor delivery system can supply the gas phase reactor with diluted precursor for long experimental times. However, the exact concentration of the precursor cannot be well known.

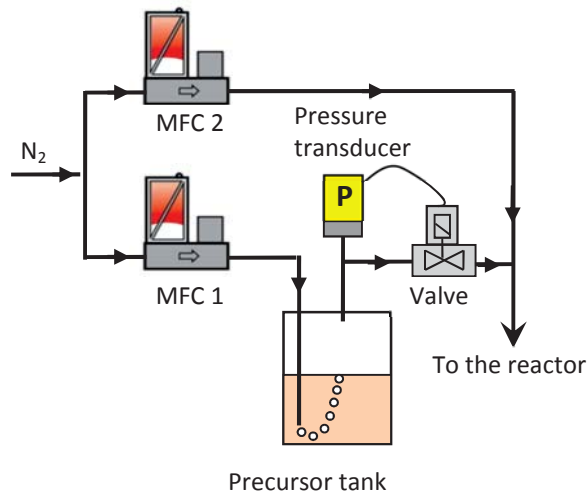


Figure 4.2: Simplified illustration of the bubbler system setup

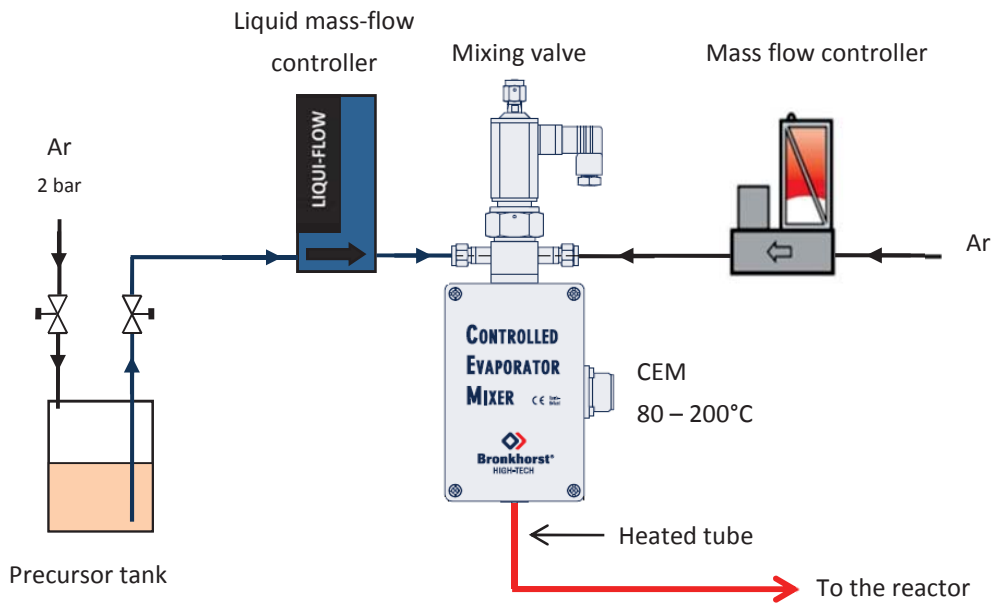


Figure 4.3: Liquid-precursor delivery system

4.1.3. Controlled evaporation and mixing (CEM)

The liquid-precursor delivery system consists of a precursor tank and a controlled evaporator-mixer system from Bronkhorst, which includes a liquid mass-flow controller, a gas mass-flow controller (MFC) and the mixing valve on top of the vaporization chamber (see Figure 4.3). A noble gas such as argon with a pressure of 2 bar presses on the surface of the liquid



precursor inside the tank causing the precursor to flow into the liquid mass-flow controller. The CEM-system is based on an injection technique in which the liquid is measured and controlled by a mass-flow controller. The advantages of the CEM liquid injection system include fast response times, high repeatability, good stability and low working temperature [76]. The liquid, controlled by the liquid flow controller, is transported with a carrier gas into the evaporator-mixer where vaporizing takes place. The CEM can provide vapor temperatures between ambient and 200°C. The inner volume of the mixing chamber was minimized, so that the response of the system would be defined mainly by the response of the liquid and gas MFCs. The partial pressure of the fluid downstream of the evaporator mixer must be lower than its vapor pressure at the set temperature to prevent condensation.

4.2. Gas-phase reactors

4.2.1. Hybrid microwave-plasma hot-wall reactor

4.2.1.1. Overview of hot-wall reactors

Hot-wall reactors or oven sources are simple systems (cf. Figure 4.4) that can be used to produce nanoparticles. The hot-wall reactor can be operated under a wide range of operating parameters such as temperature, pressure and concentration. They are heated to a certain temperature to achieve supersaturation from the decomposition of a gaseous precursor. The gas composition is freely selectable, which enables the synthesis of oxide as well as non-oxide nanoparticles. The pressure is often atmospheric but it can also be reduced down to a few mbar. The maximum operation temperature is limited due to the choice of crucible material. Despite the simple construction of this reactor, simulating the reaction kinetics and subsequent particle formation and growth should be three-dimensional due to the radial temperature gradient in addition to the axial temperature profile. The axial and radial temperature gradients can be varied in addition to the pressure by using different carrier gases which have different energy transport properties, heat conductivities and heat capacities.

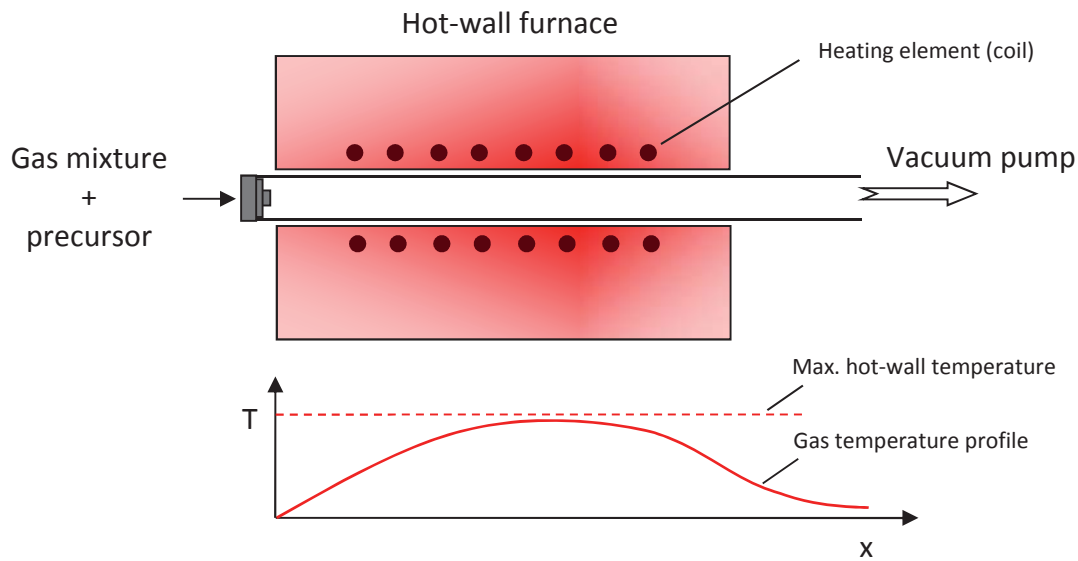


Figure 4.4: Simplified sketch of a hot-wall reactor

4.2.1.2. Overview of microwave-induced plasma reactors

An alternative means of providing the energy needed to induce precursor reactions that lead to supersaturation and particle nucleation is to inject the precursors into a microwave-induced plasma. The plasma enhances the kinetics of the chemical reactions leading to nanoparticle formation due to ionization and dissociation of the reactive molecules [42, 56, 77, 78]. Microwave plasmas are very interesting for the gas-phase synthesis of nanoparticles, especially at laboratory scales. Microwave-plasma reactors provide high heating rates (10^6 K/s) and they are generally compact and easy to control. However, their high energy requirement makes microwave-plasma reactors less interesting for industrial applications unless the value of a very specific product justifies the cost of operation.

In principle, a microwave-plasma reactor consists of a magnetron, a circulator and the microwave antenna (cf., Figure 4.5). The magnetron cavity is a high-powered vacuum tube that generates microwave radiation. The microwave radiation usually is guided from the magnetron to the microwave-antenna through a wave guide made from a good electrical conductor, e.g. aluminum. The circulator, which is made of magnets and ferrite material, is used to control the direction of signal flow in the microwave circuit. Thus, the circulator protects the power supply against any reflected power by guiding reflected microwaves into an absorbing water bath. The microwave-antenna is made from aluminum and has the function of focusing and matching the incident microwave radiation into the center where the plasma locat-

ed. The idea of employing a tuner is to optimize the energy transfer into the plasma and minimize reflection. Further details can be found in [79].

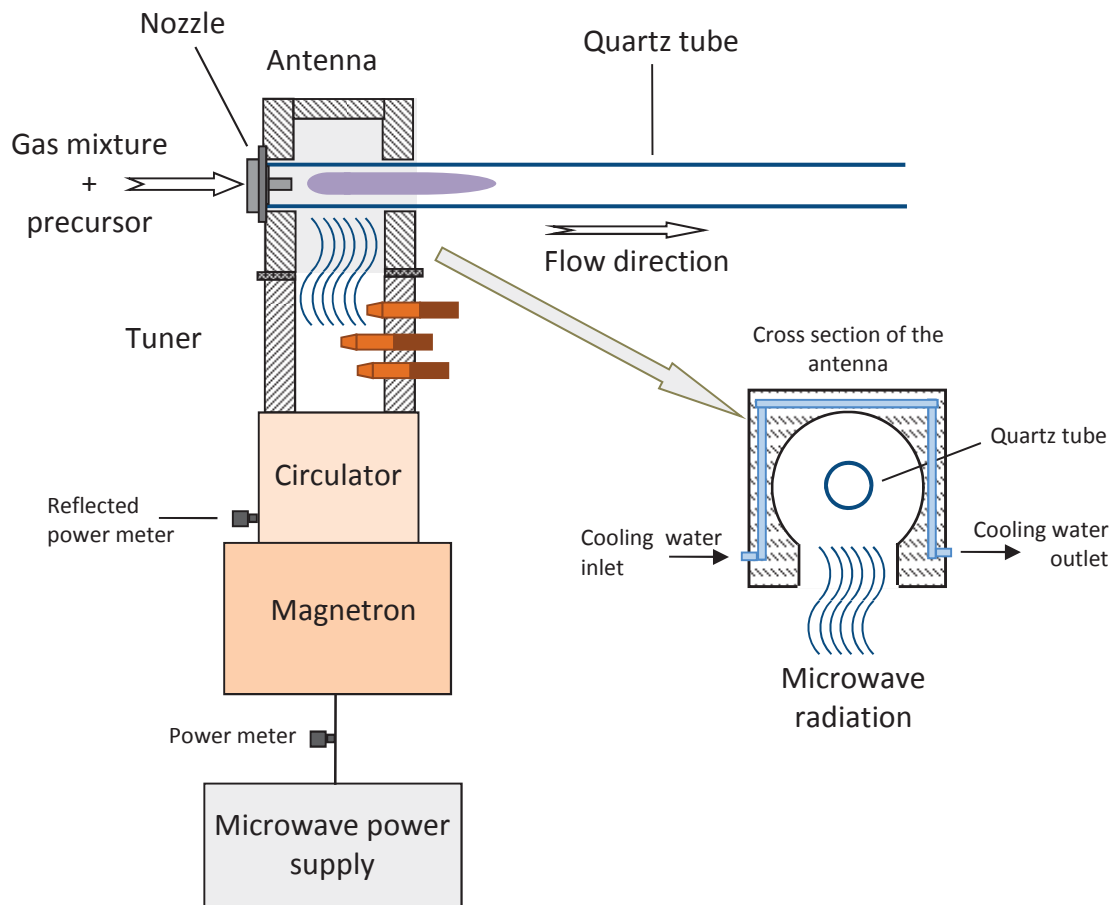


Figure 4.5: Schematic illustration of the μ W-plasma reactor

Theoretical background of plasma processing

Plasma in physics and chemistry is a state of matter similar to gases in which a certain fraction of gaseous atoms and molecules are ionized leading to strong electrostatic forces between gas molecules [15, 80]. Therefore, plasma is often called the fourth state of matter. The plasma can be generated through heating with high enough energy which leads to the ionization of atoms and molecules. Other methods involve electrical systems for induction of a plasma using direct-current (DC), radio frequency (RF) or microwaves. The plasma consists of positively and negatively charged elements (electrons and ions) in such a way that the sum of all electric charges is zero. These electrically charged elements are intermixed with neutral gas atoms or molecules. The degree of ionization (usually between $10^{10} - 10^{13} \text{ cm}^{-3}$), which is the ratio of charged particles over the uncharged ones, may be quite small. Due to the mobile electric charges, a plasma is electrically conductive [78].

The thermal equilibrium of a plasma is an important feature for the classification of plasmas which are distinguished based on the relative temperatures of electrons, ions and neutrals. In thermal plasmas, free electrons and heavy neutrals possess the same temperature, i.e. they are in thermal equilibrium with each other. In contrast, non-thermal plasmas (non-equilibrium) have different levels of thermal energy. In such plasmas the electrons have the highest thermal energy whilst the ions have significantly less energy, and the neutral gas species possesses the lowest energy (see Table 4.1). Moreover, molecules with different degrees of freedom (such as translation, rotation and vibration) are also not in equilibrium.

Table 4.1: Subdivision of plasmas [81], where T_e , T_i and T are the temperatures of electrons, ions and neutral gas species, respectively.

Low-temperature plasma (LTP)		High-temperature plasma (HTP)
Thermal LTP $T_e \approx T_i \approx T \leq 2 \times 10^4 \text{ K}$ e.g., arc Plasma at normal pressure	Non-thermal LTP $T \approx T_i \ll T_e \leq 10^5 \text{ K}$ e.g., microwave plasma	$T_e \approx T_i \geq 10^7 \text{ K}$ e.g., fusion plasma

In the case of the microwave-induced plasma, the energy is transmitted to the plasma via the microwave radiation field, which accelerates the electrons until they have sufficient energy to cause further ionization in a chain reaction [60]. The electrons can then dissipate their energy through a vast number of collisions with neutral and ionic species causing excitation and ionization processes. Because this is a relatively inefficient process due to the large difference in mass, the heavy species' temperature will remain lower than the electron temperature [82]. It must be noted that the atoms and ions are much heavier than electrons and energy transfer in a two-body collision is much more efficient if the masses are similar.

A characteristic feature of microwave radiation is that its wavelength is comparable to the dimensions of the apparatus (2.45 GHz, $\lambda = 12.2 \text{ cm}$). The absorption of microwave radiation in gas, i.e. the energy that is delivered to a unit volume per time, depends on the electron-neutral collision frequency and the ionization energy, i.e. on the gas pressure and the nature of the gas. The absorption efficiency in a 2.45 GHz discharge is high for He at pressures in the region of 10^3 and 10^4 Pa whereas the maximum efficiency for Ar is reached at 200 Pa [83]. Microwave discharges can also be operated at pressures as high as atmospheric [81]. However, at atmospheric pressure the collision frequency is so high that an increase in microwave power input is required to ensure sufficient ionization of the gas [84]. The electron acceleration and collision energy exchange mechanism in high-frequency fields have been discussed in detail by Brown [85].

4.2.1.3. Microwave-plasma hot-wall reactor

The hybrid reactor, which consists of a microwave plasma reactor and a subsequent hot-wall furnace, has been constructed for gas-phase synthesis of high-purity silica nanoparticles using TEOS as the precursor (see Figure 4.6). The aim of combining the microwave-plasma reactor and the hot-wall furnace is to extend the residence time of the reactions at high temperature. This combination allows the particle formation to be studied by characterizing the final product with variable temperature-time histories.

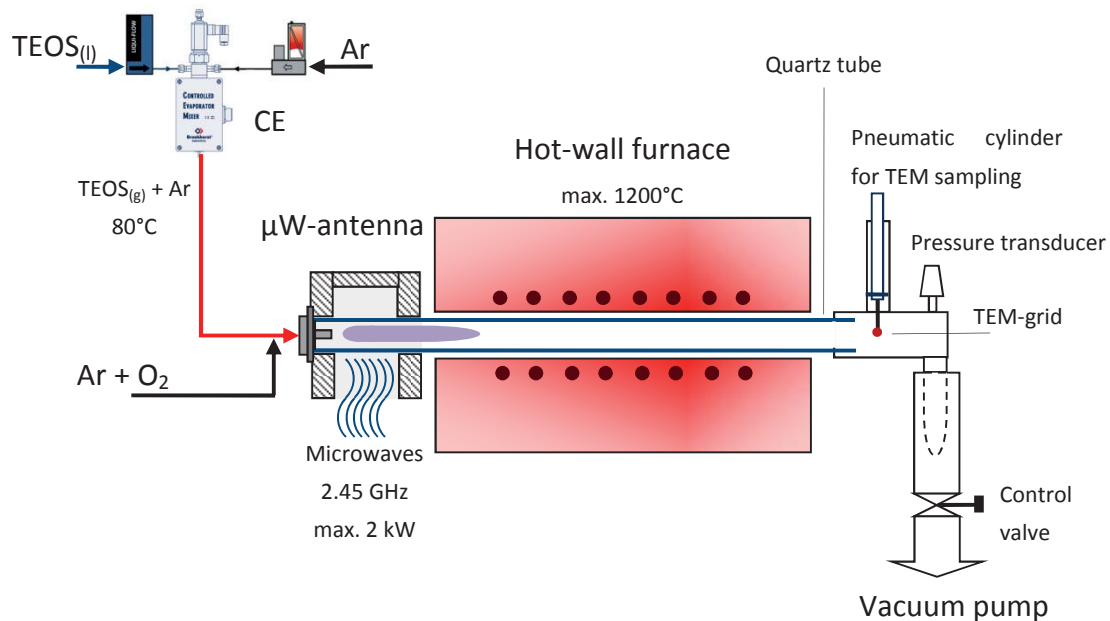


Figure 4.6: Hybrid microwave-plasma hot-wall reactor

A 2.45 GHz magnetron oscillator (Fricke und Mullah) capable of delivering up to 2 kW of continuous power was used as a microwave power source. The magnetron was protected from the reflected power by using a circulator and a matched load. The microwave radiation enters the antenna through a directional coupler so that the incident and reflected power could be monitored simultaneously. The power absorbed by the plasma was defined as the incident power minus the reflected power, assuming no power is lost to the housing. The hot-wall furnace (Carbolite, three zone tube), which is 450 mm long, can be electrically heated up to 1200°C.

In order to obtain reproducible synthesis conditions, the current apparatus allows the gas flow rates, gas composition, pressure, and temperature of the hot-wall furnace to be controlled. The reactor pressure can be varied between 20 and 1000 mbar using a control valve



behind the particle filter. A rotary vacuum pump with a capacity of 100 l/min can ensure a wide variety of stable gas flow rates and pressures in the reactor.

The required gaseous TEOS (mixed with argon as the carrier gas) was supplied using a controlled evaporator mixer (CEM) from Bronkhorst (cf. Figure 4.3). The CEM system supplies gas mixtures that can feed up to 13 g/h of TEOS vapor into the reactor despite the poor vapor pressure of TEOS (1.6 mbar at 20°C). The tube that connects the CEM and the reactor inlet is heated up to 80°C to prevent condensation of TEOS. An additional gas mixture of argon and oxygen, as oxidizing reagent, is added to the TEOS/argon mixture prior to entering the reactor.

The synthesized particles are filtered from the flowing gas using a cellulose extraction thimble downstream of the reactor. The collected particles were used for ex-situ analyses such as transmission electron microscopy (TEM) and isothermal Brunauer-Emmett-Teller (BET) nitrogen adsorption method. Online-sampling of silica particles was achieved from the reactor chamber by thermophoretic deposition onto TEM-grids using a double acting pneumatic cylinder. The sampling time can be defined in a time range between 50 and 500 ms.

4.2.2. Premixed low-pressure H₂/O₂/Ar flame reactor

4.2.2.1. Overview of flame reactors

Rather than supplying energy externally to induce the reaction and particle nucleation, particle synthesis can be achieved within a flame and its hot exhaust gas. The energy needed for initiating the precursor reactions would be supplied in-situ by the combustion reactions (cf. Figure 4.7). This is by far the most economic approach in nanoparticle synthesis, used to produce millions of metric tons per year of carbon black and metal oxides [2, 4, 86]. In addition, flame reactors can be easily scaled up for practical applications and consequently used for continuous processing [20]. Flame reactors have also been extensively used in laboratory scale systems to produce metal oxide nanoparticles such as magnetic oxide, high-temperature superconductors and photocatalysts. However, coupling the particle production to the flame chemistry is a complex process that is rather difficult to control. It is primarily useful for making oxides, because the flame environment is quite oxidizing. Recent advances are expanding flame synthesis to a wider variety of materials and providing greater control over particle morphology.

Powders, liquids and vapor can be used as precursors in a flame reactor. The flame provides the energy to evaporate the precursor and to drive the chemical reactions. The precursor concentration can be high due to the high energy density in the flame. The heating rate in the flame is quite high and temperatures from 1000 to 2400°C can be realized [15]. Several

parameters that influence the flame are used to control the particle growth such as temperature profile, reactor residence time and reactant concentration. However, these parameters cannot be changed in flame reactors independently. Every adjustment of the feed flow causes a change in the other parameters.

Using “premixed” or “non-premixed” flames can influence the shape of the flame. In a premixed flame the fuel and the oxidizer are already mixed and the reactions take place right after the burner head. These premixed flames are typically very short. In non-premixed flames the fuel and the air or oxygen are fed separately to the burner head. The reactants must mix through diffusion and turbulent mixing and react in the mixing zone [80].

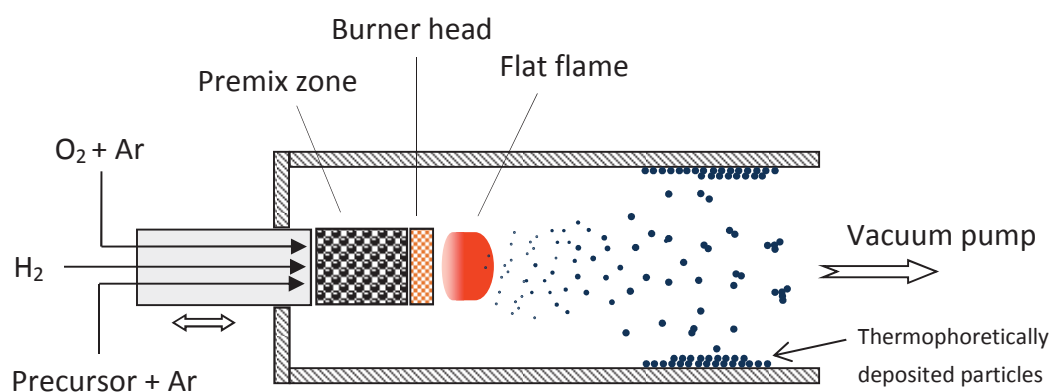


Figure 4.7: Schematics of the low-pressure $H_2/O_2/Ar$ flame reactor

4.2.2.2. Experimental setup of the premixed low-pressure $H_2/O_2/Ar$ flame reactor

The experimental setup in Figure 4.8 shows a simplified illustration of the premixed low-pressure $H_2/O_2/Ar$ flat flame reactor. The complete setup is divided into three chambers, which are operated under different pressures. The precursor, TEOS or HMDSO diluted in Ar, was prepared in a vessel and mixed with the flame gases prior to entering the 30 mbar chamber through a porous sintered-bronze burner head. The premixed flame was ignited and stabilized on the water-cooled burner head which was mounted on a horizontal translation stage that allowed the distance between the burner head and the probing nozzle (flow coordinate) to be varied. The major characteristics of this flame type is that the maximum temperature is reached just above the burner head. Furthermore, hydrogen as a fuel allows for synthesis of particles with low level contamination due to the absence of carbon [87]. The low-pressure operation (30 mbar) creates a spatially expanded reaction and particle-growth zone where important information about species concentration can be measured with high resolution. The flame was doped with diluted precursor, leading to a gas-phase reaction that yields condensable metal oxides. Because of the axial temperature gradient in

the reactor, condensation of metal oxides as well as growth of particulate solids by coagulation and coalescence occurs, leading to a mixture of primary particles, agglomerates and aggregates.

A sampling orifice that is located downstream of the first chamber is used to extract and expand the silica nanoparticles into the second chamber operated at 10^{-3} mbar. The rapid expansion into molecular free jet “freezes” almost all chemical reactions and particle interaction. A skimmer located in this chamber then extracts the particles from the centerline of the expanded jet into the third chamber that is operated at 10^{-6} mbar, generating a particle-laden molecular beam. In the third chamber a particle mass spectrometer (PMS) which works on the principle of deflection of charged particles passing through an electric field is in place.

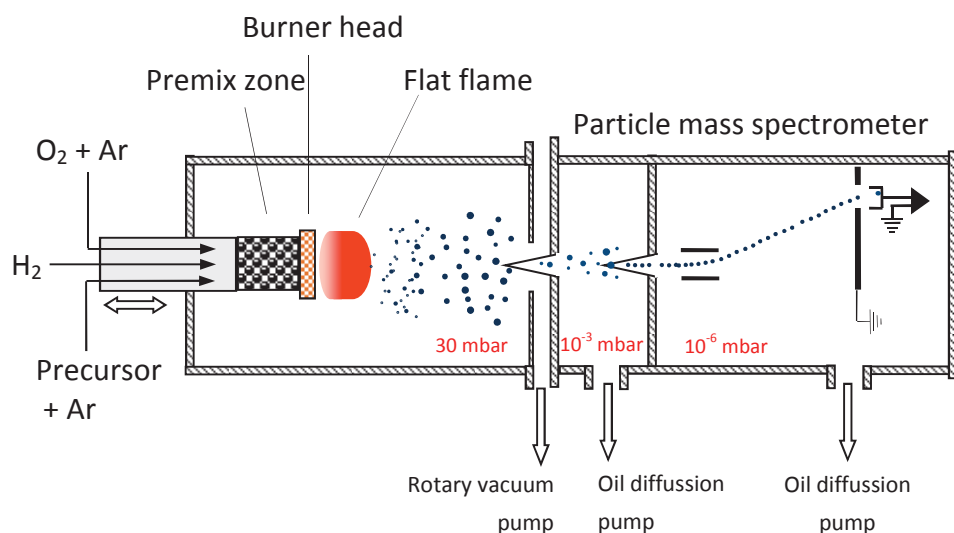


Figure 4.8: Premixed low-pressure $H_2/O_2/Ar$ flame reactor

4.2.2.3. Particle mass spectrometer (PMS)

The particle mass spectrometer is used to analyze the mean particle size as well as the particle size distribution. These are considered to be two major characteristics of nanomaterials that influence their unique properties. The combination of the PMS with the gas phase reactor, in this work only the flame reactor, allows online determination of the mass of charged particles. The measured mass of charged particles can be then converted into the particle-size distribution using the solid density of the material. The technique of the PMS measurement is based on combined physical principles, which are:

- the physics of the molecular beam technique to generate a particle beam
- an electrical deflection and filter system which classifies the particles due to their kinetic energy and velocity in the beam

- a detection system for the charged particles

The transfer of the particles from a normal aerosol into a beam of particles is necessary to realize the measurement principle of the PMS. This is possible by applying the molecular beam technique, which is well known from classical gas dynamics [88]. The generation of a molecular beam is achieved by expanding the gas through a small orifice nozzle using a pressure difference between the reactor chamber (30 mbar) and the expansion zone (10^{-3} mbar) of the PMS (cf. Figure 4.9). The gas species and nanoparticles are adiabatically expanded to form a supersonic jet whereby the particles move at approximately equal velocities with very few collisions. The flow conditions are such that the gas temperature decreases very rapidly, nearly completely freezing any physical or chemical processes inside the expansion aerosol probe. The center of the free jet is extracted using a sharp edged nozzle called “skimmer” and moves as a particle-laden or molecular beam into a second vacuum chamber [89].

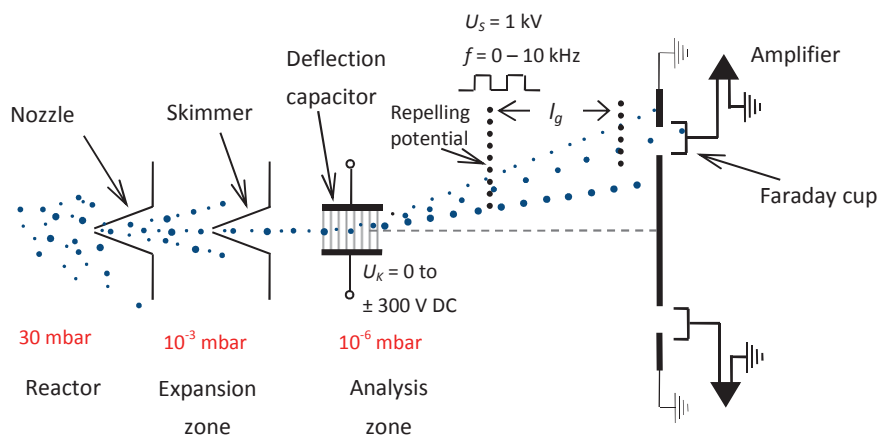


Figure 4.9: Simplified schematic illustration of particle mass spectrometer (PMS) [89]

The analysis zone of the PMS consists of a deflection capacitor with length l_K , width b_K , an aperture at a distance L_{PMS} from the deflection capacitor (Figure 4.10a), and a Faraday cup behind an aperture for particle-charge detection. The well-focused particle beam, which moves in the x-direction (cf. Figure 4.10), enters the center of the deflection capacitor. By applying a certain voltage between the parallel plates of the capacitor the charged particles are deflected from the original path. The force of the electrical field is assumed to exist only inside the capacitor and to be perpendicular to the electrode surfaces. The field strength therefore is $E = U_K / b_K$. An individual charged particle entering the electrical field is deflected by a force $F = ze U_K / b_K$ acting in the direction of the field lines. It causes the particle to ac-

celerate in the y -direction in relation to its mass: $\ddot{y}_p = ze U_K / b_K m_p$. The individual particle trajectory and the velocity components inside the capacitor

$$0 \leq x_p \leq l_K \quad \text{or} \quad 0 \leq t \leq \frac{l_K}{v_p}$$

can be described in Cartesian coordinates using the time t as a parameter thus,

$$y_p = \frac{1}{2} \frac{zeU_K}{m_p b_K} t^2 \quad x_p = v_p t \quad (3.10)$$

$$\dot{y}_p = \frac{zeU_K}{m_p b_K} t \quad \dot{x}_p = v_p \quad (3.11)$$

Outside the electrical field the particles move along straight lines as indicated in Figure 4.10a. The direction of motion with respect to the x -axis results from the condition of constant velocity components \dot{y}_p and \dot{x}_p outside the capacitor. The particle trajectory is therefore given by:

$$y_p = \frac{zeU_K l_K}{m_p v_p^2 b_K} \left(x_p - \frac{l_K}{2} \right) \quad \text{for } x_p \geq l_K \quad (3.12)$$

The well-focused particle beam passing through the capacitor splits into different trajectories according to the mass and charge of individual particles. According to equation 2 each particle mass m_p with charge ze has its individual trajectory $y_p = f(x_p)$.

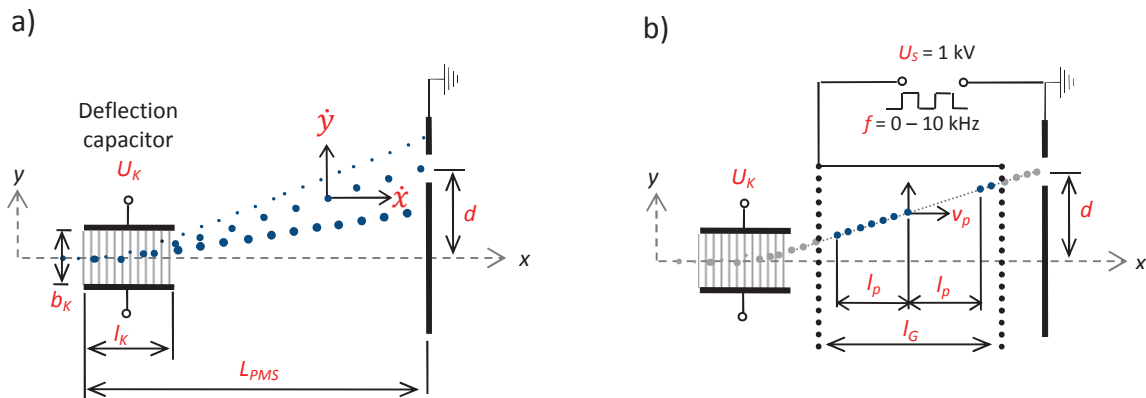


Figure 4.10: a) Deflection of charged particles in an electrical field and resulting particle trajectories in a vacuum containment. b) PM velocity measurement

In the next stage, a grounded slit, with width Δd at a position $y = d$ from the x -axis, is introduced at a distance $x = 50$ mm from the origin of the coordinate system. It separates a discrete class of particles which can pass through the slit whereas the rest are blocked and collected by the grounded plate. By re-arranging equation 2 and setting $y_p = d$ and $x_p = l$, the kinetic energy at this selected point of the signal is:

$$\frac{m_p v_p^2}{ze} = U_K \frac{l_K}{b_K} \left(\frac{2l}{d} - \frac{l_K}{d} \right) \quad (3.13)$$

For fixed geometrical conditions, especially for a fixed slit position or beam deflection d , capacitor dimensions l_K and b_K , and for a known distance L_{PMS} between the entrance of the capacitor and the aperture, the voltage U_K selects particles of kinetic energy $(m_p v_p^2/2)$ carrying elementary charges z . By varying or tuning the deflection voltage U_K , particles of various energies can pass through the aperture. In other words, U_K is a direct and unique measure of the kinetic energy of particles which pass through the slit arrangement. Thus,

$$U_K = \text{const} \frac{m_p v_p^2}{ze} \quad (3.14)$$

Up to this point, the particle beam is classified by the deflection voltage U_K (together with the slit) into discrete classes of kinetic energy. The desired proportionality between particle mass (m_p/ze) and deflection voltage (U_K) can be obtained from equation 3.14, if the particle velocity v_p is known. This property can be measured by an electrical chopping system, as illustrated in Figure 4.10b. The beam of charged particles passes through two grids supplied with a synchronously-pulsed repelling potential. The upper grid forms packages of charged particles when the potential is zero and the particles can thus pass through the grid and are repelled during the time that the voltage is suddenly increased to 1 kV. The length of the package l_p depends on the frequency of the grid voltage f and on the particle velocity v_p . Whether the full package of particles or only part of it can pass through the second grid and reach the aperture can be estimated by the application of a simple geometrical phase condition. Only very few or no particles pass through the second grid if the package length l_p is the reverse odd-numbered multiple of the grid distance l_G . This results in a series of minima of the electrical current I or the particle flux I_p , which occur in the later described current plots at frequencies $f_{min,i}$, for the following conditions:

$$v_p = 2f_{min,i} l_{pi} \quad (3.15)$$

$$l_{pi} = l_G, \frac{l_G}{3}, \frac{l_G}{5}, \text{etc.} \quad (3.16)$$

Equation 3.15 represents the measurement guidance for the particle velocity v_p . The frequencies $f_{min,i}$ of the repelling potential which cause the minimum particle flux I_p must be determined. At this minimum frequency, the particle velocity v_p can be measured for every group of particles selected by the deflection voltage U_K . Therefore, equation 3.14 can be further simplified to its final form:

$$U_K = \text{const} \frac{m_p}{ze} \quad (3.17)$$

This is a well known relation in mass spectroscopy. The deflection voltage U_K of the capacitor is a direct measure of the particle mass m_p divided by the particle charge ze . What remains is to determine the particle flux that is classified by both the deflection voltage U_K and the ap-

erture. The simplest way is to collect the charged particles using a Faraday cup and to convert the signal into an equivalent electrical current I by means of a very sensitive electrometric amplifier. The measured electrical current is, for singly charged particles ($z = 1$), directly proportional to the particle flux passing the aperture; thus

$$I = f(U_K) \sim \Delta \dot{N}_p \quad (3.18)$$

For particles carrying more than one elementary charge ($z > 1$) the situation is in principle similar. However, practically only a small portion of doubly charged particles can exist in some conditions due to small particle sizes.

4.2.3. Gas-dynamically-induced particle synthesis

“Gas-dynamically-induced particle synthesis” (GIP) is a new concept for mass production of highly specific oxide nanoparticles from gas-phase precursors in a shock-wave flow reactor. The reactor consists of two consecutive Laval nozzles with a reaction zone in between and utilizes gasdynamic heating and cooling rates respectively (see Figure 4.11). In this concept the shock wave of an over-expanded supersonic nozzle flow heats the gas mixture, including the gaseous precursor, instantaneously up to high temperatures and initiates the reactions. Single particles with a narrow size distribution are aimed to be produced with the aid of high heating and cooling rates in this processing technique. Figure 4.11 shows an overview of the principle of GIP operation. The exhaust gas from the pore burner (1) flows at a high speed, high temperature (1300 K) and high pressure (10 bar) through the supersonic tunnel. Gaseous TEOS with nitrogen as carrier gas is then injected (2) prior to the first nozzle. TEOS is mixed with the exhaust gas, which is then accelerated in the first nozzle (3) to supersonic flow speeds and produces a shock wave (4) at a certain axial location downstream. The shock wave heats the gas mixture instantaneously and initiates the chemical reaction of precursor decomposition or ignition, which is then followed by particle formation and growth (5). The length of the reaction volume is variable. Therefore, the residence time within the reaction volume is adjustable. Sudden expansion to lower pressure (atmospheric pressure) through the second nozzle (6) reduces the temperature instantaneously. Finally, the total enthalpy of the flow is reduced by injecting cooling water in a quenching system (7). A detailed process description is given by Grzona et al. [90] and Al-Hasan [91].

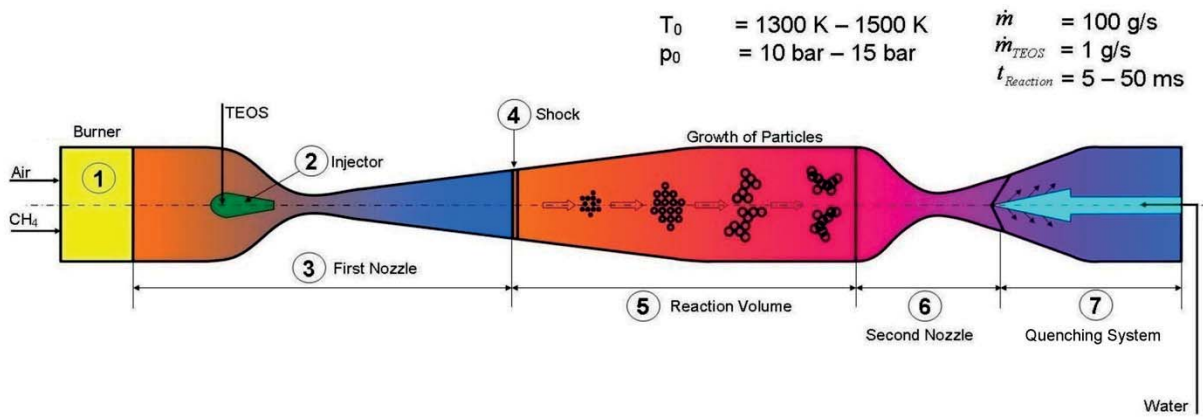


Figure 4.11: Schematic representation of the gas-dynamically-induced particle synthesis [90]

The realization of this novel process required several studies such as:

- Numerical simulation of the gas dynamic, precursor chemistry and particle growth and subsequently comparison with experiments
- Precursor injection and mixing with the gases prior to the shock wave
- Precursor chemistry and particle formation and growth in the gas phase
- Gasdynamic cooling and water evaporation in the quenching system
- Sampling method of the particles from different locations in the reaction volume

The studies mentioned above have been carried out by different groups.

4.2.3.1. 3D-Simulation of the production of gas-phase synthesized nanoparticles in the reactor

This part of the work has been carried out by Al-Hasan [19, 91, 92] and Giglmaier [18] at the Institute of Aerodynamics and Fluid Mechanics, Technical University of Munich. The 3-D simulation models the entire gasdynamic flow and the particle formation and growth including injection and mixing of the precursor, ignition delay, heat release, formation of monomers and coagulation. The governing equations for the flow are the 3-D time-dependent Favre-averaged Navier-Stokes equations for compressible mixtures of gases. For the simulation of particle growth an efficient bimodal monodisperse model has been investigated based on the work of Kruis et al. [93]. In contrast to the original model, an additional balance equation for the monomer concentration is taken into account in order to reproduce the bimodal particle distribution, which is due to the comparatively slow precursor combustion.

The particle sizes predicted by the 3-D CFD simulation are validated against experimentally obtained results for the generator facility. In particular, the sensitivity of the processes is analyzed with respect to operation condition variations, such as stagnation conditions, precursor mass flow and wall cooling. Detailed insight can be provided into the complexity of this novel process of gas-phase synthesized, non-aggregated nanoparticle generation, and

display the potential of coupled 3-D Navier-Stokes/particle-growth simulations as a tool for the design and analysis of innovative particle production processes and particle reactors.

The pilot facility was designed using 3-D reactive CFD simulations that provided a detailed insight into the full process. Figure 4.12 shows a numerical simulation of the doubly choked Laval nozzle system. The shock position is determined by the critical cross sections A_1^* and A_2^* and the overall losses due to heat release from the precursor combustion, wall cooling and friction. As the ignition of the precursor is initiated by the temperature rise across a gasdynamic shock, 3-D simulations of all thermodynamic conditions of the transonic flow are required to predict the conditions are at a stagnation temperature and pressure of $T_{01} = 1400$ K and of $p_{01} = 10$ bar respectively. At the first minimum cross section, $A_1^* = 88.8$ mm² where $x = 0$, the flow reaches sonic speed, i.e. Mach number $M = 1$, and accelerates further downstream to supersonic flow speed. The static temperature (red curve) drops to a minimum of 880 K at $x = 196$ mm. At that position a pseudo shock system with a pre-shock Mach number $M = 1.8$ forms and decelerates the flow.

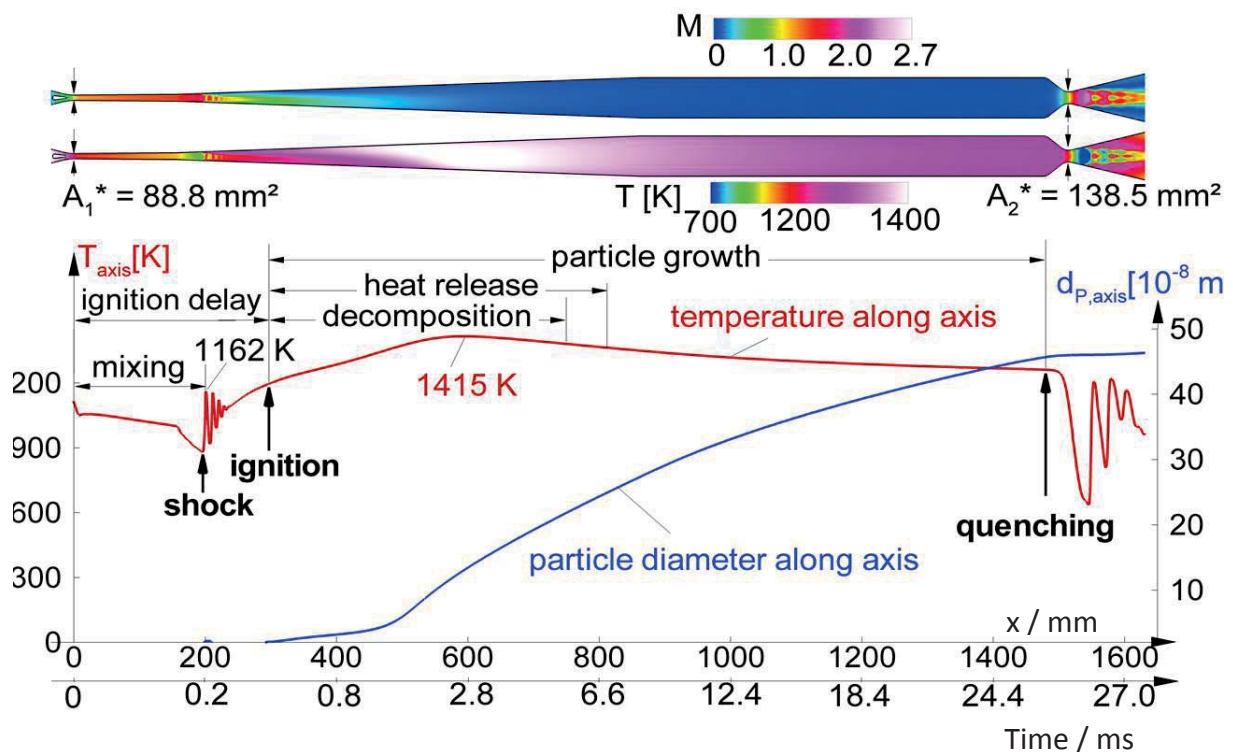


Figure 4.12: Dominating phenomena during "gas-dynamically induced particle synthesis" [18]

The precursor TEOS is injected into the flow shortly upstream of the first throat (cf. Figure 4.11). The available mixing-length from the injector to the pseudo-shock system is 200 mm in order to ensure mixing of the precursor and the carrier gas. The rise in static temperature

across the gasdynamic shock leads to ignition of the precursor. The location of ignition on the time axis in Figure 4.12 is determined from the ignition delay time study as a function of temperature, which has been carried out in this thesis work (cf. section 5.1). Simulation of the particle formation and growth begins after the ignition delay time of TEOS.

4.2.3.2. Experimental study of the mixing process of the injected precursor with the reactor gases

This part of the work has been carried out by Mohri [94, 95] (Institute of Combustion and Gasdynamics, University of Duisburg-Essen) and Wohler [96] (Institut für Thermodynamik der Luft- und Raumfahrt, University of Stuttgart). Homogeneous molecular mixing of the precursor with the reactor gases between the injector and the reactor main flow is essential to achieve high particle quality of low agglomeration index and narrow particle size distribution. The injector design and the flow conditions play the most important role on influencing the mixing process. Studying the mixture formation and flow conditions between the injected flow and the reactor main flow, using different injector designs have been conducted with the laser based diagnostic technique known as laser-induced fluorescence (LIF) imaging.

4.2.3.3. Studying the precursor chemistry and the particle growth

The kinetics data as well as the ignition delay times of the precursor are essential to define the injector axial location and the GIP reactor length. The residence time between the injector and the shock wave should be shorter than the ignition delay time at the respective gas temperature. This is to ensure that precursor ignition occurs after the shock wave. When the temperature at the injector is high enough to initiate the reactions, the precursor will not ignite before the shock wave if the ignition delay time is longer than the residence time between the injector and the shock wave. Moreover, the reactor should be long enough to cover the required time for the precursor decomposition, particle formation and growth. The fine tuning of the residence time can be adjusted with the reactor conditions. This study has been carried out for the GIP project as part of this doctoral work. The kinetics of the precursor decomposition and ignition were studied in shock-tube experiments. The particle growth was investigated in gas-phase reactors such as a flame and a microwave plasma reactor under various conditions. These experiments provide the required information for the design of the GIP reactor as well as the numerical simulations. The GIP reactor length as a variable parameter and the experimental conditions can be defined with means of a previous numerical simulation of the particle growth process.

4.2.3.4. Supersonic expansion and water quenching system

This part of the work has been carried out by Rakeł [97] at Institut für Technische Thermodynamik und Kältetechnik, Karlsruhe Institute of Technology KIT. The high cooling rate beyond the second Laval nozzle is achieved by the combination of instantaneous expansion in the lower pressure (atmospheric pressure) to reduce the temperature and a supersonic water quenching system to reduce the total enthalpy by evaporation and freezes the reactions. Figure 4.13 illustrates the principle of the supersonic quenching system, whereby the scale proportions are adapted to improve the description. The gas is flowing as indicated from left to the right through the convergent nozzle. The temperature descent is illustrated as a color gradient. As water penetration into a supersonic gas stream is relatively low, the water is injected from the wall and in the center of the Laval nozzle to cover the entire cross-section. The so called quench lance extends from the outlet into the direction of the nozzle throat in the center. The quench lance is a pipe with a slender cone at its tip to avoid strong oblique shocks.

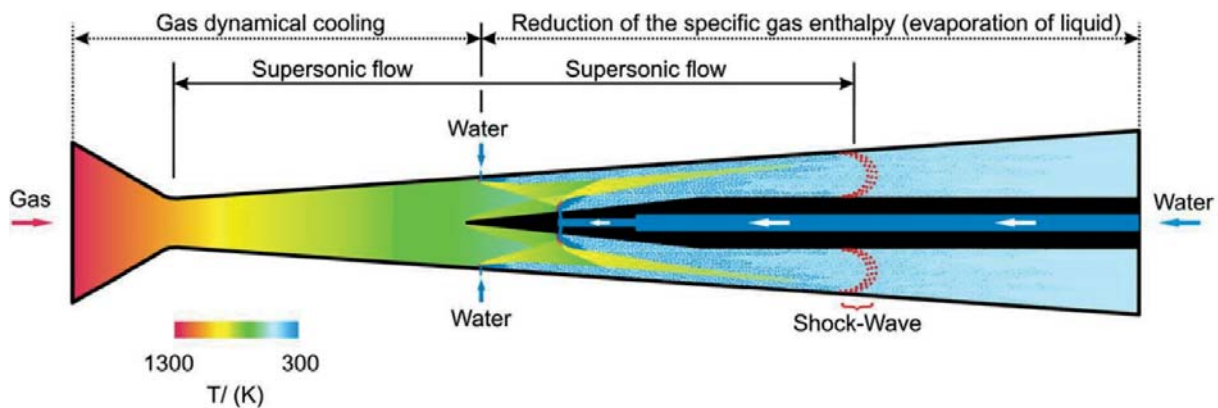


Figure 4.13: Schematic sketch of the supersonic quenching system [97]

4.2.3.5. Sampling technique of particles from the reactor

This part of the project has been carried out by Verena Goertz [98] at Institut für Mechanische Verfahrenstechnik und Mechanik, Karlsruhe Institute of Technology (KIT). An important aspect of the novel reactor is the characterization of the particles during their growth. In order to investigate particle size, size distribution and morphology, samples are taken at different positions in the reactor, i.e. in the reaction volume and downstream of the quenching. In order to ensure representative sampling, the probe has to be adjusted with respect to the high particle number concentration and the high temperature and pressure inside the reaction chamber. Chemical reaction must be prevented inside the probe.

Figure 4.14 represents the schematics of the probe. The probe for extracting particles from the reaction chamber consists of four coaxial thin walled stainless steel capillaries. Due to the multi coaxial design it is not possible to provide a 90° bend probe which would allow sampling in flow direction. Therefore, the probe is installed normal to the flow direction in the reactor part. To avoid particle sampling out of the recirculation area, the probe was bevelled at an angle of 30°. By applying 3-D unsteady scale adaptive simulations (SAS) [99] the design was optimized with the commercial CFD-Tool Ansys CFX. As the gases in the reaction chamber reach high temperature e.g. 1300 K, it is necessary to cool the probe by means of water inside the two outer capillaries. The product is exhausted through the central capillary. Finally, the particles are collected on a carbon-coated TEM grid attached to a glass fiber filter.

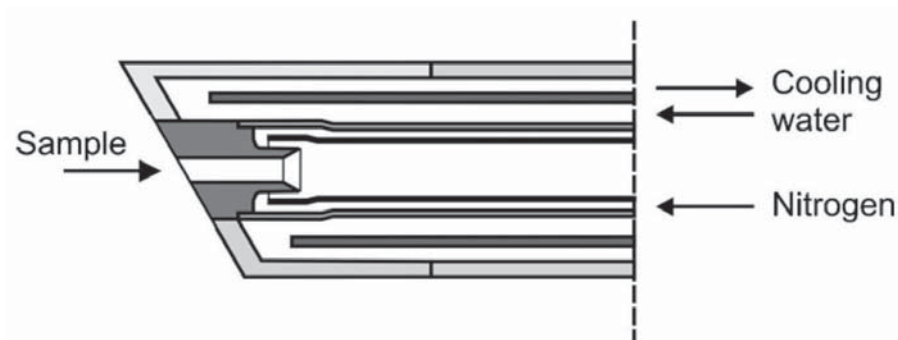


Figure 4.14: Schematic representation of the sample probe to extract particles from the reaction chamber [98]

4.3. Shock-tube experiments

4.3.1. Principles of shock-tube experiments

The shock tube is a laboratory device used mainly for aerodynamic and high temperature kinetics studies [100]. Because of the high and variable stagnation enthalpies (and temperatures) that are obtained, the shock tube provides a means to study phenomena such as thermodynamic properties of gases at high temperatures, dissociation, ionization and chemical kinetics [101]. It allows the study of gas-phase kinetics under a wide range of temperatures and pressures that are difficult to obtain in other types of testing facilities. A shock tube has the ability to heat up a gas in a very short time, such that any reactions at intermediate temperatures and the influence of transport are prevented.

In general, shock tubes are thick-walled tubes made of stainless steel with circular, square or rectangular cross sections with a very smooth inner surface [102]. Some form of a diaphragm, usually made from aluminum, separates a gas at low pressure and a gas at high-pressure. The low-pressure gas, referred to as the *driven gas*, is subjected to the shock wave.

The high pressure gas is known as the *driver gas*. The corresponding sections of the tube are likewise called the driven and driver sections respectively. The driver gas is usually chosen to have a low molecular weight and high speed of sound, but may be slightly diluted to 'tailor' interface conditions across the shock. Hydrogen or helium may be used, with helium being the safer option. The driven section contains the test gas mixture including the fuel or the precursor. Typically the driver section is fed with driver gas until the diaphragm bursts and the highly compressed driver gas flows into the low pressure chamber. A shock wave then propagates through the test gas, while a rarefaction wave travels through the driver gas (cf. Figure 4.15). The interface, across which a limited degree of mixing occurs, which separates driven and driver gases is referred to as the contact surface and follows the shock wave at a lower velocity.

The pressure distribution prior to bursting of the diaphragm and the resulting pressure and temperature distributions after bursting of the diaphragm are shown in Figure 4.15 along the axis of the tube. It shows the axial pressure and temperature distributions, at (a) $t = 0$, for intermediate times (b) and (c) before the arrival of the incident shock wave to the end wall, and (d) and (e) after the reflected shock wave reaches the sample gas. In Figure 4.15 it can be observed that the incident and reflected shock waves induce two stepwise increases of temperature and pressure in the test gas.

Successive longitudinal time-pressure distributions, indicating the shock front position, can be plotted in an $x-t$ diagram, i.e. the typical distance-time diagram, as shown in Figure 4.16 [103]. At time $t = 0$ the diaphragm ruptures and a series of compression waves coalesce into a normal shock wave which propagates at supersonic velocity in the driven section. The moving shock wave induces the fluid behind it to travel in the same direction with velocity v_{iw} . A contact surface formed at the interface between the driven and driver gases, behind the incident wave, moves at velocity v_{cs} . The difference between v_{iw} and v_{cs} permits the test gas to achieve the condition of high pressure and temperature (T_5, p_5), required for the experiment, when the reflected wave is formed and before the arrival of the contact surface. This is shown as region 5 in Figure 4.16 where the test gas is under uniform conditions. Simultaneously, in the driver section a set of rarefaction waves propagate in the opposite direction inside the driver gas. The arrival of the rarefaction waves disturbs the test gas. The time interval between the arrival of the reflected wave and of the contact surface is the available time for measurements, Δt_{ms} (e.g. 2 ms).

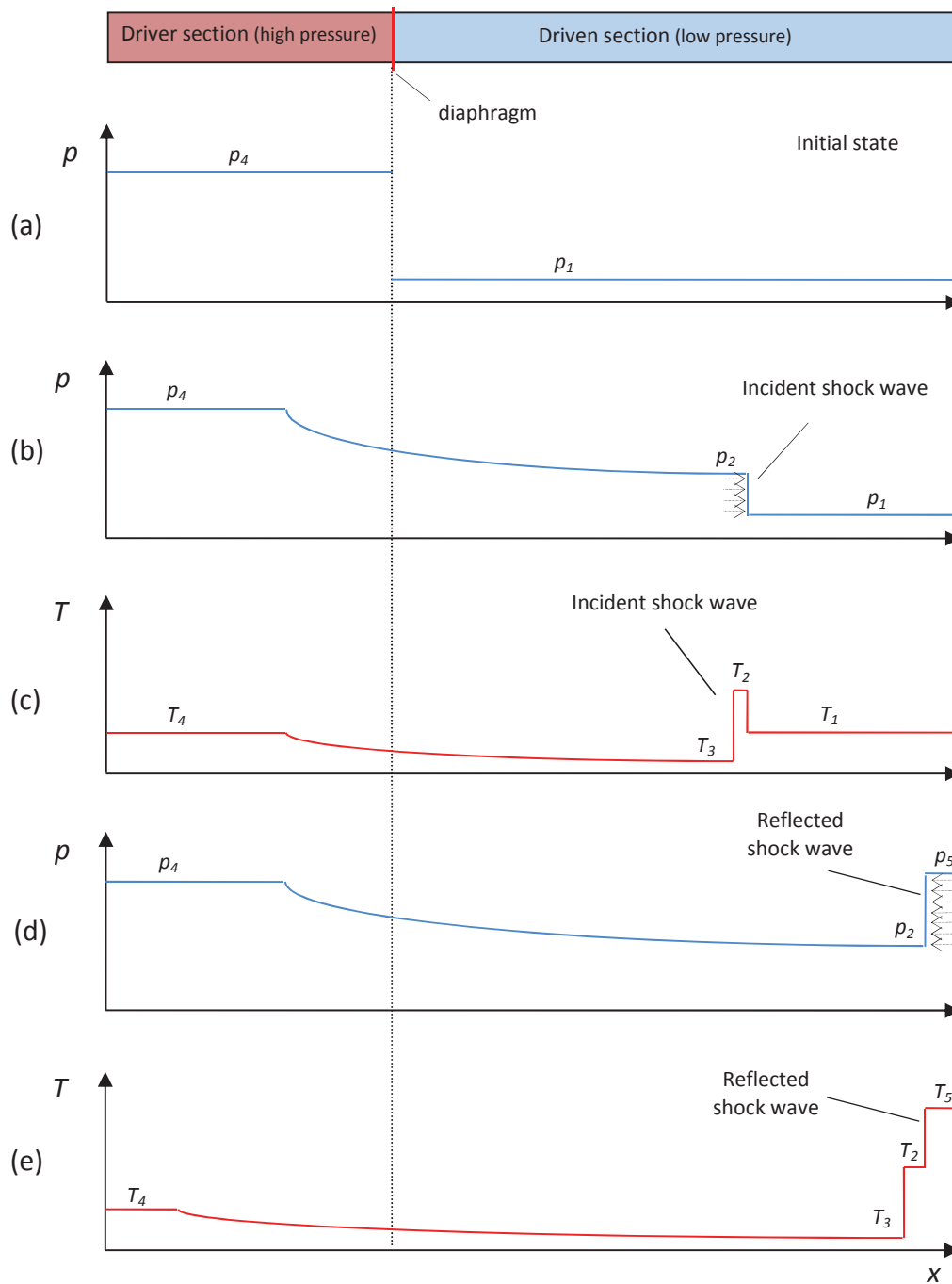


Figure 4.15: Operation principle of a shock tube

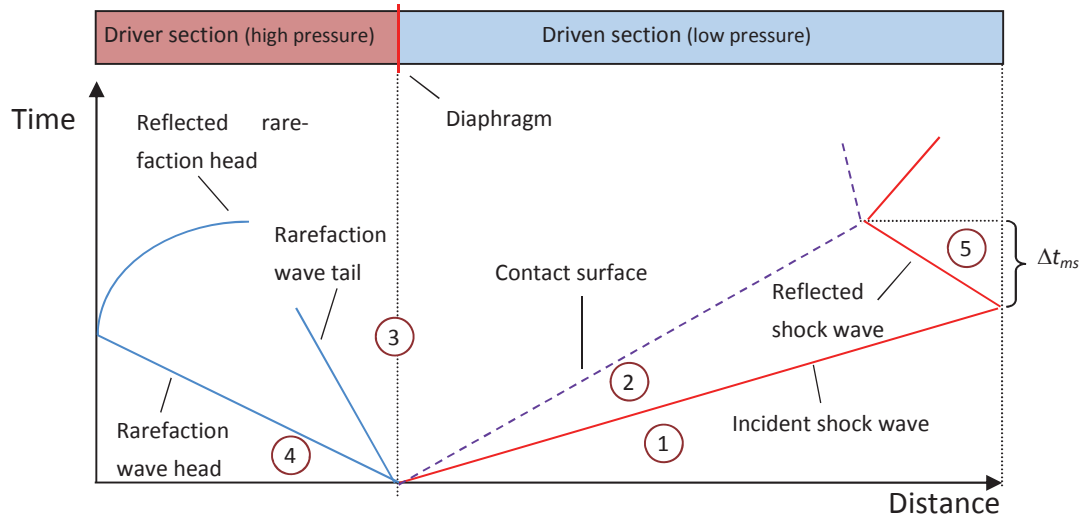


Figure 4.16: Distance-time diagram in shock tube. The gas behind the reflected shock wave is at rest. Adapted from Zel'dovich et al. [103]

4.3.2. Shock-tube experiments to determine the ignition delay time of TEOS and HMDSO

Ignition delay times provide kinetics data of the precursor ignition in an oxidizing environment. Emission from the electronically excited $\text{OH } A^2\Sigma^+$ state (OH^*) near 307 nm is a prominent feature of hydrogen and hydrocarbon flame spectra [104]. OH^* emission and the reactions important in OH^* chemiluminescence have long been studied [104,108]. The OH^* -formation reactions and rates are presented in Table 4.2. The CH and H species in the reactant side of the reaction equation no. 1 and 2 in Table 4.2 are fragments during TEOS decomposition. This means that these reactions take place during TEOS decomposition and ligand combustion. Increasing the temperature will accelerate the decomposition of TEOS and therefore the formation of OH^* , and OH^* emission will appear earlier.

Table 4.2: Elementary reactions of OH^* formation and quenching. Rate coefficients are expressed as $k = AT^n \exp(-E/RT)$ with units of cal, mol, cm and s

No.	Reaction	A	n	E		Source
1	$\text{CH} + \text{O}_2 \leftrightarrow \text{OH}^* + \text{CO}$	3.24×10^{14}	-0.4	4 150	Formation	[109]
2	$\text{H} + \text{O} + \text{M} \leftrightarrow \text{OH}^* + \text{M}$	3.10×10^{14}	0.0	10 000	Formation	[109]
3	$\text{OH}^* + \text{H}_2\text{O} \leftrightarrow \text{OH} + \text{H}_2\text{O}$	5.92×10^{12}	0.5	-861	Quenching	[110]
4	$\text{OH}^* + \text{CO}_2 \leftrightarrow \text{OH} + \text{CO}_2$	2.75×10^{12}	0.5	-968	Quenching	[110]

The ignition delay time with respect of the shock-tube experiments of a combustible fuel-oxygen-argon mixture is defined by the time delay between the compression of the gas and

the sudden increase in the rate of reaction, coinciding with large temperature and pressure changes and emission of light. This time interval is a characteristic quantity for any fuel and is a function of the initial temperature, pressure and mixture composition [101]. The ignition can be observed by measuring the onset of OH*-chemiluminescence emission at 307 nm. The wavelength of emitted light is selected using a band-pass filter and detected with a photomultiplier located downstream in the measurement plane (cf. Figure 4.17). One of the main objectives of measuring the ignition delay time is to define the axial location of the precursor injector in the GIP reactor (cf. Figure 4.11). When the exhaust gas temperature at the precursor injector is high enough to initiate the reactions, precursor ignition upstream of the shock wave can be avoided. On the other hand, when the reactions do not commence at the injector the shock wave will heat the gas mixture instantaneously and thus the reactions will begin. In this case the ignition delay time must be included into the overall residence time beyond the shock wave.

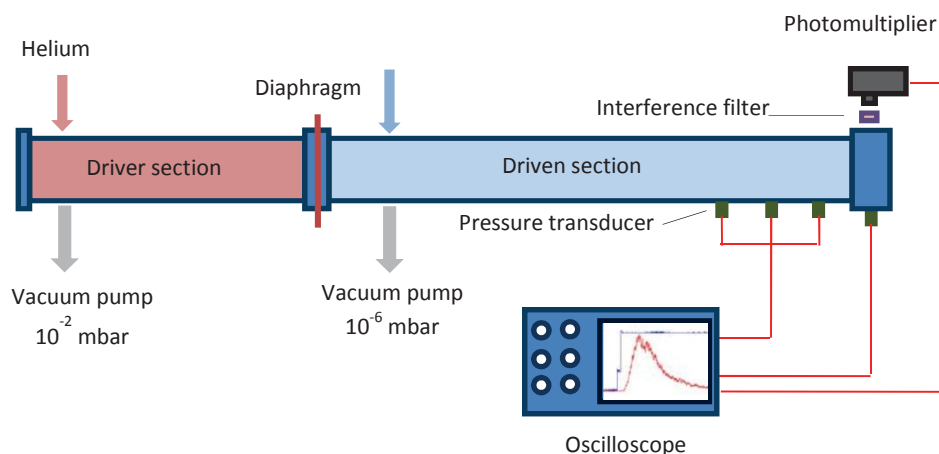


Figure 4.17: Simplified schematic of a shock tube with an experimental setup for the ignition delay time measurements

Two shock tubes that have the same diameter of 80 mm have been used. Shock tube 1 has been used for low precursor concentrations and chemiluminescence detection while shock tube 2 has been used for higher concentrations. Test times in both experiments were up to 2 ms. The driver and driven sections of shock tube 1 have a length of 3.8 and 7.2 m, respectively. A 300 μm thick aluminum diaphragm was chosen to achieve a pressure of about 10 bar behind the reflected shock wave. The driven section can be baked out and pumped down to pressures below 10^{-6} mbar using a turbo molecular pump. The driver section can be pumped to 10^{-2} mbar with a rotary pump. Gas mixtures were prepared in a stainless-steel mixing vessel. Ignition was observed by measuring the onset of OH* chemiluminescence



emission at 307 nm through a window on the side wall of the shock tube 20 mm upstream of the end flange. An arrangement of two slits in between the window and the detector results in a narrow acceptance angle of the detector corresponding to a time resolution of 6 μs defining by the passage of the reflected shock wave and the slit diameter.

Shock tube 2 is equipped with pumps that can handle particle-laden gases and thus allows experiments at higher precursor concentrations. Aluminum diaphragms of 70 and 100 μm thickness were chosen to achieve pressures of 1.7 and 2.8 bar behind the reflected shock wave, respectively. The driven and the driver sections as well as the mixing vessel can be pumped down to 4×10^{-2} mbar using a dry vacuum pump (Edwards dry star; Model QDP 80).

Temperatures and pressures behind the reflected shock wave (T_5 , p_5) are determined from the incident shock-wave velocity assuming one-dimensional behavior using the standard approach [111]. The velocity is measured from the arrival time of the incident shock wave at four pressure transducers located at 20, 170, 320 and 570 mm upstream of the end flange. The liquids and gases used were of highest commercial purity: TEOS > 98%, HMDSO >99%, He, O₂, N₂, CO₂ and Ar > 99.999%.

Ignition delay times of TEOS were measured in shock tube 1. Homogeneous mixtures were provided by injecting liquid TEOS into the evacuated stainless-steel mixing vessel with subsequent addition of the desired amount of gases. The mixture rested for 2 hours prior to the experiments to ensure homogeneous mixing. In the first set of tests, 1600 ppm TEOS was mixed with dry synthetic air. In a second set of tests TEOS was mixed with a gas mixture that is representative of the exhaust gases from the methane flame in the GIP reactor. This contained N₂, O₂, CO₂, and H₂O. For these experiments the desired amount of water was injected directly into the driven section of the shock tube, and after evaporation mixed with the TEOS/gas mixture from the mixing vessel. The mixture rested for one hour to ensure homogeneous mixing. In the first and second set of tests the ignition delay times of TEOS in dry and humid gas mixtures were investigated as a function of temperature (in the range 1140–1390 K). Additionally, a set of tests was conducted in order to investigate the influence of water concentration on the ignition-delay time of TEOS. For this purpose various amounts of water, 0–12 mol%, were added to a fixed mixture of TEOS (1600 ppm) in dry synthetic air.

Homogenous mixtures of HMDSO in dry and moist synthetic air were prepared in a similar manner as described for TEOS. The concentration of HMDSO in the gas mixtures was 1800 ppm. HMDSO was investigated in shock tube 2 due to a higher amount of particle production. Since HMDSO produces higher number of particles than TEOS, HMDSO was investigated in shock tube 2.

4.3.3. Time-of-flight mass spectrometer (TOF-MS)

4.3.3.1. Theory of time-of-flight mass spectrometry

Time-of-flight mass spectrometry is an early arrival in the mass spectrometry family which underwent a deep revival in the last 20 years [112]. The implementation of new-generation ion sources allowing the analysis of high-mass molecular species and the solution of virtually all the technical problems affecting the early instruments allowed TOF-MS to successfully compete with magnetic and quadrupole instruments for some applications despite their higher sensitivity and resolving power. The ability of time-resolved measurements and high-repetition-rate of TOF-MS within a very short time provides the opportunity to analyze chemical kinetics in the gas phase. Particularly, in the combustion context, TOF-MS has been combined with a shock tube for qualitative and quantitative measurements of chemical kinetics behind the reflected shock wave to determine the reaction mechanisms, the reaction rates and the time-resolved gas composition. The challenge for using TOF-MS in combination with shock-tube experiments is the short time window available as test time in the shock tube. Due to its wide mass range, TOF-MS may in principle be used to measure particles up to 10^6 u [113] (4 nm in case of SiO_2).

Time-of-flight measurement is a method in mass spectrometry where mass separation is obtained after creating ions, all of which have approximately the same kinetic energy through acceleration in an electric field, and allowing them to travel in a field-free region. Since the ion velocity is acquired according to the mass-to-charge ratio m/z , the ions separate into individual packets and the masses can thus be detected sequentially in time [114].

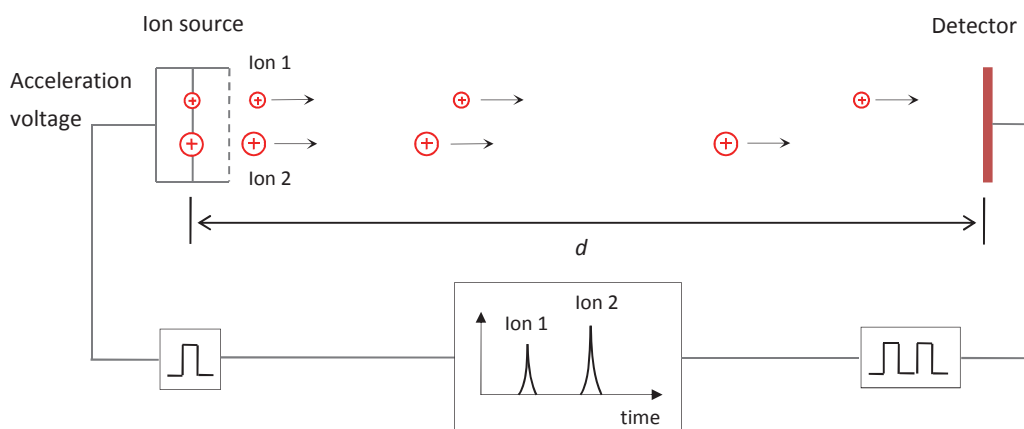


Figure 4.18: Principle of a linear time-of-flight mass spectrometer (TOF-MS)

To explain the theory behind TOF-MS a simplified principle set-up of a linear TOF is presented in Figure 4.18. The ions are generated in the instrument's ion source (*ionization*, typically achieved by electron impact or laser beams) with the same initial kinetic energy and acceler-

ated by means of a pulsed electric field (*extraction*). As they then pass along the field-free drift zone, they are separated by their masses as the lighter ions travel faster. This enables the instrument to record all ions sequentially in time as they arrive at the detector and so covers a very large mass range. The relationship between time or velocity and mass is governed by the energy balance. Independent of the ionization method the potential energy of a charged particle in an electric field is related to the charge of the particle and to the strength of the electric field as given in the following equation:

$$E_p = qU = ezU \quad (3.1)$$

Where E_p is potential energy, U is the electric potential difference (Voltage), q is the charge of the particle ($q = ez$), e is the charge of the electron and z is the number of electron charges. When the charged particle is accelerated by the voltage U , it gains kinetic energy. The kinetic energy of any mass is:

$$E_k = \frac{1}{2}mv^2 \quad (3.2)$$

In effect, the potential energy of the ion in the electric field is converted to kinetic energy, meaning that equations 2.1 and 2.2 are equal:

$$E_p = E_k \quad (3.3)$$

$$ezU = \frac{1}{2}mv^2 \quad (3.4)$$

The velocity of the charged particle after acceleration will not change since it moves in a field-free high-vacuum flight tube. The velocity of the particle can be determined in a time-of-flight tube since the timing of the ionization and the length of the flight path (d) of the ion is known and the flight time of the ion (t) can be measured using a transient digitizer or time to digital converter. Thus,

$$v = \frac{d}{t} \quad (3.5)$$

and the value of v from eq. 3.5 can be substituted into eq. 3.4 to give

$$ezU = \frac{1}{2}m\left(\frac{d}{t}\right)^2 \quad (3.6)$$

By rearranging eq. 3.6 the flight time will be expressed as

$$t = \frac{d}{\sqrt{2eU}} \sqrt{\frac{m}{z}} \quad (3.7)$$

Where $\frac{d}{\sqrt{2eU}}$ contains factors that are related to the instrument settings and can be taken as a constant k , which in principle does not change when a set of ions are analyzed in a single extraction pulse. The final time-of-flight equation can be expressed as:

$$t = k \sqrt{\frac{m}{z}} \quad (3.8)$$

This equation reveals more clearly that the time-of-flight of the ion varies with the square root of its mass-to-charge ratio (m/z).

Therefore, theoretically all the ions are given the same initial kinetic energy by the extraction pulse and then drift along the field-free zone where they will be separated so that all ions of the same m/z arrive at the detector at the same time. In practice, the initial kinetic energy distribution of the ions in the ion source lowers the mass resolution by creating a time-of-flight distribution for each m/z [115]. This is corrected for by the application of an ion mirror (reflectron TOF-MS) at the end of the drift zone [116]. This consists of a static electric field which repulses the ions back along the flight tube, usually at a slightly displaced angle (cf. Figure 4.19), resulting in a refocusing of ions with the same m/z value at one location when the ion detector is in place. The flat surface of the ion detector (typically microchannel plate, MCP) is placed at the point where ions with different energies, reflected by the reflectron, hit the surface of the detector simultaneously. The time-of-flight is defined as the time difference between the on-set of the extraction pulse in the ion source and the time the reflected ions are detected. A point where ions of the same mass and charge but different energies arrive at is often referred to as time-of-flight focus of the reflectron. An additional advantage to the reflectron TOF-MS arrangement is that roughly twice the flight path is achieved in a given length of instrument providing a higher mass resolution.

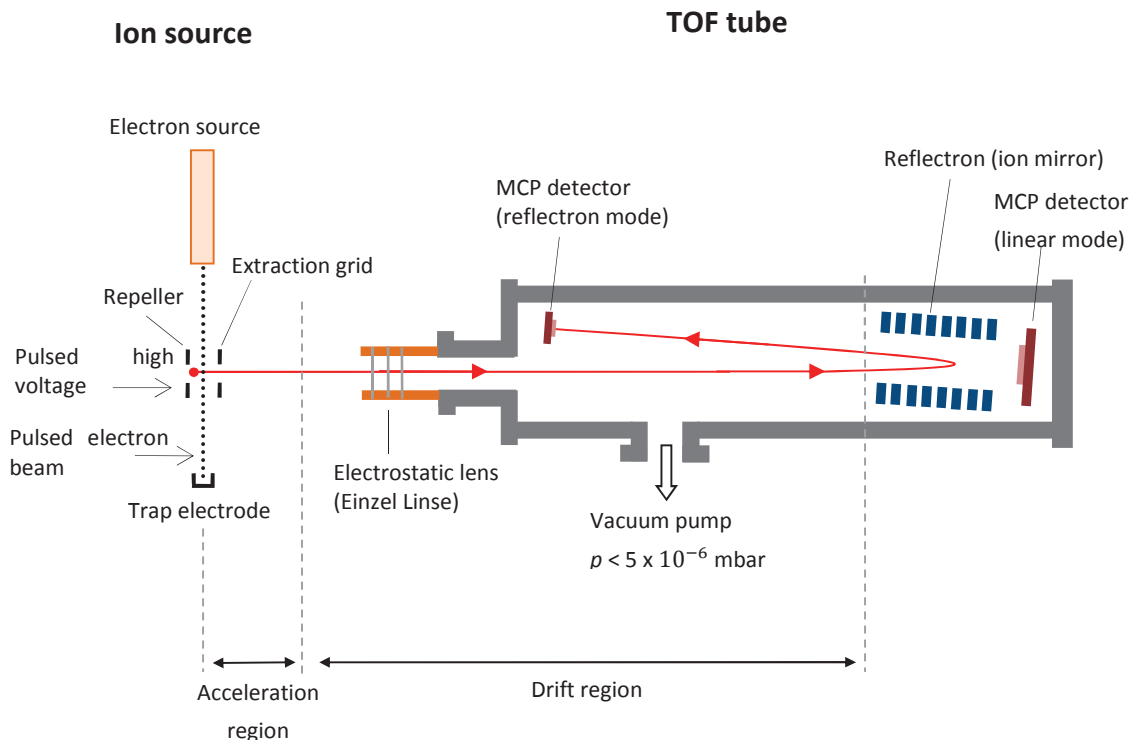


Figure 4.19 Simplified schematic of a time-of-flight mass spectrometer

4.3.3.2. TOF-MS for kinetics investigations at the shock tube

The high temperature and pressure conditions behind the reflected shock wave in the shock tube are stable up to a few milliseconds. Therefore, fast detection methods that provide time-resolved information about the change of composition of the investigated mixture are required. A high-repetition-rate (HRR) time-of-flight mass spectrometer (TOF-MS) from Kaesdorf can simultaneously measure the transient concentration profiles for numerous species with approximately one measurement every 10 μs [108, 117]. Combinations of shock tubes with TOF-MS are established for the study of complex reaction systems. The most extensive set of TOF-MS shock-tube measurements was published by Kern et al. [118-120].

A high-repetition-rate time-of-flight mass spectrometer (HRR-TOF-MS) was coupled to shock tube 2 (cf. Figure 4.20) in this work. The end-flange separating the driven section from the TOF-MS contains a precision manufactured conical nozzle (Frey Berlin) with a diameter of 60 μm . The large pressure ratio across the orifice is sufficient to ensure a supersonic jet forms as gas flows and expands through the nozzle. In order for the HRR-TOF-MS to be used in reaction kinetics studies, the TOF-MS has to be operated at highest repetition rates. Hence, the HRR-TOF-MS (Kaesdorf) was optimized for repetition rates up to 150 kHz by combining a compact design (short flight distance) with high transmission energies (high flight velocities). The resulting short flight times ensure no overlap of signals caused by ions from different consecutive ionization cycles. The TOF is equipped with both an electron impact (EI) ion source that constitutes a two stage ion extraction, and a two stage ion reflectron. The latter feature compensates for flight time differences due to different initial energies of the ions with the same mass up to a second order correction (approx. 8–10% of the mean energy of the distribution).

Commencing the data recording from the moment the shock passes the first pressure transducer provides some mass spectra information before the shock wave in the form of a sudden rise in the signal. This information helps to define the exact zero time of the arrival of the shock wave at the end wall. Using the following equation m/z is determined for each peak from its time of occurrence t .

$$\frac{m}{z} = a(t - b)^2 \quad (3.9)$$

The constants a and b are determined from calibration measurements with noble gas mixtures.

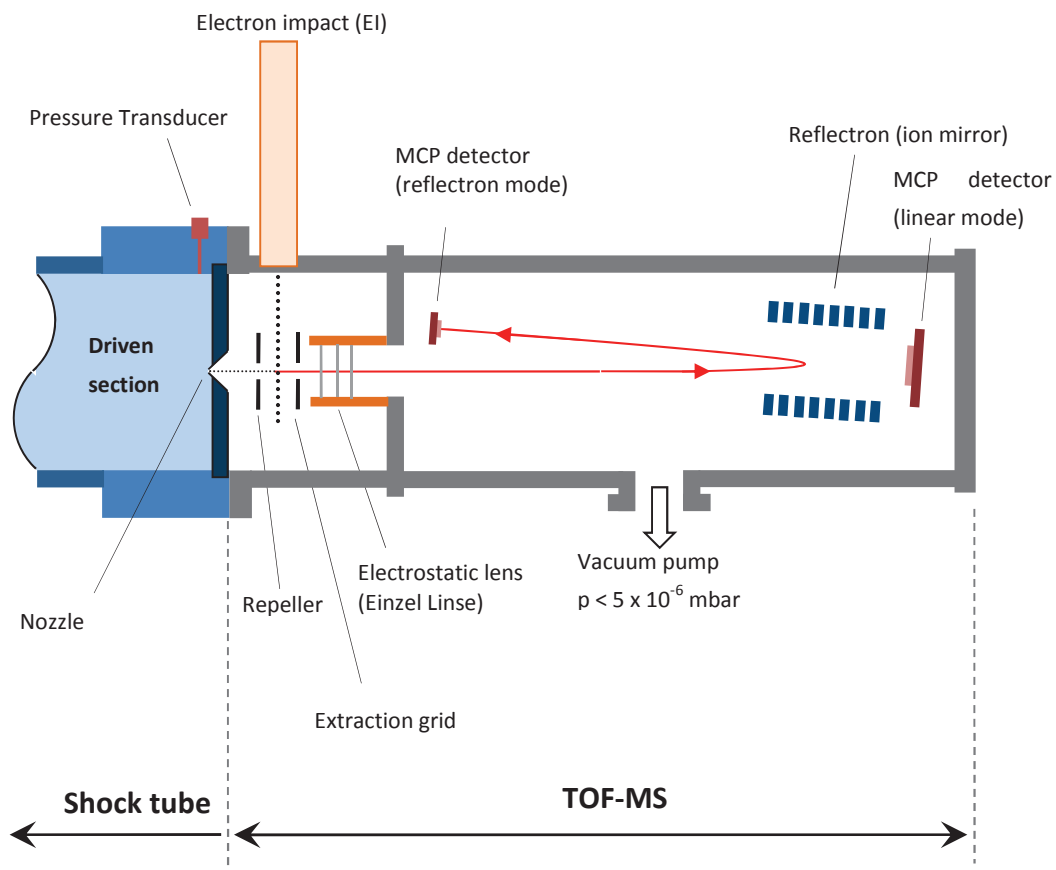


Figure 4.20: Arrangement of the TOF-MS at the shock tube

The energy of the ionizing electrons can be tuned from 5 to 85 eV. It is possible to ionize under field free conditions as ionization (200 ns – 2 μ s) and extraction (300 ns – several μ s, rise-time 10 ns) can be pulsed independently. The maximum kinetic energy of the ions is 10 keV which is high enough to result in detectable signals for molecular weights up to 1000 u, using the two stage MCP detectors. The HRR-TOF-MS is equipped with two detectors: one that is used in the reflectron mode (higher resolution) and one that can be used in the linear TOF mode (higher transmission and sensitivity). To avoid the negative influence of chemical ionization in the shock tube a positively charged lens deflects the negative ions from the molecular free jet. Further details about the experimental setup and the data acquisition system can be found in Dürrstein et al. [108].

4.4. Multiline NO-LIF thermometry in flow reactors

4.4.1. Fundamentals of multiline NO-LIF thermometry

Laser-induced fluorescence (LIF) imaging is a laser-based spectroscopic method used for quantitative and qualitative detection of selective species in the gas phase. The fundamental physical process can be simplified as shown in Figure 4.21. It is based on the quantum mechanical description of the interaction between an atom or a molecule and electromagnetic radiation. An incident laser photon excites the system by stimulated absorption from the ground state into the excited state. After some time (typically in the range of 1 – 100 ns), the system falls back from the excited state into the ground state through various depopulating processes, one of which is the radiative emission. Since the fluorescence intensity is dependent on parameters such as ground state population, chemical environment, pressure and temperature, LIF measurements have become an important tool in physical chemistry. Photon absorption in the visible and UV spectral range and appropriate fluorescence quantum yields enable species detection down to the parts-per-billion (ppb) range. Many combustion-relevant species such as OH, O₂, NO, CH, CN, NH, and C₂ can be accessed selectively [121]. Also, organic molecules such as ketones or atomic species (e.g. indium) are frequently used [122].

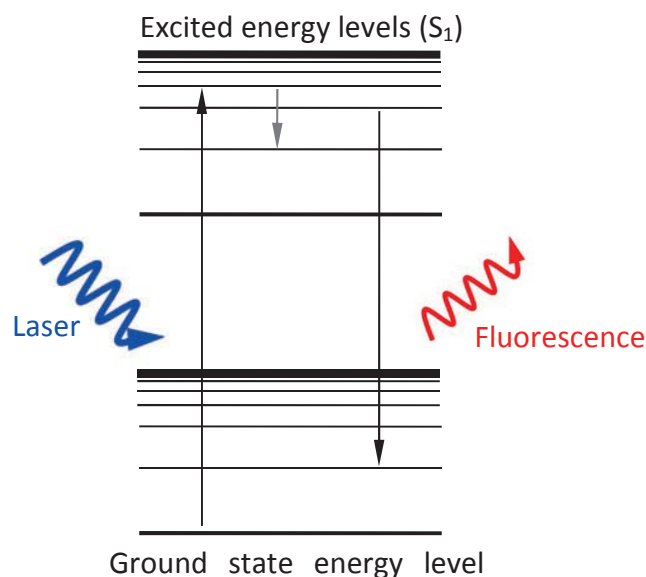


Figure 4.21: Fluorescence phenomenon using the diagram of the vibrational energy levels of an absorbing molecule

The multi-line LIF thermometry technique is based on the measurement of LIF excitation spectra of nitric oxide (NO). Nitric oxide is stable at room and higher temperatures, which gives NO the advantage of a wide measurement range for LIF thermometry. The NO molecule is non-polar and has a complex electronic structure. Laser-induced fluorescence imaging experiments involve a number of different electronic states with extensive fine structure: NO optical spectra show thousands of transitions in the UV range. A potential energy diagram of the NO molecule with the five lowest doublet electronic states is given in Figure 4.22. The ground state is termed X and the excited states are sorted alphabetically.

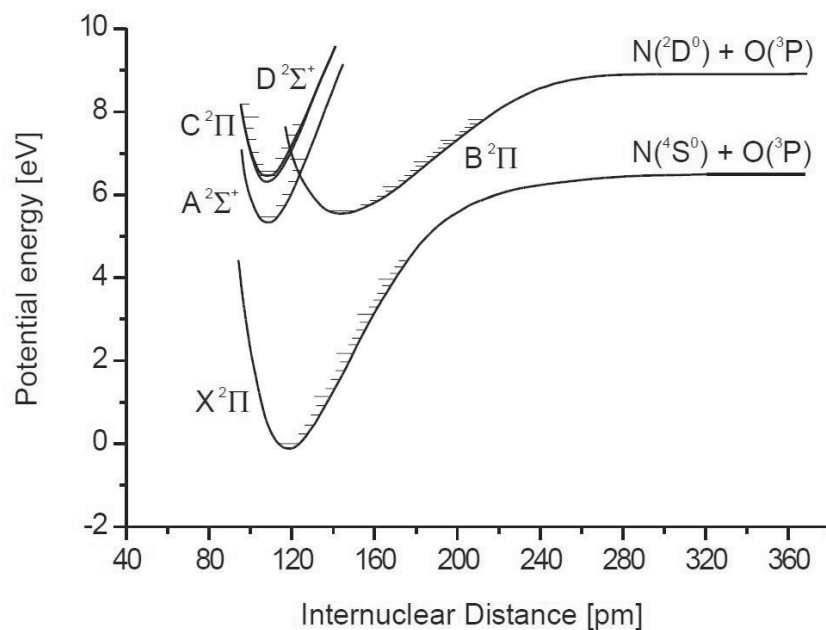


Figure 4.22: Potential energy diagram of NO [123]

This laser-based method enables remote imaging of the gas-phase temperature without introducing disturbances into the system. The applicable temperature range is 250 – 2500 K with an accuracy of better than $\pm 2\%$ [121, 122]. Moreover, the multi-line technique yields absolute temperatures without the need for calibration, which also makes it applicable in systems with comparably large background signal such as plasmas.

This thermometry technique is based on the temperature-dependent population of the rotational energy levels of the nitric oxide (NO) molecule. The species are either generated in the plasma flow itself, or added as a tracer molecule. The LIF excitation laser beam is formed into a light sheet and illuminates a plane in the area of interest. The pulsed laser is tuned over part of the NO A-X(0,0) electronic absorption band (γ -system), while for each wavelength position individual images of the induced fluorescence are recorded using an ICCD camera. From the resulting stack of images LIF excitation spectra can be extracted for

each pixel. LIFSIM [124] is used to fit simulated spectra to the experimental data with temperature, a broadband background as a baseline and signal intensity as free parameters.

In this work, the multi-line NO-LIF technique has been applied to a plasma for the first time. While several experiments were performed with addition of 1000–4000 ppm of NO as a tracer, some experiments used the naturally formed NO when operating oxygen/nitrogen plasmas. The spectral range chosen for the excitation was between 225.19–225.10 nm ($44406\text{--}44425\text{ cm}^{-1}$). Figure 4.23 shows spectra for two different temperature regions. Note the significant change of prominent spectral features with temperature making this spectral section ideal for sensitive temperature measurements.

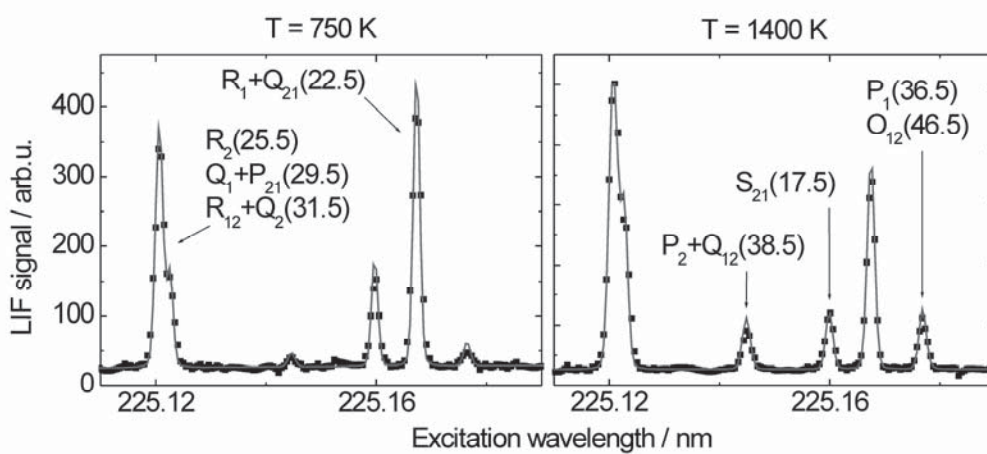


Figure 4.23: Experimental NO excitation spectra (solid symbols) and spectral fit (solid line) obtained from regions in the plasma exhibiting significantly different temperatures [124]

For each spectra an excitation scan over 191 wavelength positions at equal spectral intervals of 0.1 cm^{-1} was performed. Each wavelength position was averaged over 30 instantaneous laser shots. The full image data set is acquired within 10 minutes.

4.4.2. Multiline NO-LIF-technique at a low-pressure premixed flame reactor

Multiline NO-LIF thermometry was previously utilized by Kronmayer and Ifecho in the same low-pressure $\text{H}_2/\text{O}_2/\text{Ar}$ premixed flame reactor. Detailed information can be found in Kronmayer et al. [121, 122]. Their results show temperature profiles for a hydrogen flame with flame equivalence ratios of 0.375 and 0.667 at HAB from 0 to 180 mm. The reactor conditions during the measurements were $p = 30\text{ mbar}$ and mass flow rates of hydrogen, oxygen and argon were 600, 800 and 400 sccm, respectively. The measurements show maximum temperatures between 1250 and 1375 K depending on the equivalence ratio.

4.4.3. Multiline NO-LIF technique at the microwave-plasma reactor

The aim of these experiments was to measure the gas temperature downstream of the microwave-antenna in the plasma-reactor and to understand the influence of the main parameters on the plasma. In addition, the effect of precursor in the inlet gas mixture was studied. Details about the setup of the microwave-plasma reactor have been explained in section 4.2.1.3. For this experiment the microwave-plasma reactor was simplified as much as possible to ease studying and understanding the influence of the main parameters such as reactor pressure and microwave power on the NO-rotational temperature (Figure 4.24). The reactor in this case consists mainly of a microwave-antenna, quartz tube with 30 mm outer diameter and 2 mm wall thickness and a rotary vacuum pump. The delivery of the gaseous TEOS into the reactor was achieved using a bubbler system.

A tunable KrF*-excimer laser (248 nm) is frequency-shifted to 225 nm in an 8 bar H₂ Raman cell. The laser beam is formed using a cylindrical lens $f = 500$ mm to form a light sheet that measures 20 mm high and 5 mm thick and illuminates a horizontal plane coaxially in the quartz tube. The NO molecules are excited in the A-X (0,0) band and the LIF-signal is recorded with the intensified CCD-camera (LaVision). A 235–250 nm reflection band pass filter blocks both stray light from the laser and the plasma glow. The quartz tube allows optical access to the plasma region in the UV and visible spectral range, while the light sheet is directed into the reactor from a window at the downstream end (cf. Figure 4.24). The camera is mounted perpendicular to the quartz tube centerline to image a rectangular spatial region of size 38×20 mm² downstream of the antenna exit as indicated in Figure 4.24.

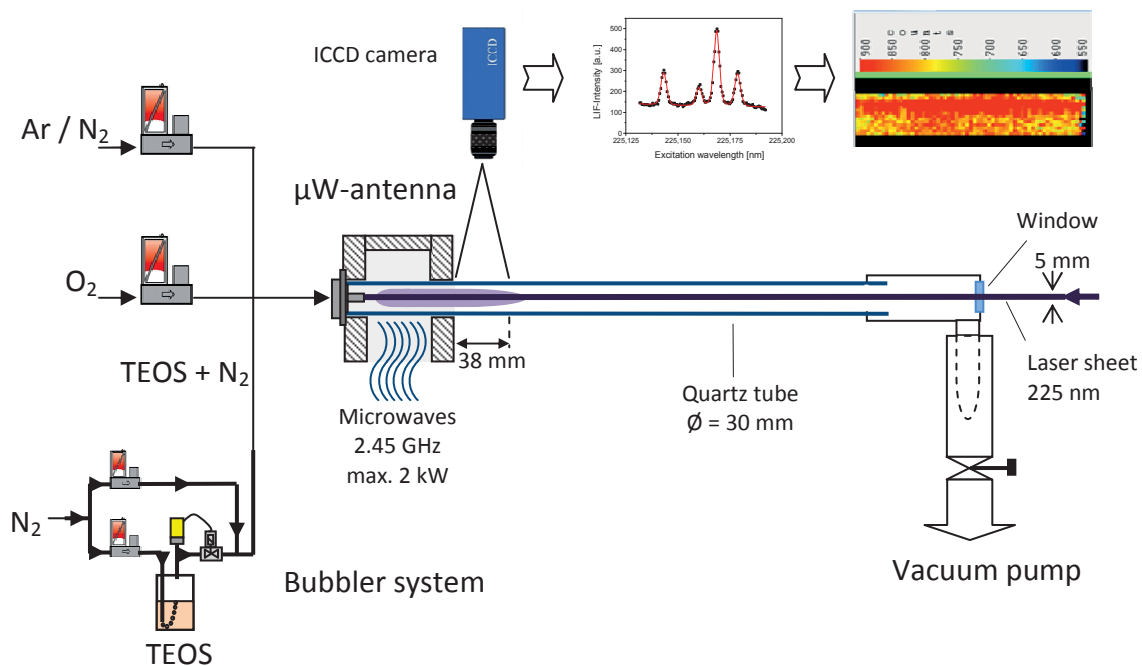


Figure 4.24: Simplified schematic illustration of the experimental setup of the NO-LIF thermometry on the microwave-plasma reactor without co-flow

5. Results and discussion

5.1. Kinetics studies of precursor decomposition and oxidation in shock-tube experiments

5.1.1. Tetraethoxysilane (TEOS)

5.1.1.1. Studying the decomposition kinetics of TEOS using TOF-MS at the shock tube

The gas-phase precursor chemistry and subsequent steps such as nucleation and particle growth define the final particle properties. In order to understand the underlying process of the precursor decomposition kinetic in more detail, which is essential for simulations of the particle formation, the decomposition of TEOS was investigated with high-repetition-rate time-of-flight mass spectrometry (HRR TOF-MS) in shock-tube experiments. With this device it is possible to obtain the time history of the concentration of many species simultaneously with an acceptable time resolution within a test time of approximately 2 ms. The decomposition of TEOS was investigated in the temperature range between 1330 and 1590 K. Mass spectra in the range up to 250 u were taken every 10 μ s.

Commencing the data recording from the moment the shock passes the first pressure transducer (cf. Figure 4.17) provides some mass spectra information before the incoming shock wave in the form of a sudden rise in the signal. This information helps define the exact zero time (t_0) of the arrival of the shock wave at the end wall. Figure 5.1 shows raw data obtained by the TOF-MS. The steep rise in intensity at approximately 500 μ s is due to the compression induced by shock arrival.

Figure 5.1 shows the raw signal of 150 subsequent mass spectra in the time domain. In order to identify the peaks in the individual mass spectra, the time domain (time-of-flight) must be converted to mass. Equation 3.9 in section 4.3.3 explains the relationship between the mass m of an ion and the time t taken for the ion of a given charge z to travel for a fixed distance. The constants a and b can be determined from the measured t for the known m/z . Xe is usually used for the mass calibration of a and b . With the mass resolution of the apparatus it is easy to distinguish the xenon isotopes ($m/z = 128, 129, 130, 131, 132, 134, 136$) that are separated by either one or two atomic mass units. Additionally, fragments of CCl_4 can be considered for calibration. Figure 5.2 shows a calibration curve that contains a wide range of masses between 12 for carbon and 136 for Xe. This was achieved by measuring each gas separately at room temperature (without shock). The measurement of carbon atoms at mass 12 was achieved from fragmentation of CCl_4 . The resulting values of a and b from the fitting

shown in Figure 5.2 are 2.5127 and 0.1843, respectively. It should be noted that the electron energy has no influence on the time-to-mass calibration. Increasing the electron energy increases the ionization and thus leads to stronger signal but also increases fragmentation.

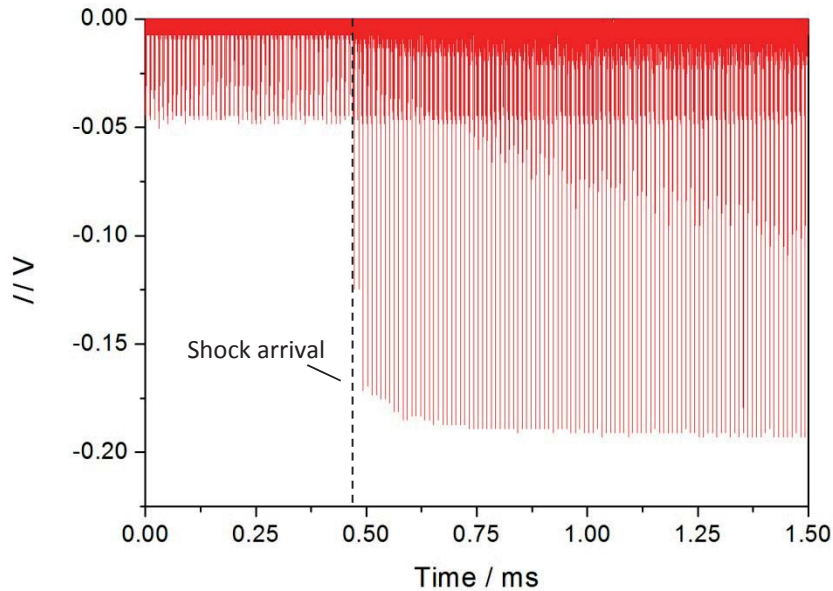


Figure 5.1: Raw TOF-MS data represents a series of individual mass spectra. The mixture is 0.5% TEOS and 0.5% Ar in Ne, $p_5 = 1.46$ bar and $T_5 = 1410$ K. Nozzle diameter: 45 μm , Electron energy: 45 eV, repetition rate: 100 kHz, data span: 1.5 ms

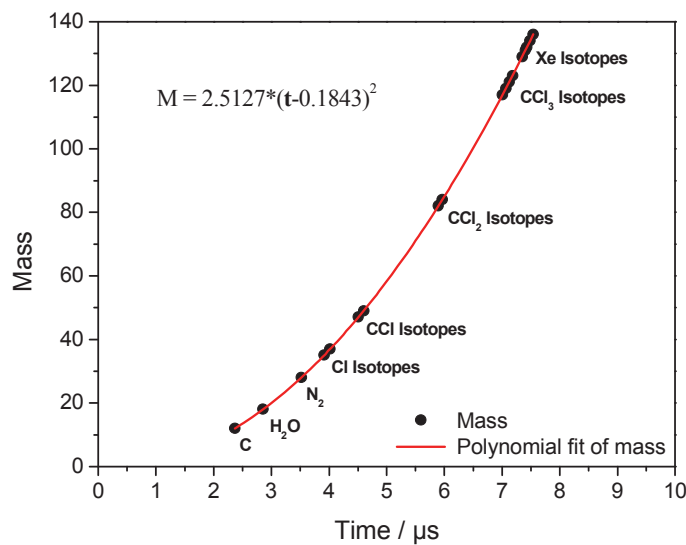


Figure 5.2: Time-to-mass calibration curve

A single spectrum of the fragments from TEOS decomposition and their reaction products is shown in Figure 5.3 in the time domain. This figure shows a single scan (10 μs) from 200 repetitive measurements extracted from the raw data (Figure 5.1) at 1.25 ms. Using the cali-

bration procedure described before the spectrum in Figure 5.3 can be converted into mass spectrum as shown in Figure 5.4.

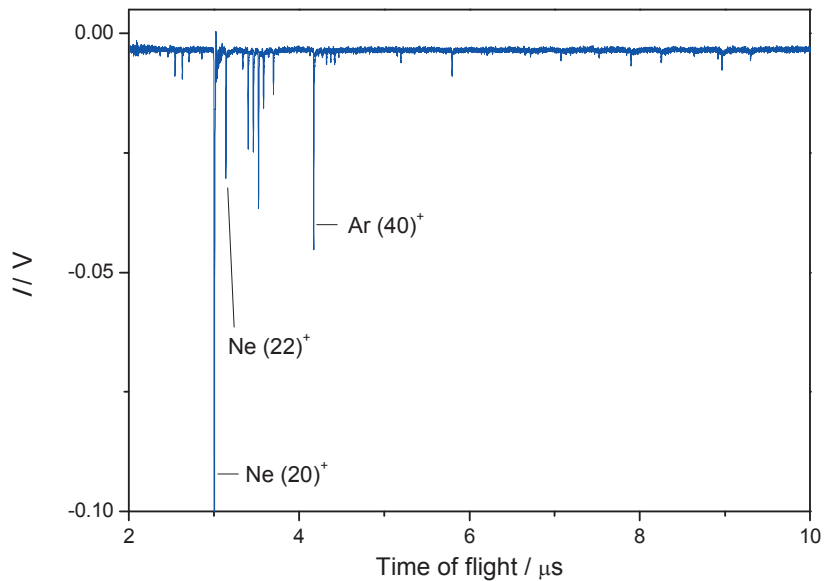


Figure 5.3: Mass spectrum from Figure 5.1 as function of time. The mixture is 0.5% TEOS and 0.5% Ar in Ne, $p_5 = 1.46$ bar and $T_5 = 1410$ K. The spectrum is for 0.75 ms after the arrival of the shock wave. Nozzle diameter: 45 μm . Electron energy: 45 eV, repetition rate: 100 kHz

Figure 5.4 shows a single spectrum from the pre-shock region (at T_2) from the same experiment. In the pre-shock spectrum in addition to the peaks representing neon at $m/z = 20$ and 22 and argon at $m/z = 40$ a wide range of species that are produced due to the fragmentation of TEOS during ionization can be seen. These peaks for TEOS match the mass spectrum of TEOS given in the NIST data base [126]. In addition to these peaks, the mass spectrum from the post-shock region shows a large number of new peaks in the range between $m/z = 12$ and 46. These peaks reveal the species that are produced during the thermal decomposition of TEOS in the shock tube. The masses that receive additional signal due to electron impact fragmentation of TEOS must be corrected for the respective signal contribution.

The post-shock spectrum up to $m/z = 47$ is presented and the species generated during the fragmentation of TEOS are labeled in Figure 5.5. The data show that the strongest peak is at $m/z = 28$, which reveals ethylene to be the main product of TEOS decomposition. Ethylene cannot be a fragmentation product since the ionization and extraction in the TOF-MS occurs rapidly inhibiting any isomerization process that could take place in the ion optic or in the drift region. The delay between the ionization and extraction was about 1 μs . According to the single-pulse shock-tube studies of Herzler et al. [36], in addition to ethylene a substantial amount of ethanol in the reaction products is observed. However, the peak corresponding to ethanol, at $m/z = 46$, is very weak which can be correlated to the fast fragmentation of etha-

nol. Instead of $m/z = 46$ an additional peak can also be seen at $m/z = 45$ that is attributed to C_2H_5O .

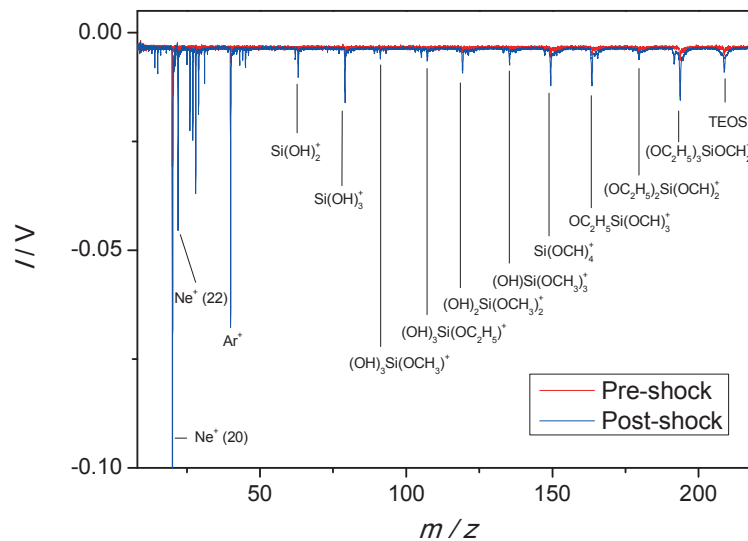


Figure 5.4: TOF-mass spectra of pre-shock (red) and post-shock (blue) conditions. $T_5 = 1410$ K, $p_5 = 1.46$ bar, 0.5% TEOS + 0.5% Ar in Ne

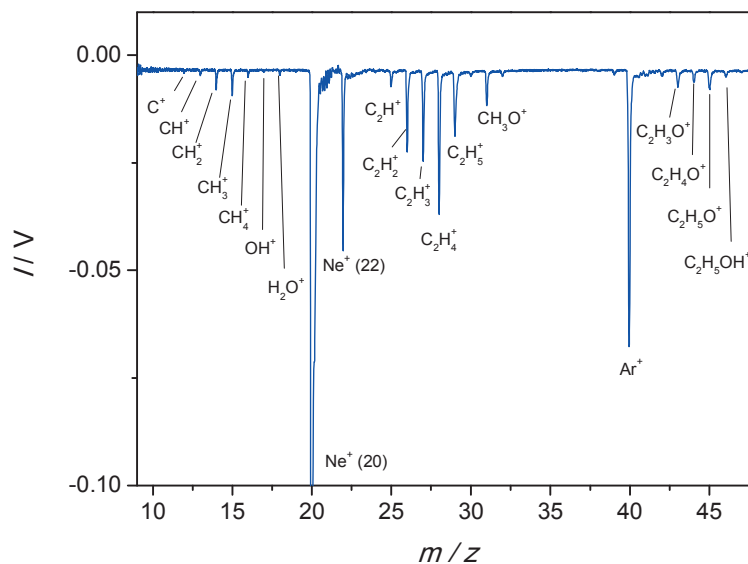


Figure 5.5: Post-shock TOF mass spectrum of the products detected from decomposition of TEOS. The initial gas mixture contains 0.5% TEOS + 0.5% Ar in Ne. $T_5 = 1410$ K, $p_5 = 1.46$ bar, electron energy: 45 eV

The raw data were converted into intensity-time profiles by integrating the peak area of different species (i.e., m/z values). There were almost 150 repetitive measurements for each

species during every run. Using software developed by the Olzmann group [127] the variation of the intensity of each species was plotted as a function of time.

The intensity histories that are investigated for clarifying the reaction kinetics in the shock tube are then deduced from the mass information of a series of runs of the mass spectrometer with the time resolution of the repetition rate of the ionization. The latter is limited by the flight time of heaviest ions that are detectable to prevent overlapping of heavy and light ion signals of subsequent measurements. Figure 5.6 shows the intensity-time profile for the internal standard (Ar). The use of internal standards is necessary since the free-jet is non-stationary due to the rapidly changing boundary conditions once the shock arrives at the nozzle leading to an initial signal increase for all masses. For correction, all the species signal profiles are therefore divided by the Ar signal intensity profile. Before the correction, the Ar signal is fitted with a polynomial function to avoid deterioration of the signal-to-noise ratio of the measured species signals by the scatter of the Ar signal. In the diagram the time of the shock arrival has been set to 0.

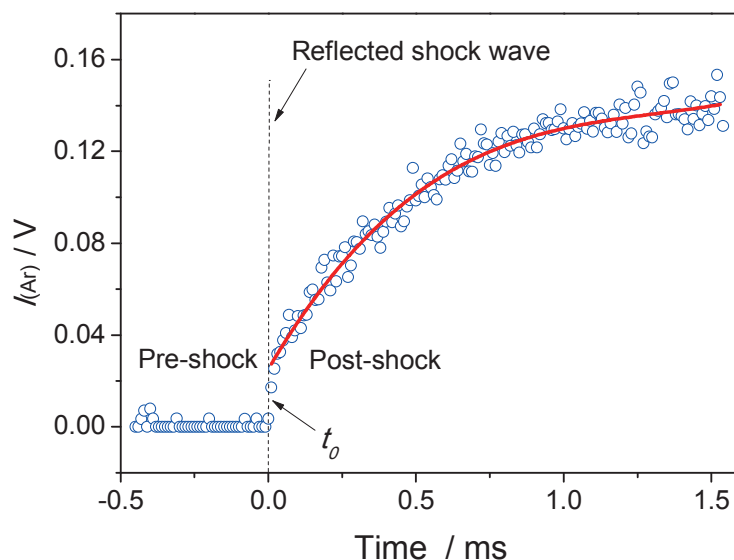


Figure 5.6: Ar peak intensities as a function of time for an experiment with 0.5% TEOS and 0.5% Ar in Ne, $p_5 = 1.46$ bar and $T_5 = 1410$ K. Nozzle diameter: 45 μm . Electron energy: 45 eV, repetition rate: 100 kHz

As an example Figure 5.7a shows the not normalized intensity-time profile of TEOS extracted at $m/z = 208$. In Figure 5.7a the shock arrival can be recognized at the point of the sudden increase of the signal intensity. Figure 5.7b shows the corrected values of the species using the polynomial fit of the Ar signal. The resulting intensity-time profile during TEOS decomposition is shown in Figure 5.7b. It can also be seen that the base line of the decomposition

profile is quite high. This could be due to the fact that the ion optics in the TOF-MS are not pumped.

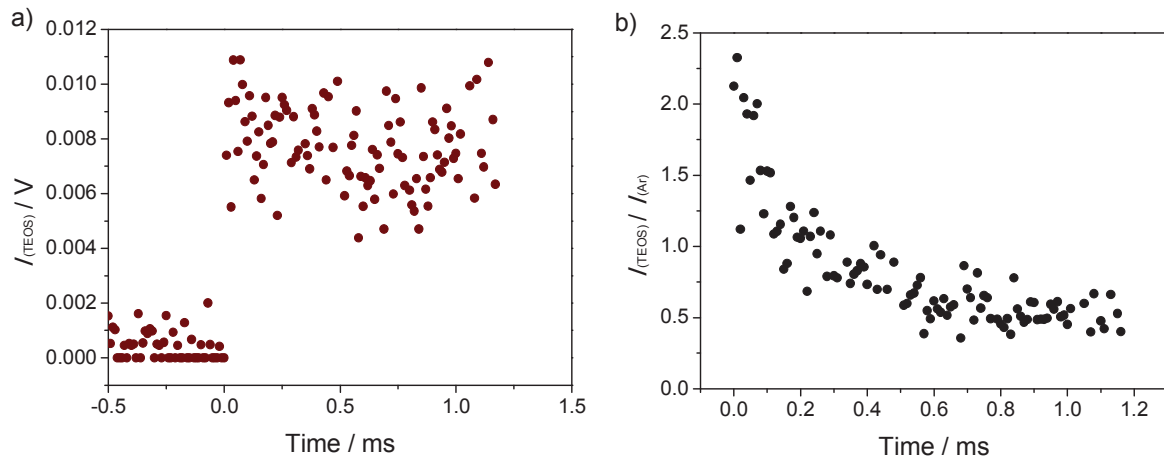


Figure 5.7: a) Peaks intensities of TEOS as function of time, b) TEOS intensity normalized with the Ar signal. $T_5 = 1410$ K, $p_5 = 1.46$ bar, 0.5% TEOS + 0.5% Ar in Ne

For the comparison of the TOF-MS measurements with literature, CHEMKIN simulations using the TEOS decomposition mechanism of Herzler et al. [36] as well as the mechanism of Kraft and co-workers [38] were carried out for our experimental conditions. Figure 5.8 shows a comparison between the measured TEOS decay from TOF-MS measurements at $m/z = 208$ with the CHEMKIN simulations. The measured TEOS intensity in Figure 5.8 calibrated with the initial TEOS concentration of 0.5%. Figure 5.8 shows that the decomposition rates predicted by the Herzler et al. mechanism [36] as well as the Kraft et al. mechanism [38] are obviously faster than the experimentally observed ones. This also could be due to the lack of time resolution of the instrument or due to the rest signal at longer reaction times.

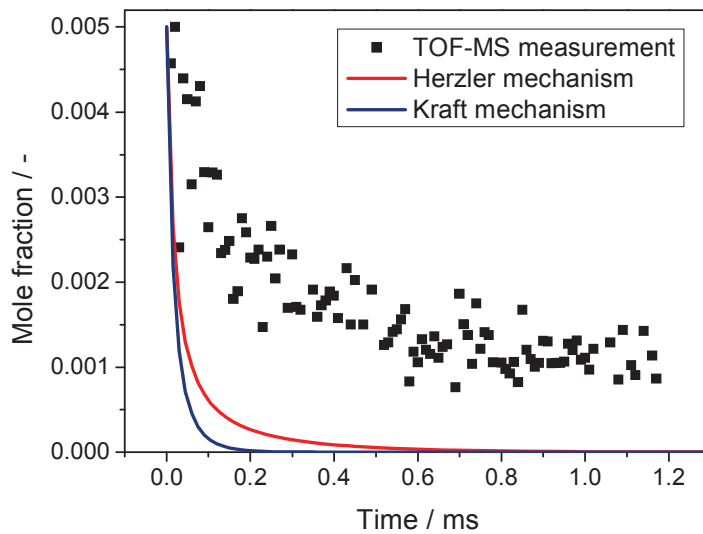
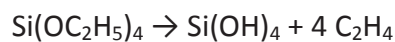


Figure 5.8: Comparison of TEOS decay between the TOF-MS measurements and CHEMKIN simulations using Herzler et al. [36] and Kraft et al. [38] mechanisms. $T_5 = 1410$ K, $p_5 = 1.46$ bar, 0.5% TEOS + 0.5% Ar in Ne

Comparisons of measurements and simulations of the TEOS decomposition for the conditions presented in Figure 5.4–5.10 are plotted in Figure 5.9. Figure 5.9a shows that the simulated concentration of SiO_2 from Herzler’s mechanism [36] reaches a maximum of almost 10% of the initial TEOS concentration and the amount of silicic acid formed is negligible. Moreover, the simulated profiles with the Kraft et al. [38] mechanism [38] are shown in Figure 5.9b. It shows a continuous increase in the silicic acid formation at a slow rate. A longer time (e.g., 10 ms) of the Kraft mechanism predicts that silicic acid concentration almost reaches the value of the initial TEOS concentration and the final concentration of ethylene is almost four times higher. This is because the decomposition model is based mainly on the removal of terminal C_2H_4 from each ethoxy branch to form ethoxysilanes $\text{Si}(\text{OH})_x(\text{OC}_2\text{H}_5)_{4-x}$ and ultimately $\text{Si}(\text{OH})_4$. Therefore, the decomposition of TEOS after a longer time (e.g., 10 ms) can be approximately simplified to the following chemical equation



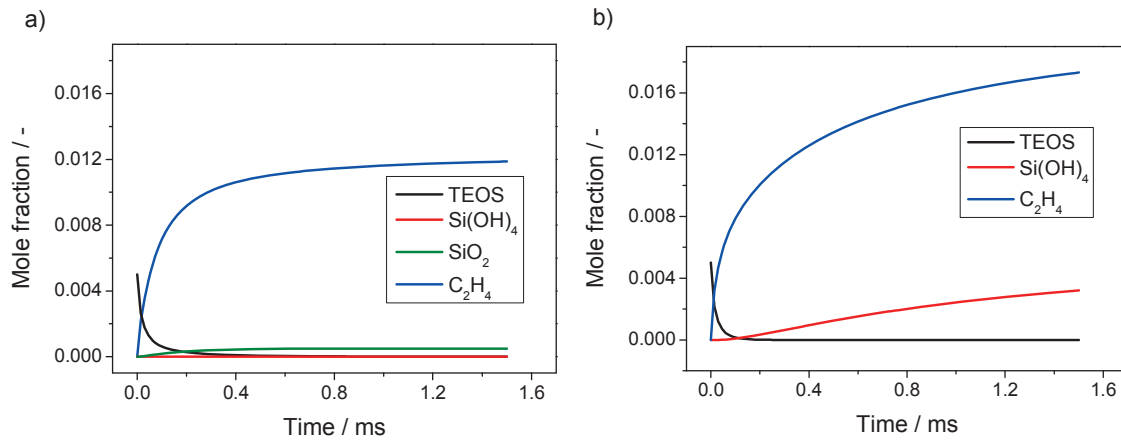


Figure 5.9: Simulated concentration histories of some species that are produced from TEOS decomposition using a) Herzler et al. [36] and b) Kraft et al. [38] mechanisms at 1410 K, 1.46 bar and 0.5 % TEOS

The previous simulations show a slight difference in the concentration of ethylene, but large difference in the Si-containing molecules that are produced from TEOS decomposition. Herzler et al. [36] measured in their study the yield of ethylene and ethanol. Therefore, concentration-time profiles of ethylene and ethanol ($m/z = 28$ and 45) from TOF results are presented in Figure 5.10. Furthermore, a CHEMKIN simulation using the GRI mechanism that was assembled with the TEOS decomposition mechanism of Herzler et al. [36] was carried out under the same conditions. The measured relative concentrations of ethylene and ethanol were normalized to their simulated concentrations at 1.2 ms. Figure 5.10 shows a good agreement of the measurements with the simulation. However, in the measurements the formation of ethanol begins at 0.2 ms, while the simulation predicts an earlier onset. This behavior was also recognized by all the TOF experiments with TEOS.

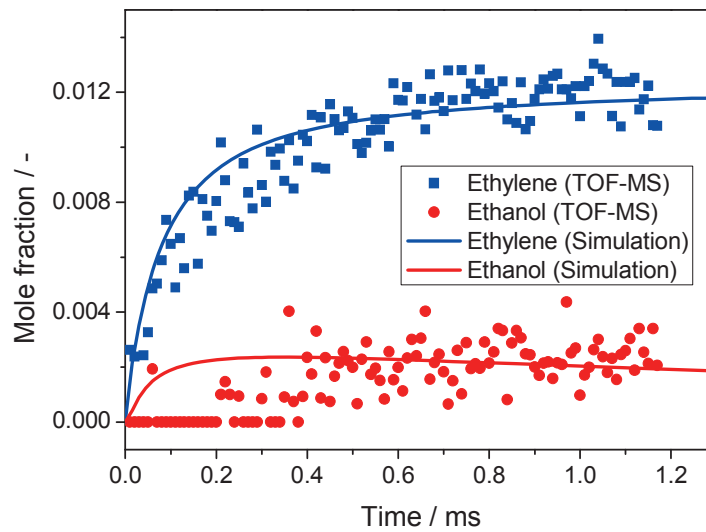


Figure 5.10: Concentration-time profiles of ethylene (blue squares) and ethanol (red circles) behind the reflected shock wave for an experiment at $T_5 = 1410$ K and $p_5 = 1.46$ bar. The blue and red lines are from CHEMKIN simulations of TEOS under the same conditions

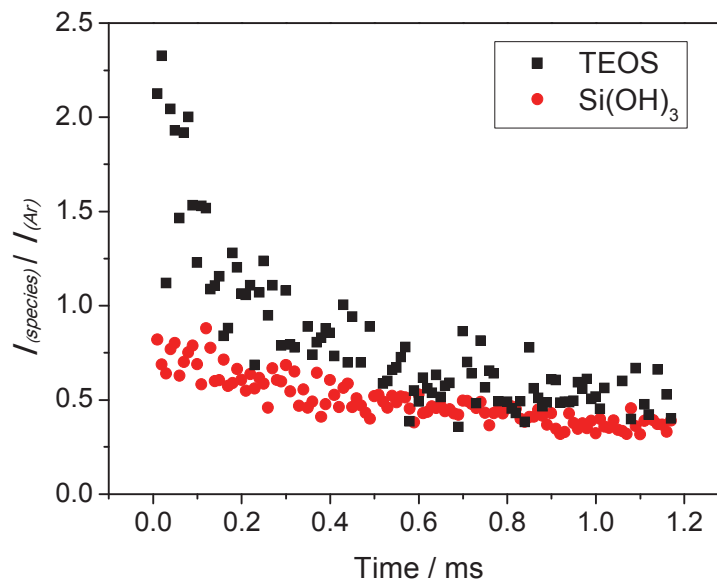


Figure 5.11: Normalized intensity profiles of TEOS and $\text{Si}(\text{OH})_3$. $T_5 = 1410$ K, $p_5 = 1.46$ bar, 0.5% TEOS + 0.5% Ar in Ne

The TOF results do not show any new peak of silicon containing species in the post-shock mass spectra under these conditions. The concentration of the Si-containing species are either below the detection limit of our TOF-MS or the reaction is too slow to generate significant concentrations within the test time of 1.2 ms. Furthermore, several peaks of Si-containing species were detected, nonetheless these peaks also appeared in the pre-shock TOF mass spectra. For example, $\text{Si}(\text{OH})_3$ was detected at $m/z = 79$. This signal at $m/z = 79$

exhibits a slower rate of decay than TEOS (cf. Figure 5.11) and appears to originate from other species than the TEOS signal. This species could have been formed from the cleavage of one hydroxyl group from silicic acid $\text{Si}(\text{OH})_4$ in the ionization zone of the TOF-MS. This results can be an indication of the formation of $\text{Si}(\text{OH})_4$ from TEOS decomposition as Kraft et al. [38] suggested.

5.1.1.2. Ignition delay times of TEOS

The objective of the experiments is to determine the ignition delay time of TEOS/air mixtures as a function of temperature. Ignition delay times of TEOS were measured by observing OH^* chemiluminescence and pressure increase behind the reflected shock wave in shock-tube experiments. A typical measurement at these quantities that allows the ignition delay time to be determined is shown in Figure 5.12. To eliminate the influence of pressure on the experimental results all experiments were carried out at the same pressure ($p = 10$ bar). All ignition delay times shown in this work were determined by extrapolating the steepest increase of the OH^* -emission signal to its zero value on the time axis.

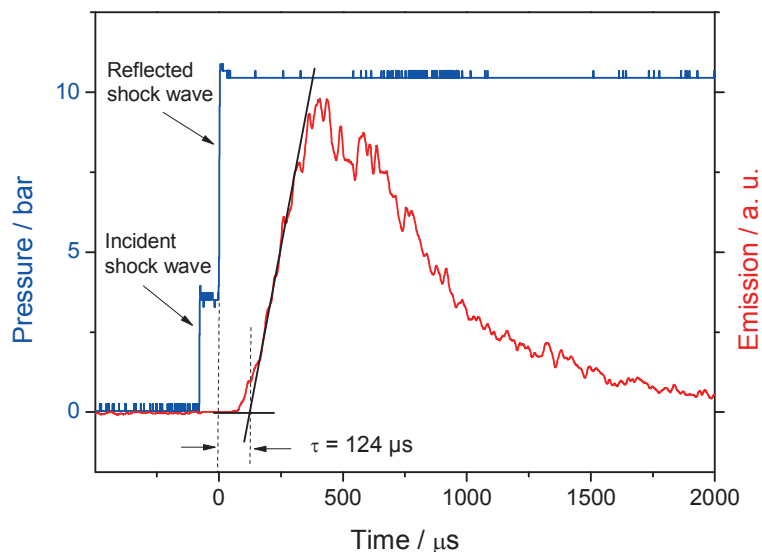


Figure 5.12: Determination of the ignition delay time from the rise in OH^* chemiluminescence from TEOS for an experiment with $T_5 = 1206$ K, $p_5 = 10.4$ bar. The pressure trace (blue line) shows the step-wise increase after the incident and reflected shock waves. An ignition delay time of $124 \mu\text{s}$ was determined under these conditions

The results for mixtures of 1600 ppm TEOS in dry synthetic air show that the ignition delay time strongly depends on temperature (Figure 5.13). The ignition-delay time of TEOS follows an Arrhenius-like relation and can be given as:

$$\tau = 5.86 \times 10^{-9} \exp(28800 \text{ K}/T) \mu\text{s} \quad (5.2)$$

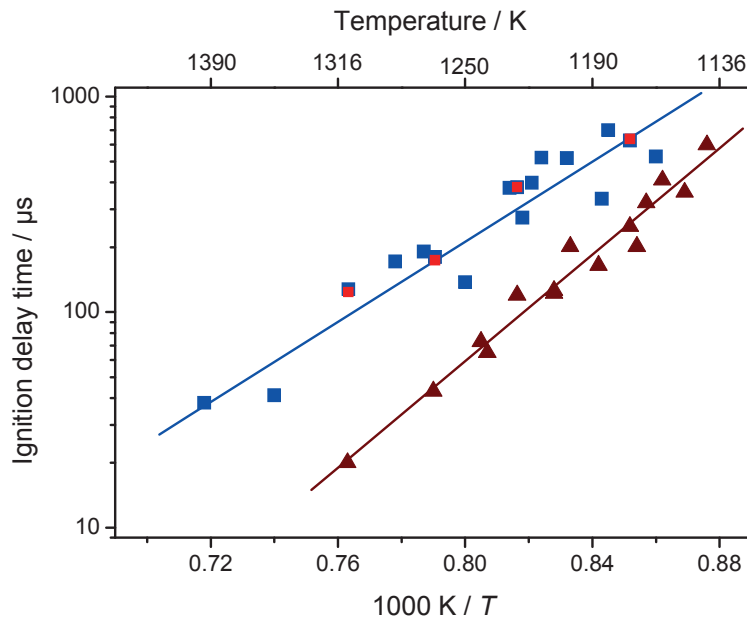


Figure 5.13: Ignition delay times of TEOS in dry synthetic air (brown triangles), synthetic burnt gas (blue squares) and moist synthetic air (red squares) at 10 bar

In practice, the initiation of the precursor reaction in gas-phase processes can be achieved, e.g., by plasma or convective heating in dry gas, or with hot burnt gases from burners that contain high levels of moisture and CO_2 . Therefore, the measurement of ignition delay times of 1600 ppm TEOS was studied in a gas mixture that is similar to the burnt gas composition of lean methane flame with equivalence ratio $\phi = 0.45$. Details of the initial gas mixture are given in Table 5.1 (mixture 2). Results of the ignition delay times are presented in Figure 5.13. This figure shows that the presence of H_2O and CO_2 in the initial gas mixture increases the ignition-delay time by almost one order of magnitude at 1300 K. In order to investigate whether the presence of CO_2 or H_2O has the influence for increasing the ignition delay times of TEOS a third gas mixture that contains only H_2O beside TEOS, O_2 and N_2 , but no CO_2 was prepared (cf. Table 5.1). The results of the ignition delay time experiments with the third mixture (see the red squares in Figure 5.13) show a good agreement with the results of the second mixture. This indicates that it is the water that increases the ignition delay times of TEOS, regardless of the presence of CO_2 . Therefore, the data obtained for TEOS in moist synthetic air are considered to represent the ignition delay time behavior of the case with exhaust gas. The ignition-delay time of TEOS as a function of temperature in moist synthetic air can be given by the following expression:

$$\tau = 7.76 \times 10^{-6} \exp(21400 \text{ K}/T) \mu\text{s} \quad (5.3)$$

Table 5.1: Gas composition of test condition 1: TEOS in dry synthetic air, 2: TEOS in gas with a composition that represents the exhaust gas of a lean methane/air flame ($\phi = 0.45$), 3: TEOS in moist synthetic air

Mixture	Volume concentrations / %				
	TEOS	O ₂	N ₂	CO ₂	H ₂ O
1	0.16	20.92	78.92	0	0
2	0.15	11.0	75.35	4.5	9.0
3	0.15	15.0	75.85	0	9.0

To rule out that reactions between water vapor and TEOS take place during the mixing time at room temperature (approximately 1 hour), stability measurements were carried out. The stability of TEOS in moist gas mixtures was investigated with FTIR spectroscopy. The testing gas mixture was prepared in glass tubes, which were previously pumped down to 10^{-6} mbar. The chemical composition of a fresh mixture (3.5 mbar TEOS, 1.2 mbar H₂O diluted in 570 mbar He) was investigated with FTIR after 30, 75, and 135 min indicating negligible decrease in TEOS concentration or formation of products. The results are shown in Figure 5.14. It can be seen that the spectrum remains almost unchanged even after 2 hours. A minor absorption band near 1000 cm^{-1} is assigned to ethylene and is considered minimal and does not increase with the time. Ethanol was not detected at all under these experimental conditions. The absorption at 2250 cm^{-1} (CO₂) is due to the impurity from the air. Therefore, it can be concluded that TEOS was stable in the presence of moisture during the mixing time before starting the shock-tube experiments.

To clarify the influence of moisture on the ignition-delay time, measurements were performed at various temperatures and different amounts of water vapor. Figure 5.15 shows the results obtained at four different temperatures and water concentrations from 0 to 12% by volume. The data points shown in Figure 5.15 have a temperature variation of ± 3 K around the indicated value that is due to the scatter in temperature for all subsequent shock-tube experiments at the same test conditions. It can be seen that even traces of water in the gas mixture increase the ignition delay times significantly, up to an order of magnitude. Moreover, at water concentrations above 2% no further increase in ignition delay time was observed.

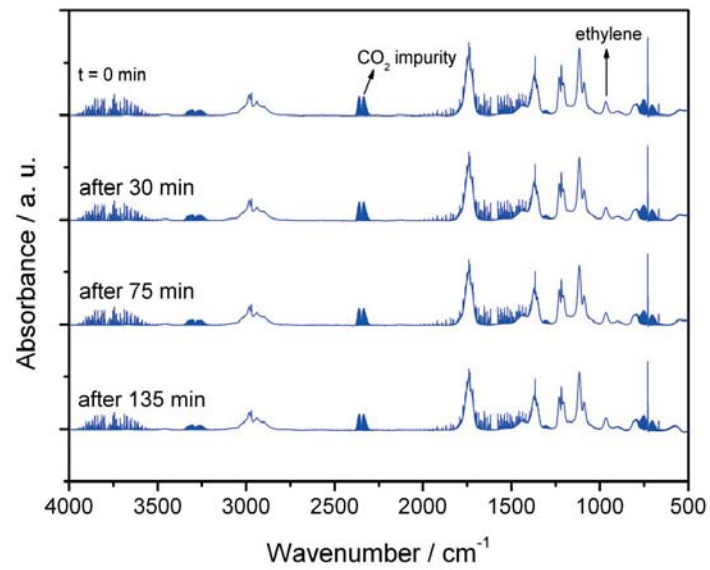


Figure 5.14: FTIR absorption spectrum of a TEOS/H₂O/He mixture obtained immediately after mixing and at various residence times at room temperature [128]

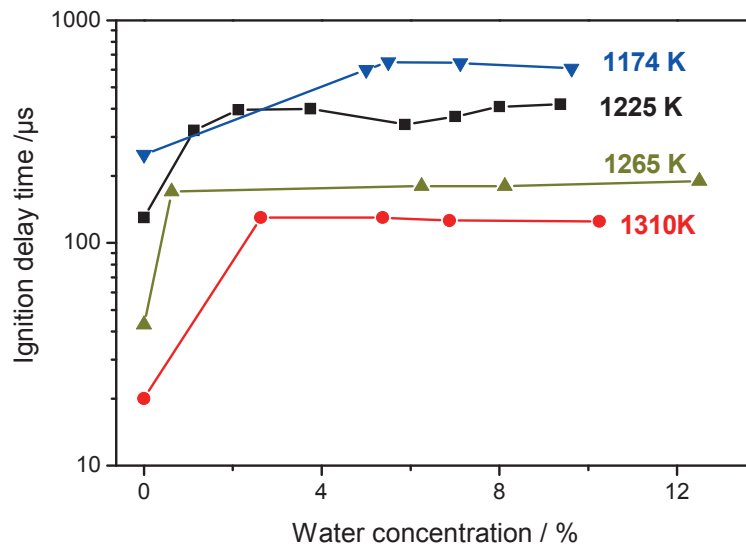


Figure 5.15: Ignition-delay times of TEOS as a function of water concentration at various temperatures: The lines show the average values of measurements in moist synthetic air.

5.1.2. Hexamethyldisiloxane (HMDSO)

HMDSO has been investigated additionally for the comparison with TEOS and as an alternative precursor for the gas-dynamically induced silica nanoparticles in the GIP reactor (cf. section 4.2.3).

5.1.2.1. Studying the decomposition kinetics of HMDSO in the shock tube via TOF-MS

Due to the lack of detailed kinetics knowledge of HMDSO decomposition, shock-tube experiments were required. The thermal decomposition of HMDSO was investigated in the temperature range between 1300 and 2150 K and at pressures between 0.97 and 1.65 bar. The measurements were performed with 0.5% HMDSO and 1% Ar as internal standard diluted in Ne as the bath gas. Further TOF-MS experiments were carried out to investigate the influence of oxygen during the reaction.

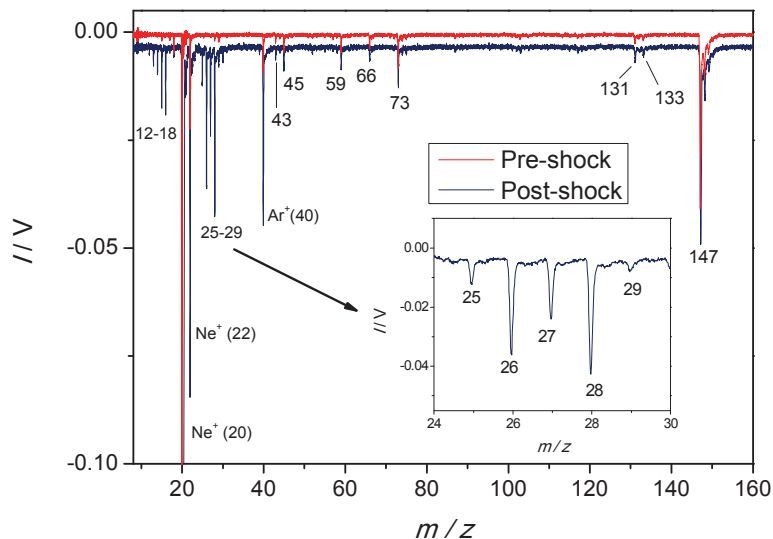


Figure 5.16: TOF-mass spectra of pre-shock (red) and post-shock (blue) conditions. Insert: zoomed part of the post-shock spectrum. The gas mixture contains 0.5% HMDSO + 0.4% Ar in Ne. $T_5 = 1650$ K and $p_5 = 1.31$ bar

A pre-shock spectrum of HMDSO and an averaged TOF mass spectrum (10 mass spectra after 1.0 ms of the shock arrival) of HMDSO decomposition at 1650 K behind the reflected shock wave are presented in Figure 5.16. Both mass spectra show a single high peak at $m/z = 147$, representing pentamethyldisiloxane (PMDSO) $\text{Si}_2\text{O}(\text{CH}_3)_5^+$. This is due to the cleavage of one methyl group in the ionization chamber. As also found by Carles et al. [45] in plasmas, the main initial decomposition path is the fast cleavage of a CH_3 group giving masses 15 and 147. This is in agreement with the results of Basner et al. [129] and Wavhal et al. [44]. Therefore,

the peaks at $m/z = 147$ were used to monitor the HMDSO concentration during decomposition.

The raw TOF data were post processed and the signal intensities of HMDSO and its product species were corrected for temporal variations with argon in the same manner as for TEOS as described in section 5.1.1.1. Additionally, calibration measurements were carried out for various HMDSO pressures at room temperature. Figure 5.17a shows a linear behavior between the peak area and partial pressure ratios of HMDSO to argon. A calibration factor can be extracted, which can then be used to convert the TOF-MS signals of HMDSO into the absolute concentrations as shown in Figure 5.17b.

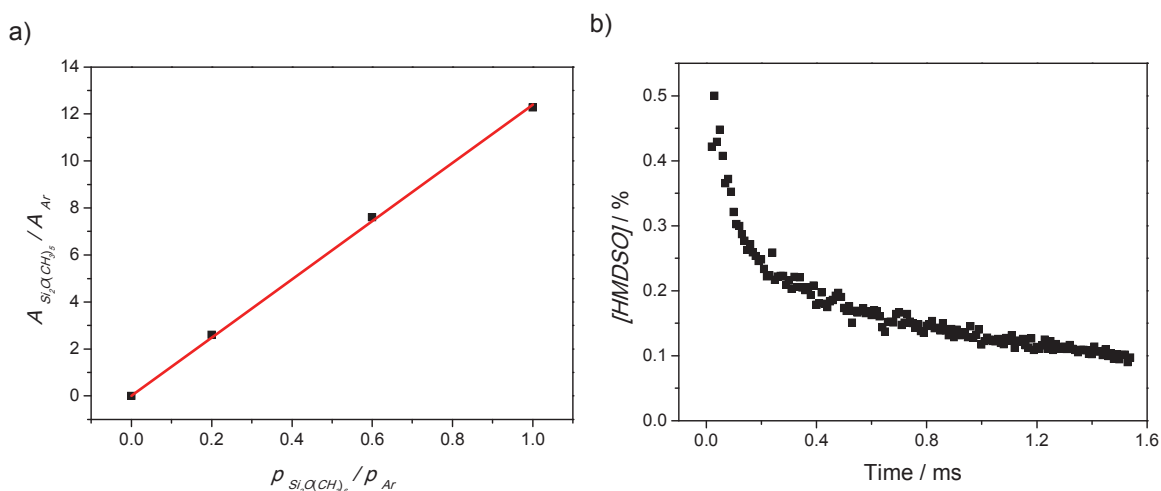


Figure 5.17: a) Calibration diagram for the determination of absolute HMDSO concentrations. Electron energy: 45 eV, repetition rate: 100 kHz. b) Concentration history of HMDSO decomposition (at $m/z = 147$). $T_5 = 1654$ K. Initial gas mixture contains 0.5% HMDSO and 1% Ar diluted in Ne

The post-shock TOF-mass spectrum in Figure 5.16 also shows a wide range of species from the decomposition of HMDSO between $m/z = 12$ and 74. It can be seen that a number of small species with molar masses between 12 and 18, which represent C_1^+ species (C^+ , CH^+ , CH_2^+ , CH_3^+ , CH_4^+) and H_2O^+ and fragments, are present. The peak corresponding to H_2O^+ is very small and it probably appears due to the impurities. Moreover, the peaks at molar masses of 25, 26, 27 and 28 represent C_2 species that are C_2H^+ , $C_2H_2^+$, $C_2H_3^+$ and $C_2H_4^+$, respectively. The strongest peak was observed at $m/z = 28$ (see the insert in Figure 5.16). It must be noted that Si atoms and CO also have a molar mass of 28, which is also shared by C_2H_4 . However, the probability of the appearance of CO as a product from decomposition of HMDSO is impossible in the pyrolysis case. The Si-containing species that appeared or increased in the post shock measurement can be seen at $m/z = 43, 45, 59$ and 73, representing $SiCH_3^+$, $SiOH^+$, $OSi(CH_3)^+$ and $Si(CH_3)_3^+$ or HSi_2O , respectively.

It seems that methyl groups appear in the early stages of HMDSO decomposition and form a wide range of C_2^+ species. In the absence of mechanism for the pyrolysis of HMDSO and for rough understanding, the reaction of CH_3 fragments from HMDSO molecules can be simulated with CHEMKIN as software tool and using the GRI 3.0 mechanism [130], assuming that all CH_3 is cleaved from the HMDSO molecules. Therefore, in this simulation the ligands were considered (1 mol HMDSO producing 6 mol CH_3). The simulation was carried out under similar conditions of $T_5 = 1654$ K and $p_5 = 1.39$ bar with 3% CH_3 instead of 0.5% HMDSO. In Figure 5.18 CH_4 , C_2H_2 , C_2H_4 and C_2H_6 are readily observed due to their high concentration compared to other C species. Figure 5.18 shows that ethane plays an intermediate role here. It appears very early and the profile reaches a maximum very quickly before decreasing again. This implies a fast reaction of CH_3 forming mainly C_2H_2 , C_2H_4 and CH_4 as a result. The simulation also shows that acetylene (as end product) reaches the highest concentration, whereas the TOF-MS results show the intensity signal at $m/z = 28$ is always higher than the signal at $m/z = 26$.

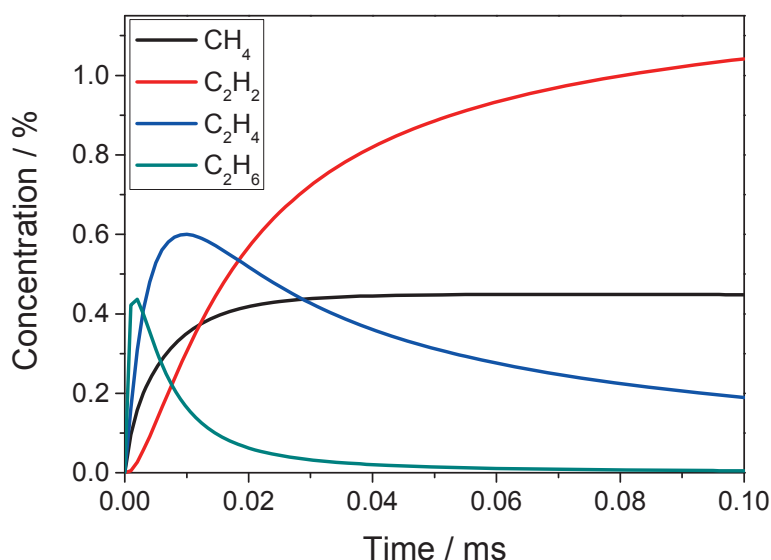


Figure 5.18: CHEMKIN simulation of the C species that yield from the reaction of 3% CH_3 diluted mixed with 1% Ar and diluted in Ne at $T_5 = 1650$ K and $p_5 = 1.39$ bar

Acetylene has been already calibrated for the facility by Aghsaei et al. [131]. The calibration factor can be used here to link the intensity-time profile of acetylene with absolute concentrations. Figure 5.19 shows the concentration-time profiles of HMDSO and acetylene. It can be seen in the Figure 5.19 that acetylene starts to increase with an induction time of 100 μs and reaches 0.35% after 1.5 ms. The rate of acetylene formation in Figure 5.19 cannot be compared with the previous simulation in Figure 5.18, because the simulation was artificially started with the CH_3^+ and therefore was very fast compared to the experimental results. It

also can be seen in Figure 5.19 that the maximum concentration of acetylene at 1.5 ms is about 0.4%, which is much lower than the simulation in Figure 5.18.

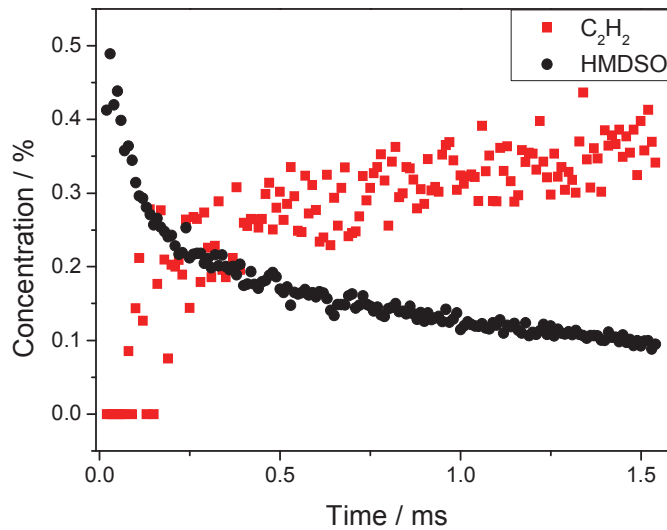


Figure 5.19: Concentration-time profiles of HMDSO and acetylene. 0.5% HMDSO and 1% Ar diluted in Ne at $T_5 = 1650$ K and $p_5 = 1.39$ bar

It is also not clear if Si^+ appears at $m/z = 28$. Therefore, investigation of the free Si atoms from the decomposition of HMDSO was carried out in the shock tube experiments using Atomic Resonance Absorption Spectroscopy (ARAS).

5.1.2.2. Atomic Resonance Absorption Spectroscopy (ARAS) of silicon atoms

This technique was applied at the shock tube to determine the qualitative as well as quantitative concentration details of free Si atoms from the decomposition of HMDSO molecules behind the reflected shock wave. The highly diluted initial mixture which contained 1 ppm HMDSO in Ar shows the high sensitivity of the technique. Moreover, the very low HMDSO concentration also minimizes the influence of subsequent reactions. An example of a typical time-resolved ARAS-signal of Si atoms is shown in Figure 5.20. It can be seen that the ARAS signal immediately increases behind the reflected shock wave, exhibiting an absorption of about 40%, and then decreases again but only down to a certain equilibrium plateau (30% of the initial maximum absorption). A possible reason for the equilibrium plateau is that the hydrocarbon species that are produced from the HMDSO decomposition absorb a portion of the emitted light at 251.6 nm.

The peak in the signal or the amount of absorbed light can be used to determine the quantitative concentration of Si atoms as a function of temperature. The calibration curve from Mick et al. [132] for Si atoms from silane was used to calibrate the Si atom concentration

from the decomposition of HMDSO. The ARAS experiments for the investigation of Si atoms from the decomposition of HMDSO were carried out at temperatures between 1350 and 1993 K. The results in Figure 5.21 show an almost linear increase in the Si concentration with rising temperature. Below 1350 K no ARAS signal could be detected for Si atoms. This means that the TOF-signals at $m/z = 28$ of the HMDSO decomposition at high temperature (higher than 1350K) is an overlap of ethylene and a small portion of free Si atoms.

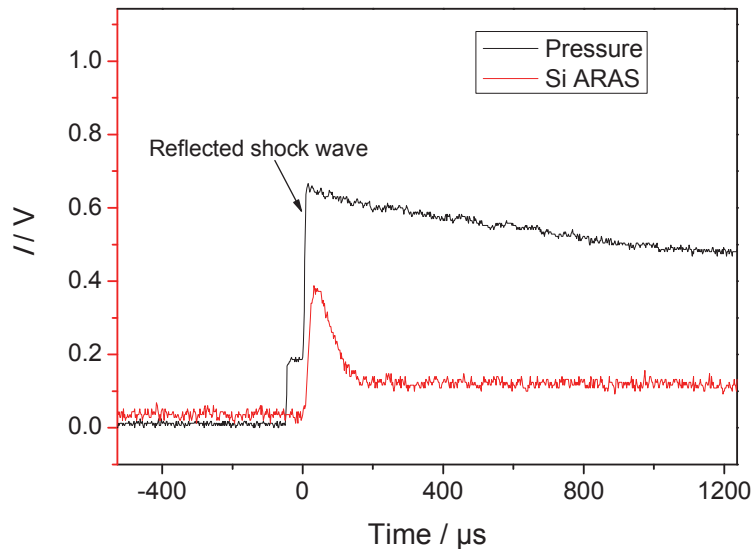


Figure 5.20: Raw ARAS data of Si atoms that produced from HMDSO pyrolysis. (1 ppm HMDSO in Ar, $p_5 = 1.51$ bar, $T_5 = 1674$ K)

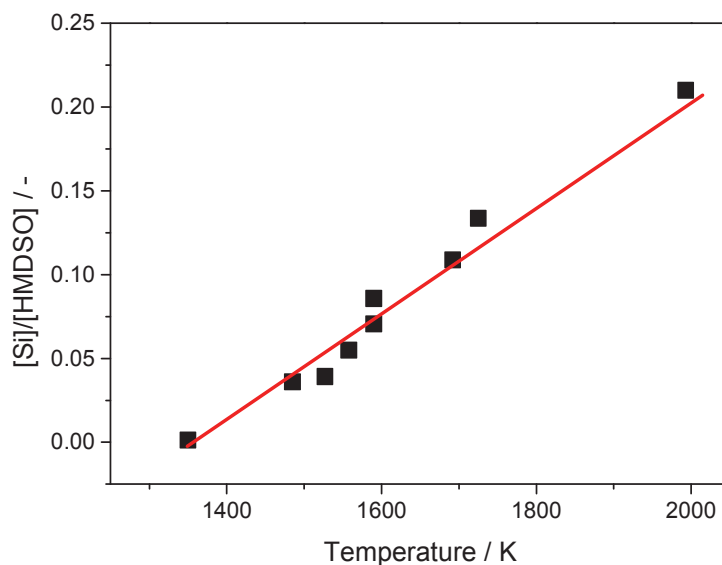


Figure 5.21: $[Si]/[HMDSO]$ peak ratio as a function of temperature. (1 ppm HMDSO in Argon, $p_5 = 1.5$ bar)

5.1.2.3. The influence of oxygen on the initial gas mixture

To study HMDSO in an oxidative environment small amounts of oxygen, here between 1 and 4%, were added to the initial gas mixture. This range of oxygen concentration is not sufficient for complete oxidation of the HMDSO. The purpose was to observe the change in the kinetics by adding increasing concentrations of oxygen in the sub-stoichiometric region of HMDSO combustion.

Figure 5.22 shows an averaged TOF mass spectrum (10 mass spectra after 1.0 ms of the shock arrival) of the HMDSO oxidation behind the reflected shock wave with an initial gas mixture of 0.5% HMDSO, 0.5% Ar and 4% O₂ diluted in Ne. In this mass spectrum two new peaks appear beside those of oxygen ($m/z = 16$ and 32) at $m/z = 17$ and 44 , which represent OH⁺ and CO₂⁺ and/or SiO⁺, respectively. At the peak of $m/z = 28$ CO⁺ and C₂H₄⁺ are expected and the probability of appearance of Si⁺ at $m/z = 28$ from an initial gas mixture that contains oxygen is very low. The reaction of Si with O₂ is very fast and its reaction rate is close to the collision rate as stated in Mick et al. [132]. However, ethylene as an intermediate product will disappear after a short time due to combustion and the CO concentration will increase.

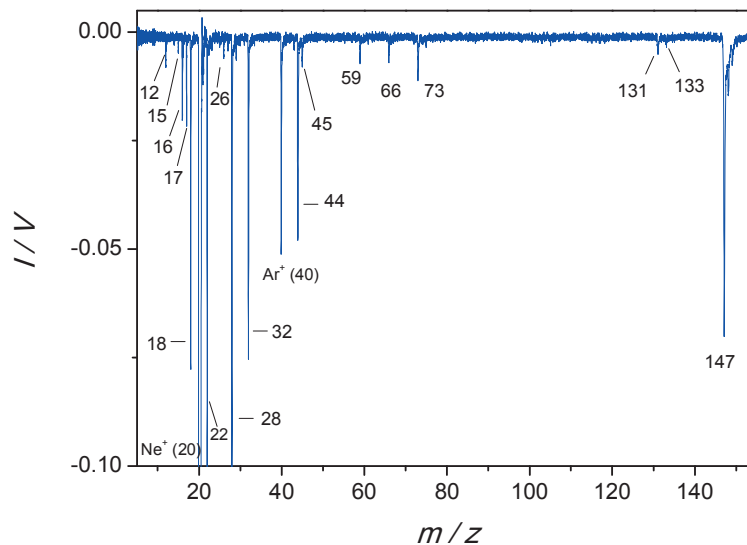


Figure 5.22: Mass spectrum for 0.5% HMDSO + 0.5% Ar + 4% O₂ in Ne; $T_5 = 1573$ K, $p_5 = 1.38$ bar

Figure 5.23 shows a comparison between the decay of HMDSO in the initial gas mixture with 4% oxygen and without oxygen. One can see that as expected the presence of oxygen accelerates the conversion of HMDSO, although T_5 of the experiment without oxygen is higher by about 80 K than that in the test with oxygen.

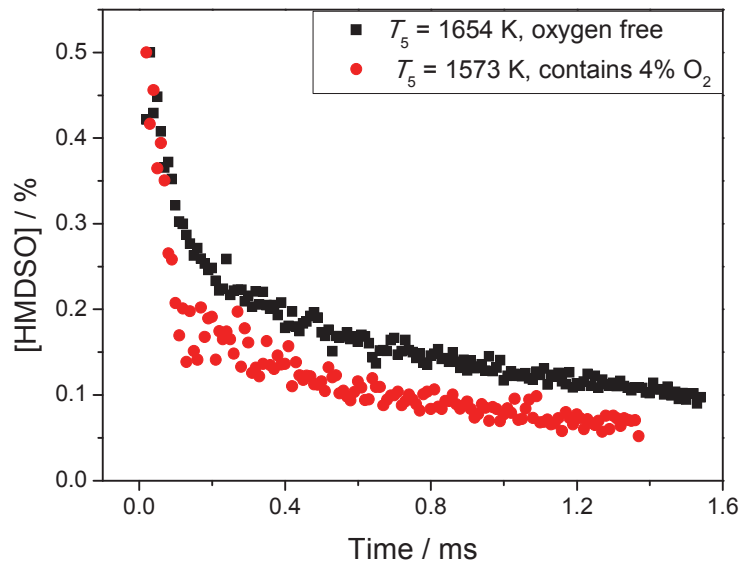


Figure 5.23: Comparison of HMDSO decay curves in oxygen-free and oxygen-containing gas mixtures (4% oxygen)

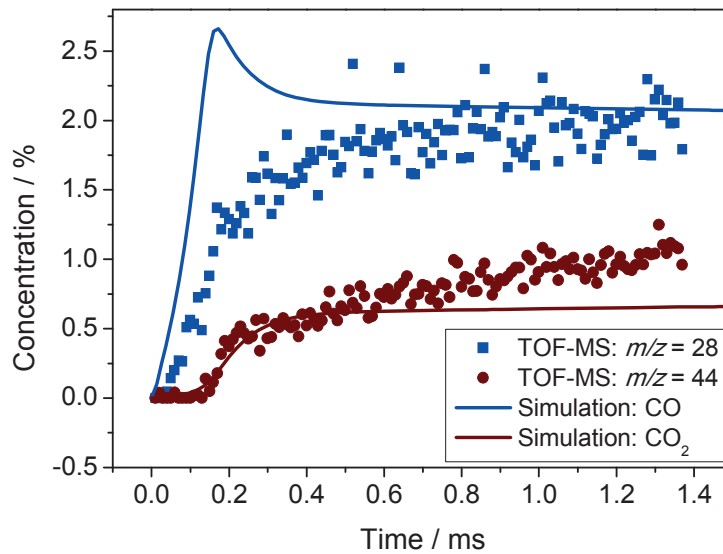


Figure 5.24: Comparison of concentration-time profiles between simulated CO and CO₂ and TOF-MS-signals of $m/z = 28$ and 44 . $T_5 = 1573$ K, $p_5 = 1.38$ bar

Figure 5.24 shows the concentration-time profiles of $m/z = 28$ and 44 , which are expected to represent CO and CO₂ and/or SiO, respectively. It can be seen that the formation of CO starts immediately behind the reflected shock wave, whereas the rise in $m/z = 44$ begins after an induction time of 160 μ s. Burkert et al. [46] detected SiO* emission in a substoichiometric HMDSO/propane/air flame up to 40 mm height above burner. Based on this work it is as-

sumed that the profile of $m/z = 44$ represents a non-negligible number of SiO species besides CO₂. Additionally, concentration-time profiles of CO and CO₂ from the combustion of 3% CH₃ with 4% O₂ diluted in Ne were simulated in CHEMKIN under the same conditions of the experiment. The TOF-signals at $m/z = 28$ and 44 were linked to absolute concentrations by normalizing all measured points to the final simulated CO concentration. To match the experiment and the simulation in time, the simulated profiles were stretched by a factor 10 on the time axis. The simulation shows that the formation of CO₂ also increases with an induction time. However, the maximum concentration is reached quickly and remains constant whereas the TOF-MS-signals at $m/z = 44$ continue to increase.

5.1.2.4. Ignition delay times of HMDSO

The ignition delay times of HMDSO were also evaluated by OH* emission detection behind the reflected shock wave, as it was done for TEOS in section 5.1.1.2. The measurements of ignition delay times as a function of temperature were carried out in shock tube 2, as mentioned in section 4.3.2. Additionally, the influence of moisture as well as pressure on the ignition delay times was measured for three conditions (cf. Table 5.2).

Table 5.2: Conditions of the shock-tube experiments with HMDSO in synthetic air

Mixture	Concentrations		p_5 / bar
	HMDSO / ppm	H ₂ O / vol. %	
1	1800	0	1.7
2	1800	8	1.7
3	1800	0	2.8

The results of ignition delay times of HMDSO under the mentioned conditions in Table 5.2 were depicted as a function of temperature in an Arrhenius diagram. Figure 5.25 shows that the presence of moisture in the initial gas mixture as well as increasing pressure behind the reflected shock wave p_5 , up to 2.8 bar, has no influence on the ignition delay time of HMDSO.

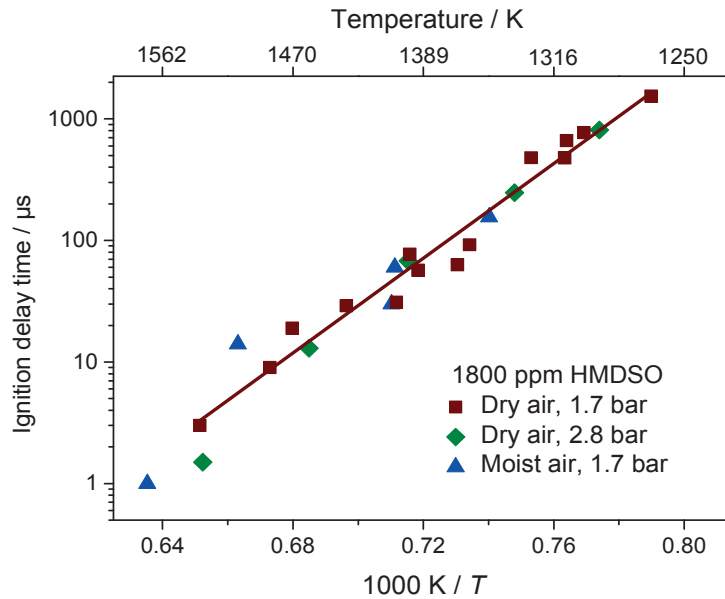


Figure 5.25: Ignition delay times of HMDSO under various conditions

The temperature-dependent ignition-delay time of HMDSO in synthetic air, for conditions 1, 2 and 3 in Table 4.2 can be given by the following expression:

$$\tau = 1.186 \times 10^{-11} \exp(41200 \text{ K}/T) \mu\text{s} \quad (5.4)$$

5.1.2.5. Simultaneous measurements of OH* chemiluminescence and TOF-MS

The aim of these experiments was to obtain better understanding of the interference between the combustion of the ligands and the kinetics of the precursor. The heat release could significantly affect the precursor depletion. For this purpose, during the ignition of HMDSO behind the reflected shock wave, the OH* emission signal was detected simultaneously using TOF-MS measurements. The initial gas mixture contained 0.5% HMDSO, 4% oxygen and 0.5% Ar diluted in Ne. Figure 5.27 shows the OH* chemiluminescence and HMDSO decay at $m/z = 147$ with the same time history behind the reflected shock wave. It can be seen that OH* chemiluminescence appears after the depletion of about 50% of HMDSO. It should be noted that this ignition delay time of HMDSO in Figure 5.26 is not comparable with the previous measurements that are presented in Figure 5.25 due to the difference in the gas composition.

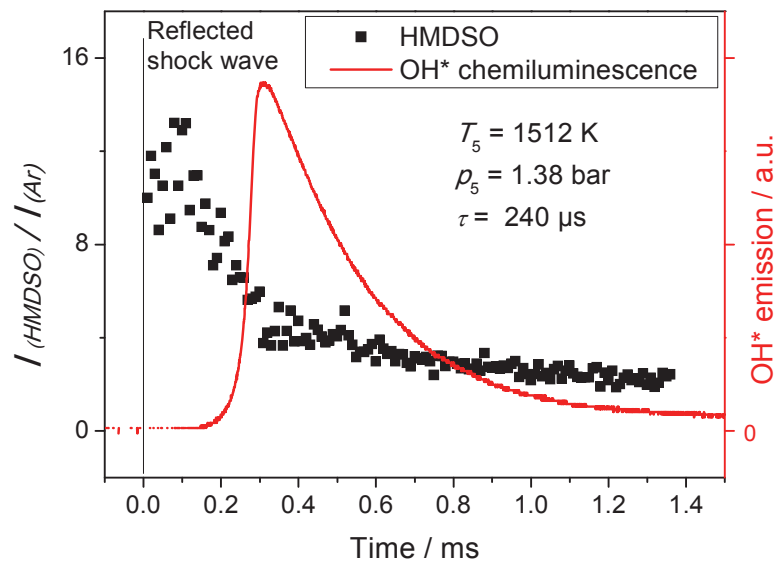


Figure 5.26: Ignition delay times during the decay of HMDSO from simultaneous measurement of OH* chemiluminescence and TOF-MS measurement of the HMDSO concentration

Figure 5.27 shows the simultaneous measurement of OH* emission and the profiles of TOF-MS at $m/z = 28$ and 44 , which represent CO and CO₂ and/or SiO respectively. It can be seen that CO formation starts together with a step increase in OH* emission and the beginning of CO₂ and/or SiO formation is located at the point of maximum OH* emission on the time axis.

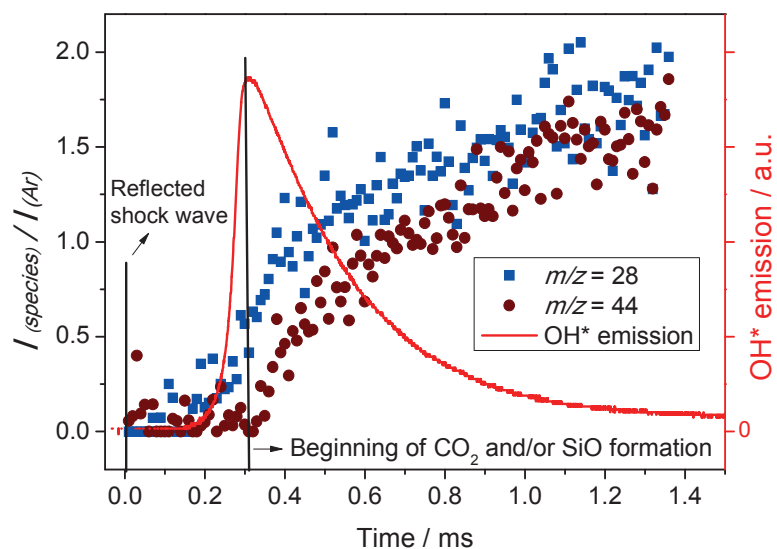


Figure 5.27: Simultaneous measurement of OH* chemiluminescence and TOF-MS showing the signals at $m/z = 28$ and 44 . $T_5 = 1512$ K

It can be concluded from the results of the shock-tube experiments that several monomers are produced from the decomposition of HMDSO. They are mainly Si atoms, SiO and Si-O-Si. They can be found as free atoms and molecules or are joined with one or more H atoms and/or methyl groups. The concentration of each species depends strongly on the temperature. Adding a small amount of oxygen into the initial gas mixture, which is not sufficient for complete combustion of HMDSO, increases the concentration of CO₂ and/or SiO dramatically. These different monomers, from HMDSO decomposition, may have a strong influence on the particle size and particle size distribution due to the different mechanisms for the formation and growth of silica particles. This agrees with the study of Briesen et al. [55].

5.2. Microwave plasma reactor

5.2.1. Temperature imaging in the microwave-plasma reactor using multiline NO-LIF thermometry

5.2.1.1. Investigating the influence of the main parameters on the plasma temperature

The objective of these measurements was to understand the influence of the main parameters such as microwave-power and reactor pressure on the plasma temperature. Especially since the gas-phase chemistry is mainly governed by gas temperature. The experimental conditions as well as the parameter variation range were chosen for the subsequently planned experiments of the synthesis of silica nanoparticles from TEOS in the microwave-plasma reactor. However, a certain amount of NO was added into the initial gas mixture that is required for the multiline NO-LIF thermometry in the microwave-plasma reactor. From all experiments the temperature in the center of the quartz tube was used for the following discussion of this comparison. The experimental parameters for the NO-LIF temperature measurements in the microwave-plasma reactor are presented in Table 5.3.

Table 5.3: Experimental conditions for the NO-LIF temperature measurements in the microwave-plasma reactor

Parameter	Variation range	Unit
O ₂ mass flow rate	1.0	slm
Ar mass flow rate	2.1	slm
Ar/O ₂ ratio	1.5–14.5	-
NO concentration	1000–4000	ppm
Reactor pressure	30	mbar
Microwave power	100–500	W

Due to the required presence of NO molecules in the initial gas mixture for the multiline NO-LIF temperature measurement, the influence of NO on the plasma temperature was investigated first. Therefore, the plasma temperature was measured using three different NO concentrations of 1000, 2600 and 4000 ppm in the initial gas mixture. Figure 5.28 shows that the temperature with 4000 ppm NO after the microwave antenna is around 700 K and remains almost constant up to 38 mm downstream of the microwave antenna (cf. Figure 4.24). Decreasing the NO concentration from 4000 to 1000 ppm causes the temperature to decrease by about 100 K. This means that adding NO into the initial gas mixture leads to an increase in temperature.

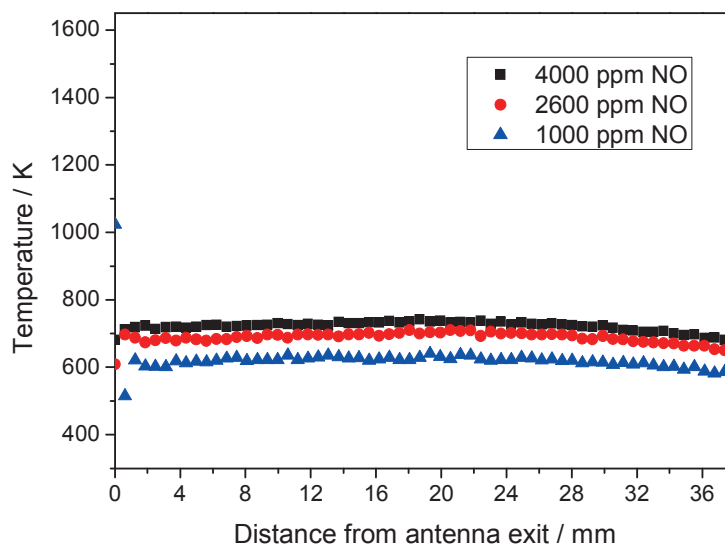


Figure 5.28: Influence of the NO concentration on the plasma temperature. $P_{MW} = 200$ W, $p = 40$ mbar

The microwave power was varied between 100 and 500 W with a constant NO concentration of 4000 ppm. The results are plotted in Figure 5.29 and show that the microwave power has a strong influence on the plasma temperature. Figure 5.29b shows that the plasma temperature increases almost linearly with increasing microwave power. Increasing the microwave power leads to a higher number of energetic electrons which collide elastically with heavy neutral particles, thus leading to a higher gas temperature. During the experiment it was also observed that increasing the microwave power leads to an increase in the plasma length.

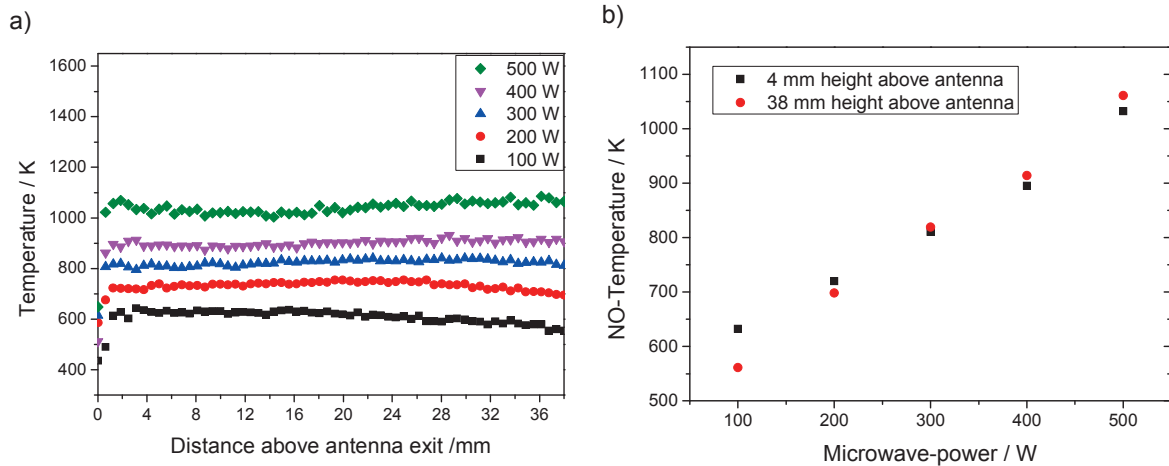


Figure 5.29: Influence of the microwave power on the plasma temperature ($p = 40$ mbar, $[\text{NO}] = 4000$ ppm)

Two dimensional CFD-simulation of the plasma reactor has been carried out by Matheis [133] at Technical University of Munich. The simulated velocity and temperature distribution as well as the particle formation and growth under similar conditions were obtained. Figure 5.30a shows a top view of the 2D-temperature distribution in the plasma reactor. The figure shows a strong radial temperature gradient inside the antenna. This is because of the high speed of the cold inlet gas from the small nozzle opening. On the other hand the temperature distribution outside the antenna is more homogenized. Figure 5.30b shows temperature profiles for variable microwave powers from 150 up to 250 W. The temperature profiles were extracted from the centerline of the reactor, where the highest temperature is outside the antenna. The figure shows that the temperature range of the simulation is much higher than the experimental results. The temperature profile of $P_{MW} = 200$ W shows a temperature of about 2200 K at the antenna exit and about 1500 K at 38 mm downstream from the antenna exit.

The linear increase in temperature as shown in Figure 5.29b illustrates that at the given conditions microwave radiation can deposit additional energy in the gas within the investigated power range. In contrast, when varying the reactor pressure with a fixed gas composition and a microwave power at 200 W deposited into the gas, the temperature increase saturates for pressures above 60 mbar (cf. Figure 5.31). Below this value, the temperature increases linearly with pressure (cf. Figure 5.31b). An explanation might be that increasing the pressure at a constant mass flow rate by reducing the flow velocity of the gas leads to an increased residence time of the gas inside the antenna. Thus, an increased amount of energy per volume is deposited. However, it appears that around 60 mbar, steady state is to be attained between energy deposition and removal by heat conduction and other loss mechanisms, such that a further increase in residence time does not lead to a significant additional temperature rise. The presence of argon in the gas mixture could also play a role. Conrad et

al [83] demonstrated that the maximum absorption efficiency of argon in a 2.45 GHz discharge is reached at 200 Pa. This also means that to operate the reactor at high pressure, e.g. atmospheric pressure, an increase in the microwave power input is required to ensure sufficient ionization of the plasma gas.

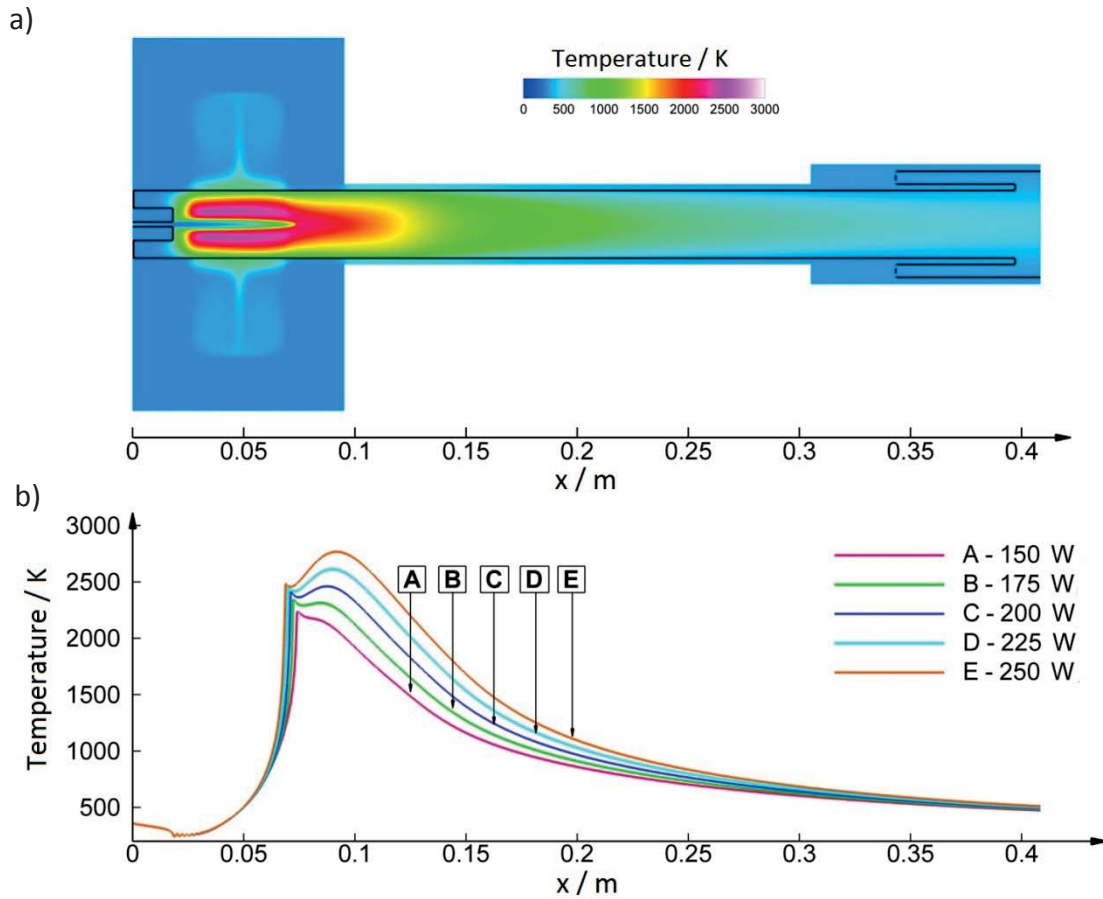


Figure 5.30: a) Top view of the temperature distribution in the microwave-plasma reactor, $P_{MW} = 200$ W, b) Gas temperature profiles from the reactor central line at different microwave powers, $p = 40$ mbar, 1 l/min O_2 and 2.1 l/min Ar [133]

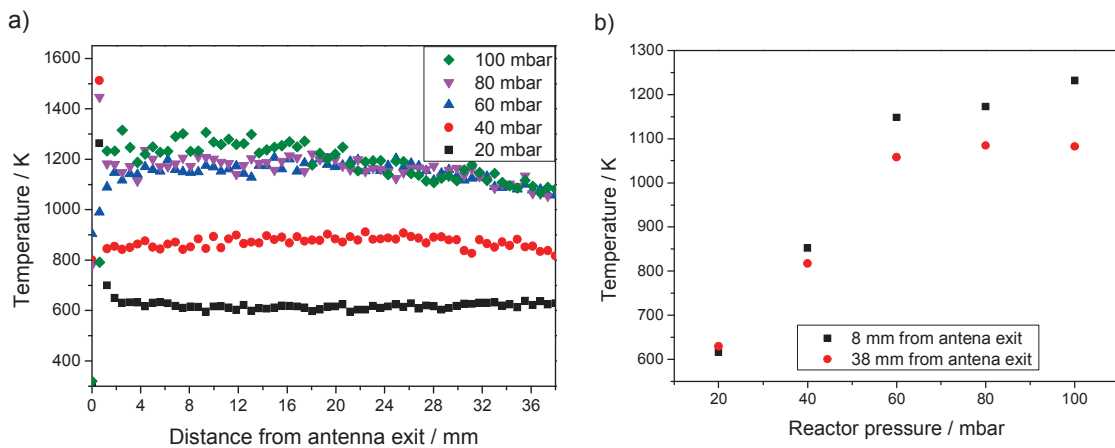


Figure 5.31: Influence of the reactor pressure on the plasma temperature. $P_{MW} = 200$ W, $[NO] = 4000$ ppm

An additional parameter of concern is the Ar/O₂ ratio, which is important for later investigations of its influence on the particle formation. However, as Figure 5.32 shows the change in Ar/O₂ ratio between 1.5 and 14.5 at a constant flow rate of 3.1 slm, has almost no influence on the plasma temperature.

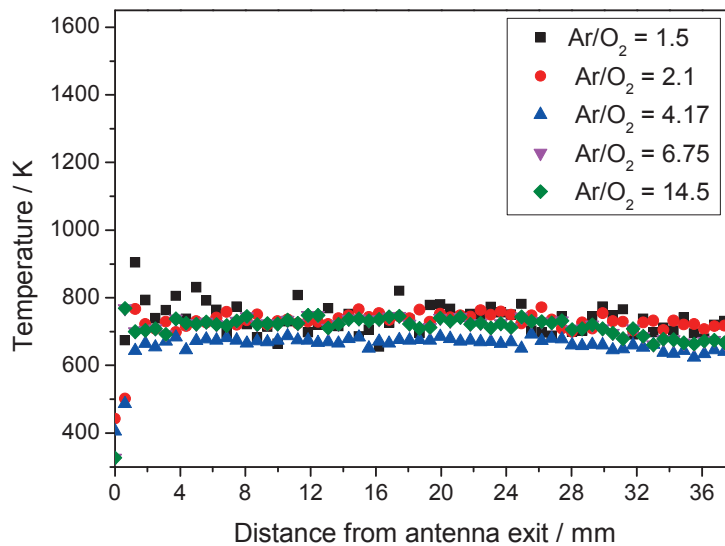


Figure 5.32: Influence of the Ar/O₂ ratio (by volume) on the plasma temperature ($p = 40$ mbar, $P_{MW} = 200$ W, [NO] = 4000 ppm)

5.2.1.2. Investigation of the plasma temperature by injecting TEOS

Following the previous understanding of the plasma behavior, by varying several parameters, the influence of the precursor's presence in the initial gas mixture on the plasma temperature was investigated next. In order to avoid the influence of adding NO into the initial gas mixture on the plasma temperature, NO was produced in-situ in the plasma. It was experimentally established that by supplying gas mixtures that consist of oxygen and nitrogen into the microwave-plasma reactor, NO is formed. Following several tests it was also found that the optimum gas composition for forming enough NO for the multiline NO-LIF measurements is a mixture of 50% oxygen and 50% nitrogen. Thus, the experimental conditions used are presented in Table 5.4.

Figure 5.33 shows the temperature profile of the oxygen/nitrogen gas mixture without precursor in the flow. The plasma temperature at the antenna exit is 1030 K and decreases linearly, with a weak slope, to reach 890 K at 38 mm downstream of the antenna exit. This temperature drop is due to heat transfer to the environment with only little energy deposited at the same time from ion recombination in the after-glow. In contrast, TEOS leads to additional energy release from the combustion of precursor fragments in the oxidizing environment as well as from the heat of condensation of the particles.

Table 5.4: Experimental conditions for the NO-LIF temperature measurements in the microwave-plasma reactor with presence of TEOS

Parameter	Variation range	Unit
TEOS concentration	0, 800, 1600	ppm
Ar mass flow rate	1.5	slm
O ₂ mass flow rate	1.5	slm
Reactor pressure	30	mbar
Microwave Power	200	W

By adding a small amount of TEOS (e.g., 800 ppm) to the same gas mixture and under the same conditions the temperature profile changes [53]. It can be seen in Figure 5.33 that in this case the temperature at the antenna exit is 970 K, about 50 K lower than in the precursor-free case, and it increases to a maximum of 1130 K at 21 mm before decreasing to 950 K at 35 mm downstream of the antenna exit. The overall heat capacity of the gas changes with TEOS addition; this however, would only be responsible for a temperature variation of less than 10 K. From the behavior of the temperature profile it can be understood that TEOS decomposes almost completely in the microwave antenna and just after the antenna exit combustion of the decomposition species such as ethylene and ethanol begin, causing the temperature to increase. The combustion of ethylene and ethanol adds approximately 2594 kJ/mol to the gas, which would lead to an increase in the adiabatic flame temperature of approximately 125 K [53]. This number is in reasonable agreement with the observed temperature rise in Figure 5.33.

By increasing the TEOS concentration up to 1600 ppm the temperature profile shifts by about 100 K higher for the 800 ppm case. However, the shape of the profile and location of the maximum temperature remains almost the same. For both temperature profiles with precursor a sharp temperature drop at about 25 mm downstream of the antenna exit can be observed, indicating the end of the reaction zone. It should be noted that in the presence of TEOS the deposition of particles to the reactor walls lead to a reduction in detected signal. While this does not affect the temperature measurement in principle (signal intensity cancels out in data reduction) the loss in signal leads to a reduced signal-to-noise ratio as seen in Figure 5.33.

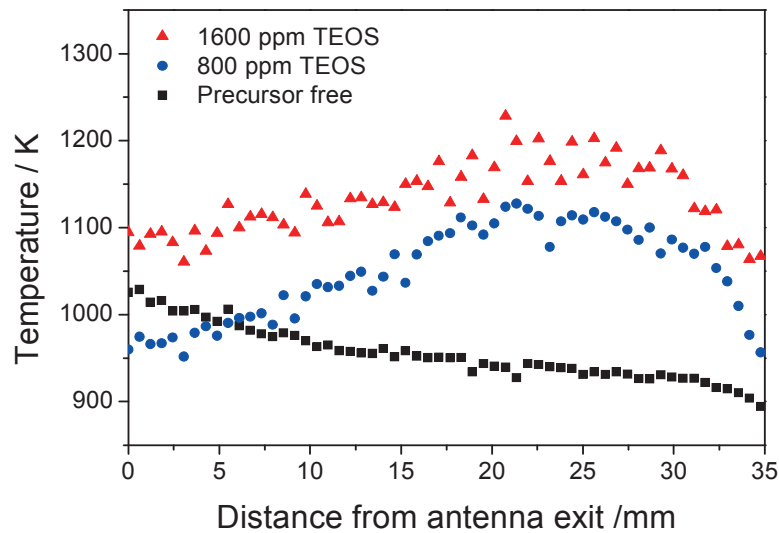


Figure 5.33: Temperature profiles of the plasma as a function of distance from antenna exit with and without precursor. $P_{MW} = 200$ W, $p = 35$ mbar N_2 : 1.5 slm and O_2 : 1.5 slm

Converting the distance from the antenna exit into time can provide data for kinetic studies and may help in understanding the chemistry in the plasma. Figure 5.34 shows the temperature profiles with 800 and 1600 ppm cases as a function of time. The residence time inside the microwave antenna was also taken into account. This was estimated with means of CFD simulations under similar conditions. The residence time inside the microwave antenna was then extracted from the centerline CFD data. The residence time outside the microwave antenna was calculated depending on the measured temperature. Figure 5.34 shows that TEOS has been already decomposed inside the antenna. The combustion of the decomposition products, mainly ethylene and ethanol, begins just beyond the antenna exit causing an increase in temperature. Inserting the temperature at the antenna exit, with value of 1080 K, of the plasma with 1600 ppm into the equation of TEOS ignition delay times in dry mixture (eq. 5.3) gives an ignition delay time of 2.23 ms. This ignition delay time (2.23 ms) is located on the time axis close to the maximum of the temperature profile of the 1600 ppm case (Figure 5.34). In contrast, the ignition delay time of TEOS at 970 K (800 ppm) is about 46 ms, which is far from the time scale of the measurement. This is due to the higher temperature in the microwave antenna which could not be measured with this experimental setup. This also indicates that the temperature drops sharply in the region of the cooled antenna wall (cf. Figure 4.5).

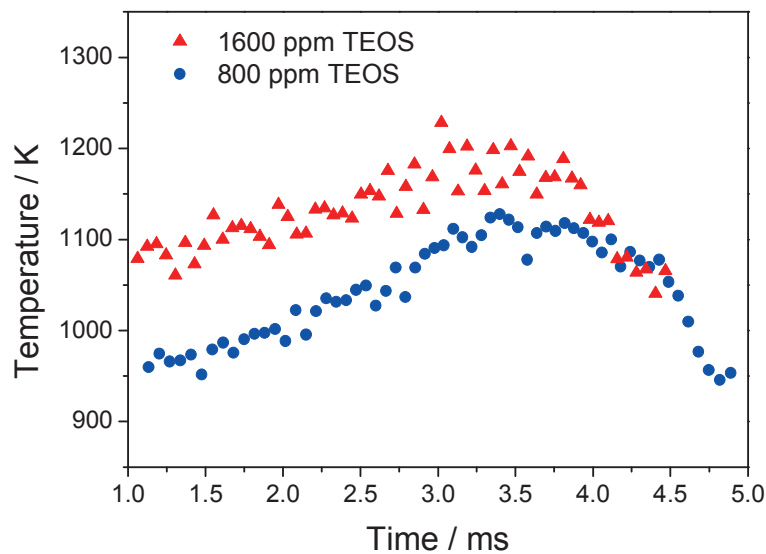


Figure 5.34: Temperature vs. time for plasma with 800 and 1600 ppm TEOS. $P_{MW} = 200$ W, $p = 35$ mbar N_2 : 1.5 slm and O_2 : 1.5 slm

5.2.1.3. Investigation of particle formation in the microwave-plasma hot-wall reactor

Silica nanoparticles were successfully synthesized from TEOS in the microwave-plasma reactor. The growth of the particles was systematically investigated by changing various parameters, which are expected to influence the particle size as well as the particle morphology. The process parameters, the variation range and the standard conditions are presented in Table 5.5.

Table 5.5: Process parameters for SiO_2 -nanoparticle synthesis in the microwave-plasma hot-wall reactor

	Parameter	Variation range	Standard condition	Unit
Experiments without furnace	TEOS concentration	580–7470	1730	ppm
	Mass flow rate Ar	2.1–2.9	2.1	slm
	Mass flow rate O_2	0.2–1.0	1.0	slm
	Ar/ O_2 ratio	2.1–14.5	2.1	-
Exp. with furnace	Microwave power	150–450	200	W
	Furnace temperature	200–1000	800	$^{\circ}C$
	Reactor pressure	40–70	40	mbar

The influence of TEOS concentration on the particle size was investigated by varying the TEOS flow rate from 1 to 13 g/h (equivalent to 580 to 7470 ppm) while keeping the flow rate of argon and oxygen constant, at 2.1 slm and 1.0 slm respectively. The mass flow rate of oxygen, of 1.0 slm, ensures the complete oxidation of all TEOS decomposition products during the variation of TEOS concentration (equivalence ratio range $\phi = 0.02 - 0.28$). For these tests, the plasma reactor was used without the hot-wall furnace in order to observe the direct influence of TEOS concentration on the resulting particle size. A representative TEM image of silica nanoparticles obtained by thermophoretic sampling from the reactor chamber is shown in Figure 5.35. In all cases the particles were non-agglomerated and had an almost spherical morphology.

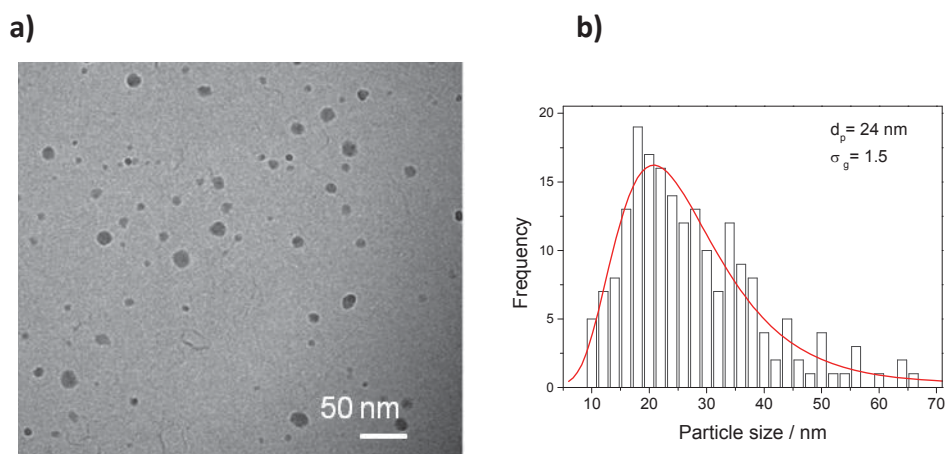


Figure 5.35: a) TEM-image of silica nanoparticles sampled from the reactor chamber. TEOS concentration is 6000 ppm, reactor pressure is 40 mbar; b) histogram and fitted log-normal size distribution with a mean particle diameter $d_p = 24 \text{ nm}$ and geometric standard deviation $\sigma = 1.5$

Figure 5.36 shows the dependence of the mean particle diameter on the TEOS concentration. Up to TEOS concentrations of 4040 ppm the particle size increases as expected from 12 nm (at 580 ppm TEOS) to about 28 nm (at 4040 ppm TEOS). This progressive increase in the particle size with rising precursor concentration results from higher frequency of collisions, coagulation and coalescence, that are due to an elevated monomer concentration. However, the particle size decreases slightly with a further increase in TEOS concentration. A likely explanation for this is the increase in temperature of the gas with increasing TEOS concentration as mentioned in section 5.2.1.2 (cf. Figure 5.33). This will speed up the gas flow in the antenna region and decrease the residence time at high temperatures, which results in a smaller particle size. Another explanation could be that at higher TEOS concentrations the nucleation rate is increased, thus, resulting in a higher concentration of primary particles with slightly smaller sizes. This behaviour is well known and described as collision-limited growth of particles [66].

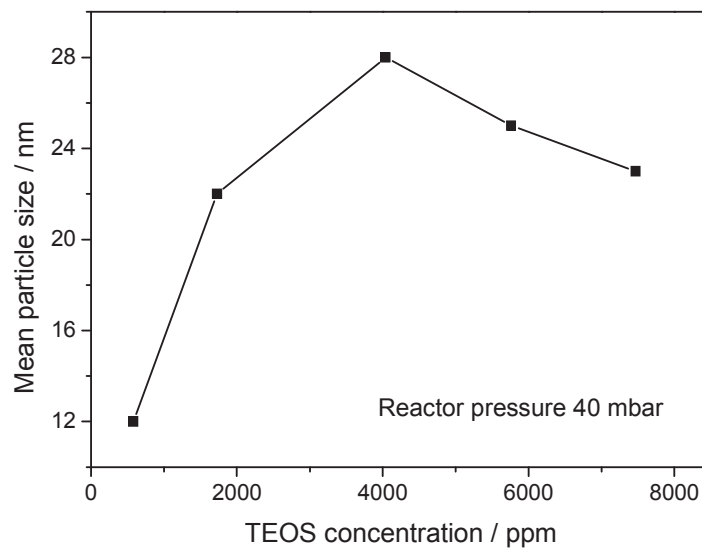


Figure 5.36: Influence of TEOS concentration on the mean particle size. $P_{MW} = 200 \text{ W}$, $p = 40 \text{ mbar}$

The microwave power was varied between 150 and 450 W. However, its influence on the particle size is not clear, as shown in Figure 5.37. The particle size increases slightly at 300 W and then decreases again. This can be explained by two antagonistic influences. With increasing microwave power the plasma temperature increases significantly as shown in Figure 5.29, which in turn should result in larger particles due to the faster dissociation rate of TEOS and higher collision rates of the monomers, clusters and particles. On the other hand several factors can lead to smaller particle size with increasing microwave power. The higher temperature decreases the residence time due to the reduced density at constant length, pressure and mass flow rates. Moreover, the defragmentation rate of clusters increases at higher temperatures. It was also observed during the experiments that the plasma volume increased with rising microwave power. In this case the thermodynamic equilibrium of clusters may take longer to be achieved, leaving less time for particle growth. High microwave power can also lead to increased charging of both the gaseous species and the particles and, thereby, the repulsive forces between the primary particles are increased and their collisional growth is thus reduced [134].

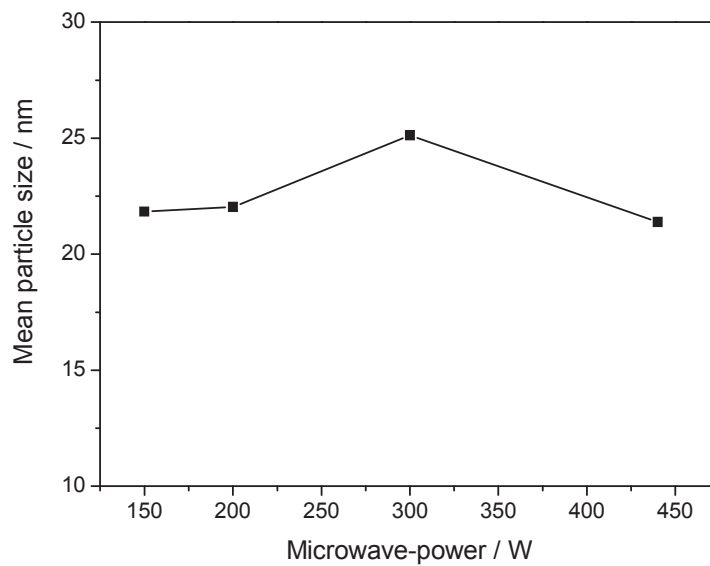


Figure 5.37: Influence of the microwave power on the particle size ([TEOS] = 1730 ppm, $p = 30$ mbar)

Increasing the Ar/O₂ ratio from 2.1 to 14.5, as illustrated in Figure 5.38, shows almost no influence on the particle size. This can be explained by the constant plasma temperature with variation of the Ar/O₂ ratio as discussed in subchapter 5.2.1.1 (cf. Figure 5.32). However, the presence of TEOS in the initial gas mixture influences the plasma temperature. Moreover, the amount of oxygen at an Ar/O₂ ratio of 14.5 (equivalence ratio $\phi = 0.3$) is high enough to oxidize all the species formed from the decomposition of TEOS to produce CO₂ and H₂O in addition to SiO₂. Therefore, this variation is expected to have no influence on the combustion process of TEOS.

For the following experiments the hot-wall furnace was mounted downstream of the plasma reactor (cf. Figure 4.6) to investigate the influence of the temperature history on the mean particle size. For these experiments, the TEOS concentration was 1730 ppm, the reactor pressure was 40 mbar and the microwave power was 200 W. The same condition was also investigated without the furnace (cf. Figure 5.36). To observe the influence of the furnace on the mean particle size, the hot-wall temperature was varied between 200 and 1000°C. The results are given in Figure 5.39, except for the data point at 1000°C as at this high furnace temperature the TEM grids were getting damaged.

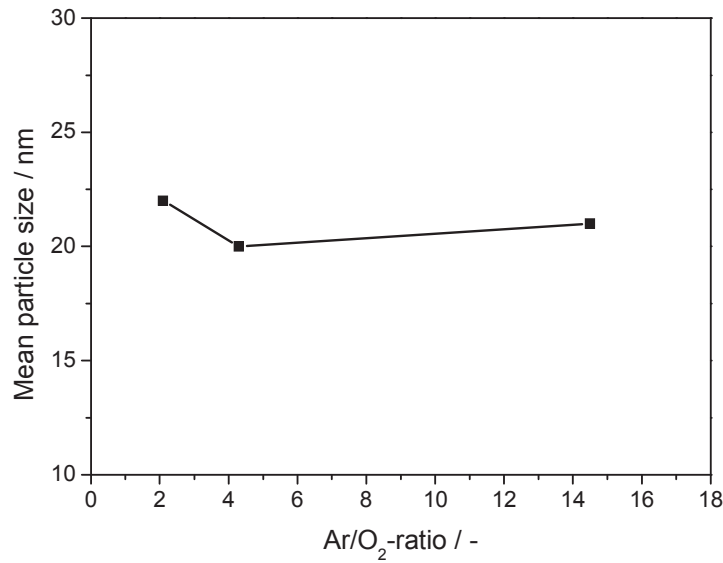


Figure 5.38: Influence of Ar/O₂ ratio on the mean particle size. [TEOS] = 1730 ppm $P_{MW} = 200$ W, $p = 30$ mbar

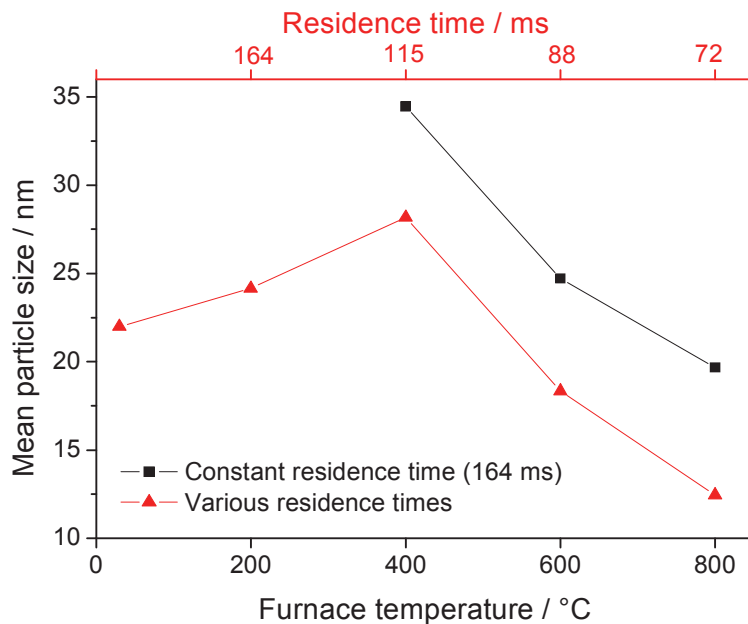


Figure 5.39: Influence of the furnace temperature on the particle size. Various residence times at constant pressure (\blacktriangle); constant residence time at various pressures (\blacksquare). [TEOS] = 1730 ppm, $P_{MW} = 200$ W, $p = 40$ mbar

In Figure 5.39 the red profile shows that for furnace temperatures up to 400°C the mean particle size increases as expected due to the rise in frequency of collisions, coagulation and coalescence up to a maximum particle size of 28 nm. However, the particle size decreases when the furnace temperature exceeds 400°C. This is attributed to two factors: firstly as

expected from plasma synthesis of nanoparticles, Coulomb repulsion plays an important role in preventing agglomeration. Therefore, at high furnace temperatures the particles are likely to gain a higher charge due to thermionization, thus, hindering particle collisions and growth [135]. The influence of the hot-wall temperature on the particle charge due to thermionization, and its influence of preventing the particle growth has been investigated by Schiel et al. [57] and Reuter et al. [58]. Secondly, the residence time decreases with increasing furnace temperature because of the reduced density at fixed pressure and gas flow rate. The influence of decreasing residence times on the particle size at high temperatures was investigated. For different temperatures the reactor pressure was varied in order to keep the residence time fixed at 164 ms, assuming that the temperature is static along the furnace axis. The results of these tests are shown in Figure 5.39 (black profile). It can also be seen in Figure 5.39 that the particle sizes at constant residence time of 164 ms are also larger at lower temperature and decreases with increasing furnace temperature mainly due to the Coulomb repulsion effect.

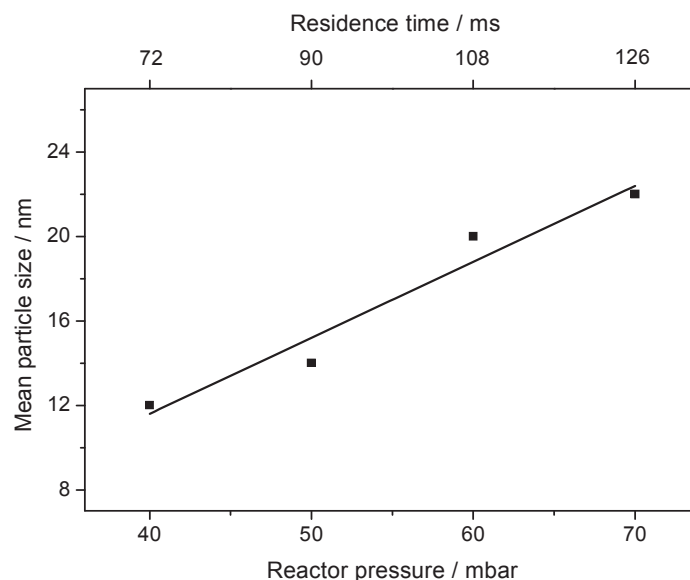


Figure 5.40: Influence of reactor pressure on the particle size. $T_{Furnace} = 800^{\circ}\text{C}$, $[\text{TEOS}] = 1730 \text{ ppm}$, $P_{MW} = 200 \text{ W}$,

To investigate whether the residence time within the reactor influences the particle growth, the furnace temperature was kept at 800°C while the residence time was varied from 72 to 126 ms by increasing the reactor pressure from 40 to 70 mbar. As it can be seen from Figure 5.40, the mean particle diameter depends strongly and almost linearly on the residence time in this case. A rise in the pressure also increases the collision frequencies between the monomers, clusters and particles, which also results in larger particle sizes. These results demonstrate that we were able to adjust the size of silica nanoparticles, prepared by gas-phase synthesis, via tuning the TEOS concentration, furnace temperature and reactor pressure.

In contrast to the samples taken by thermophoretic deposition on TEM grids, all samples collected by the filter or by thermophoretic sampling from the cold walls downstream of the reactor always showed a very high degree of particle agglomeration (cf. Figure 5.41a). The findings discussed above demonstrate that the particles in the gas phase are well separated (as it was shown earlier in Figure 5.35), while hard agglomerates are found in samples taken from the filter and from the cold reactor walls. Nevertheless, the size distribution of the initial silica nanoparticles that form the large aggregates on the filter follows the same log-normal size distribution function as the non-agglomerated particles sampled on TEM grids (cf. Figure 5.41b).

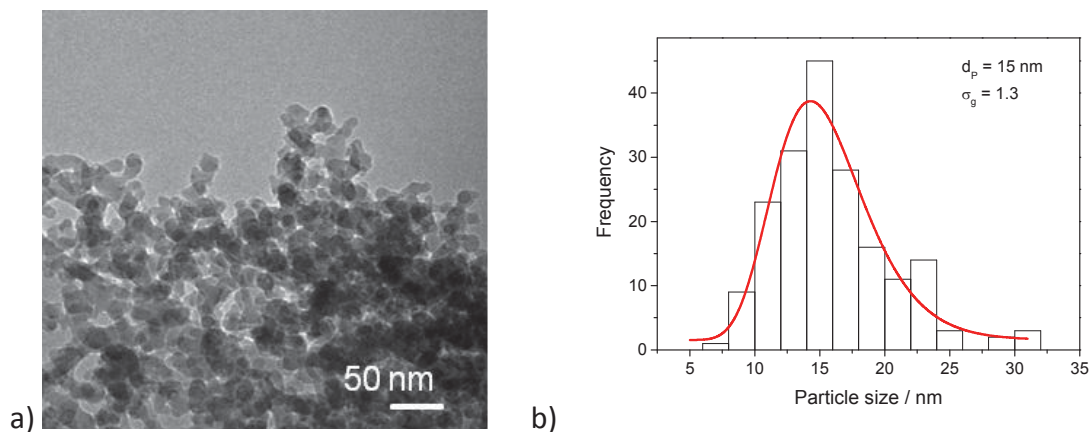


Figure 5.41: TEM-image of the collected particles from the filter (left); histogram and fitted log-normal size distribution (right). [TEOS] = 4040 ppm, $P_{MW} = 200 \text{ W}$, $T_{Furnace} = 1000^\circ\text{C}$, $p = 40 \text{ mbar}$

The calculated BET particle size of the samples from the filter, as shown in Figure 5.41, was 24 nm which is much bigger than that found in the material from the reactor (see Figure 5.41b, mean particle size is 16 nm). The high degree of agglomeration reduces the specific surface area (SSA) and therefore, shows a larger particle size. The aggregation of formerly spherical, non-agglomerated particles may be attributed to the surface chemistry of the freshly prepared silica nanoparticles. Particle adhesion, especially in the nanosized of water in the filter device [136]. Moreover, it is found that materials like inorganic oxides regime, originates from van-der-Waals forces and capillary bridging [137] and creates soft agglomerated silica nanoparticles. The electrostatic (Coulomb) forces, which can prevent particle-particle interaction within the gas phase in the reactor, can be neglected in the filter device because of the discharge due to presence that contain hydroxyl groups on their surface tend to build new, stable chemical bonds by releasing water and thus lead to formation of hard agglomerates [138]. For this reason, a particle sample from the filter was investigated with Fourier Transform Infrared (FTIR) spectroscopy.

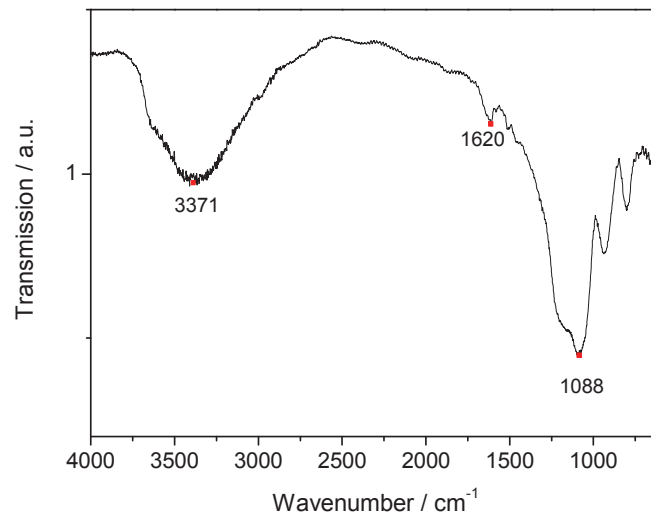


Figure 5.42: FTIR transmission spectrum of SiO₂ nanoparticles sampled from the particle filter

Figure 5.42 shows the FTIR spectrum of silica nanoparticles. In the spectrum, a broad peak around 1088 cm⁻¹ appears which can be assigned to stretching vibration of Si-O-Si. The small peak of the absorption line at 1620 cm⁻¹ is related to the 2TO₂ mode [139, 140]. The FTIR spectrum also shows a strong signal at about 3371 cm⁻¹ indicating a large amount of hydroxyl groups [139] that are expected to be responsible for the highly active particle surface. As a result, it is proposed that silica nanoparticles that touch each other will sinter together due to condensation of the hydroxyl groups on their surface. The high number of hydroxyl groups on the particle surface supports Kraft and co-workers' suggestion that silicic acid is the monomer that is produced from TEOS decomposition.

The particle inception step from silicic acid has been postulated by Kraft and co-workers [38]. It involves the interaction of two silicic acid molecules resulting in the loss of a water molecule and the formation of a dimer. This dimer is considered to be the first particle. This can be represented by a chemical reaction as shown in Figure 5.43. For further particle growth, whether by surface growth or coagulation and coalescence, the surface of the primary particles will contain a high number of hydroxyl groups.

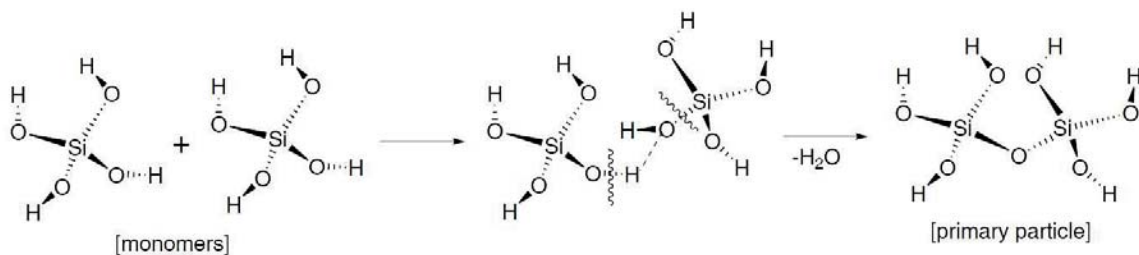


Figure 5.43: Inception of Si-O-Si structure particle from gas-phase monomers [38]

5.3. Low-pressure premixed H₂/O₂/Ar flame reactor

5.3.1. Investigation of silica particle formation in the H₂/O₂/Ar flame reactor using TEOS

The formation of silica nanoparticles from TEOS was successfully investigated in the low-pressure premixed H₂/O₂/Ar flame reactor with means of particle mass spectrometry (PMS). The PMS was used to obtain online information about particle-size distribution of silica nanoparticles during synthesis. The movable burner head at the nozzle orifice of the PMS (cf. Figure 4.8) allows the time history of particle formation to be studied. The influence of the main process parameters such as height above burner (*HAB*), TEOS concentration and equivalence ratio ϕ on the mean particle size were systematically investigated. The range of the parameter variation and the standard condition is presented in Table 5.6.

Table 5.6: Process parameters and standard condition for the silica nanoparticle synthesis in the H₂/O₂/Ar flame reactor

Parameter	Variation range	Standard condition	Unit
Height above burner (<i>HAB</i>)	130–210		mm
TEOS concentration	100–500	400	ppm
Ar mass flow rate	400–600	400	sccm
O ₂ mass flow rate	280–500	480	sccm
H ₂ mass flow rate	300–520	320	sccm
Equivalence ratio ϕ	0.3–0.77	0.3	-
Reactor pressure	30	30	mbar

A typical example of the PMS signal and velocity measurement is shown in Figure 5.44. The maximum current of 0.79 pA was detected at a deflection voltage of 55 V for silica nanoparticles synthesized under the standard conditions and at height above burner (*HAB*) of 150 mm. Using the information from Figure 5.44 and the bulk density of silica material (2.2 g/cm³), the particle size distribution can be determined. The probability density function (*PDF*) parameters were obtained from a log-normal fit of the signal in Figure 5.45. The mean particle size, which is equivalent to the count median diameter (*CMD*), was 9.3 nm with a standard deviation σ_g of 1.18.

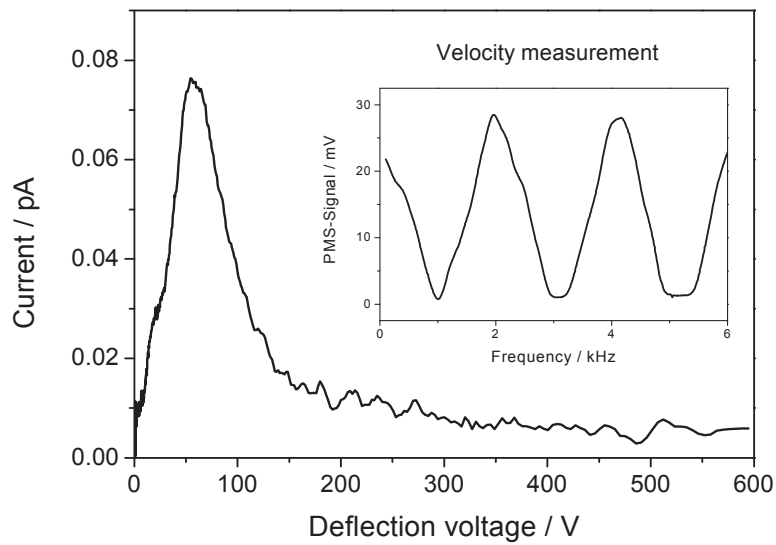


Figure 5.44: Example of PMS current/voltage signal and particle velocity (insert) of positively charged particles measured at $HAB = 150$ mm, $[TEOS] = 400$ ppm and $\phi = 0.3$

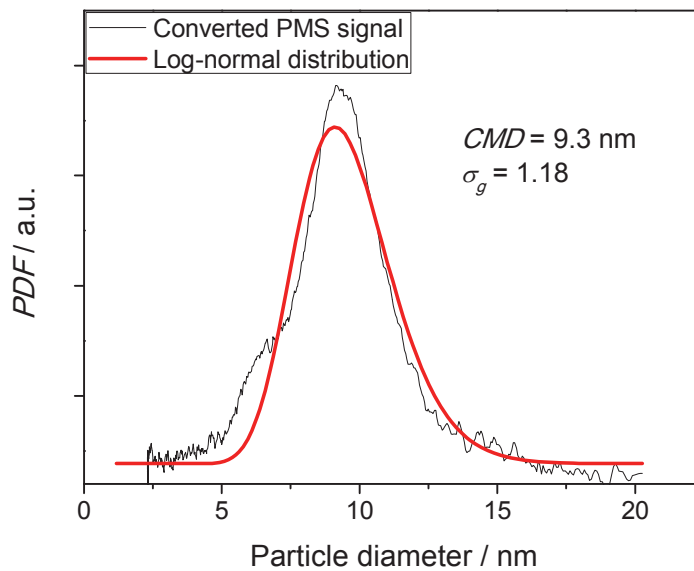


Figure 5.45: PDF of particle diameter determined from Figure 5.44. Log-normal fit of the measured signal yields $d_p = 9.3$ nm and $\sigma_g = 1.18$. $HAB = 150$ mm, $[TEOS] = 400$ ppm and $\phi = 0.3$

5.3.1.1. Influence of the height above burner (*HAB*) on the mean particle size and particle size distribution

The influence of *HAB* on the mean particle size under the standard condition is presented in Figure 5.46. As shown in this figure, increasing the *HAB* from 130 to 290 mm causes the mean particle size to progressively increases. This is due to the longer characteristic time for coagulation and coalescence of the suspended particles in the synthesis chamber. It can also be seen that the profile of the particle growth changes to a steeper increase beyond 210 mm *HAB*. This behavior was unexpected because even at complete coalescence the particle size d_p would be directly proportional to the third root of the particle volume, $d_p \propto \sqrt[3]{V_p}$. This means that the profile in Figure 5.46 should be shallower than exhibited for $HAB \geq 210$ mm. The growth rate should be less than that for $HAB \leq 210$ mm. To understand this behavior a CFD simulation of the premixed low-pressure flame reactor was carried out under similar conditions within the CFD group of our institute. The CFD simulation showed an asymmetric temperature distribution due to the influence of gravity especially at longer distances from the burner head. It was found that only results of measurements with *HAB* up to 210 mm can be used for further discussion.

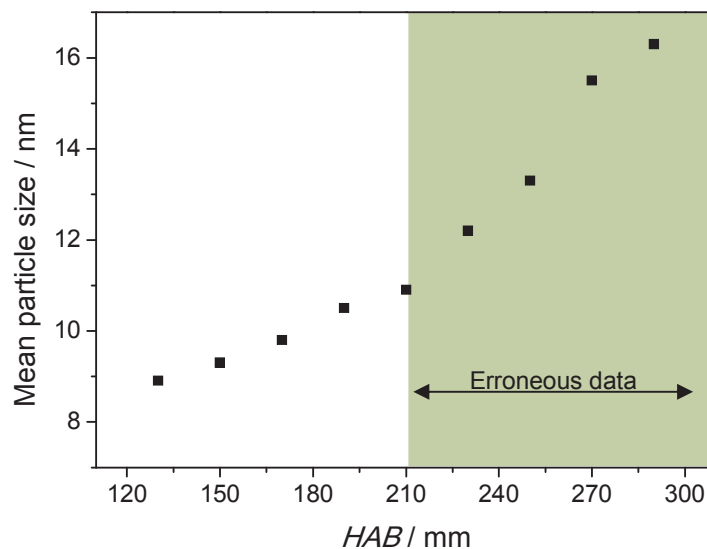


Figure 5.46: Influence of *HAB* on the mean particle size of silica nanoparticles synthesized in the low-pressure flame reactor under the standard conditions. [TEOS] = 400 ppm and $\phi = 0.3$

The first PMS signal could be seen clearly at 130 mm *HAB*. Before this point the PMS signals are very poor or there is no signal. It seems that particle formation starts just before 130 mm *HAB*. Figure 5.47 shows the mean particle size as a function of the residence time. The resi-

dence time was determined with means of the CFD simulation and was extracted from the centerline of the reactor. It seems that the silica start to nucleate just beyond 200 ms.

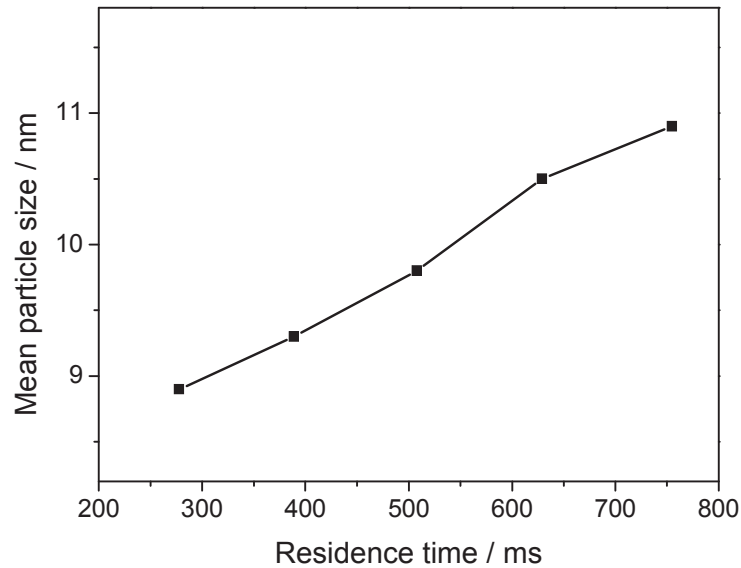


Figure 5.47: Mean particle size of silica nanoparticles as a function of residence time. [TEOS] = 400 ppm and $\phi = 0.3$

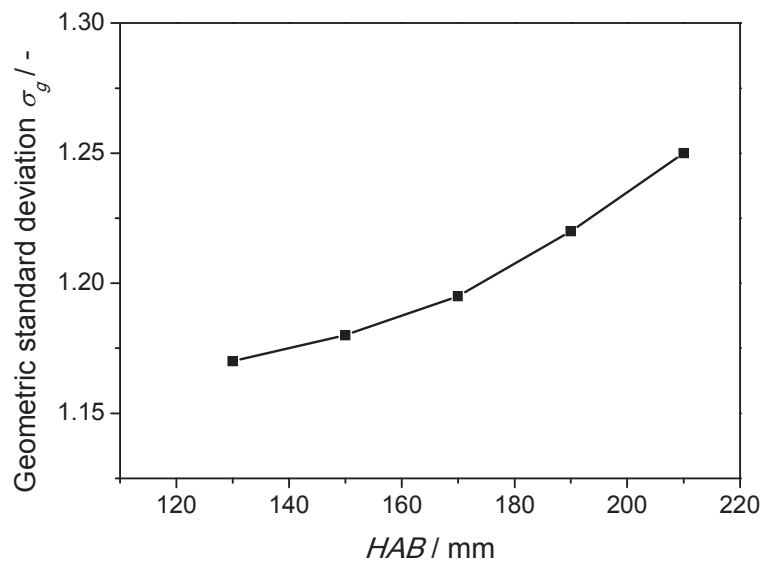


Figure 5.48: Geometric standard deviation σ_g as a function of HAB . [TEOS] = 400 ppm and $\phi = 0.3$

Measurements of the change in size distribution function with time can be used to determine the form of the particle growth law. Therefore, the geometric standard deviation σ_g from the log-normal fitting of the particle size distribution was also determined. As shown in Figure 5.48, σ_g rises from 1.17 to 1.25 with increasing HAB . This increase in σ_g is influenced

by the temperature-residence time history of the particles in the synthesis chamber. It has been found that the size distribution of a coagulating aerosol at long coagulation times approaches approximately a log-normal distribution function regardless of the initial size distribution [141, 142]. The geometrical deviation for such a self-preserving size distribution in the continuum regime is 1.35 [143, 144]. It can be seen in Figure 5.48 that the self-preserving size distribution is still not reached. In addition, the decrease in temperature in the direction of flow and incomplete coalescence of particles results in disperse particles, agglomerates and aggregates.

5.3.1.2. Influence of TEOS concentration on the mean particle size

The influence of TEOS concentration on the particle size has been investigated by varying the flow rate of the precursor mixture (0.2% TEOS in Ar) from the mixing vessel into the reactor. In order to keep the total volumetric flow rate constant, the difference from varying the precursor flow rate was compensated for by adjusting the argon flow rate. Figure 5.49 shows the PMS measurement of the mean particle size as a function of TEOS concentration. This investigation has been carried out at 190 mm *HAB* and under the standard conditions with variations in TEOS concentration from 100 to 500 ppm. Figure 5.49 also shows that the mean particle size increases with rising TEOS concentration due to higher collision frequency, coagulation and coalescence, all of which are a result of elevated monomer concentration.

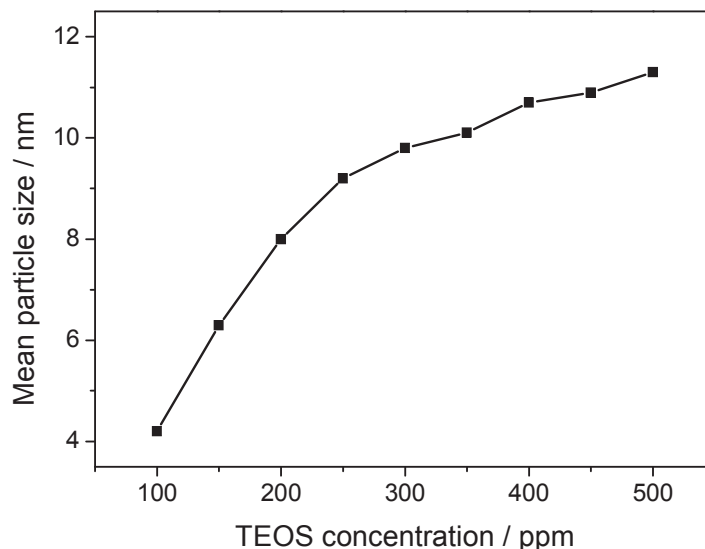


Figure 5.49: Influence of TEOS concentration on the mean particle size. *HAB* = 190 mm, $\phi = 0.3$

Figure 5.50 shows a comparison of the mean particle size at TEOS concentrations of 200 and 400 ppm as a function of *HAB*. It shows that the particle size at both TEOS concentrations rises with increasing *HAB* due to longer characteristic times for coagulation and coalescence.

As expected the particle size as a function of HAB for TEOS concentration of 400 ppm is higher than for 200 ppm TEOS. Increasing the precursor concentration rises the flame temperature and changes the temperature-residence time history downstream of the flame. This affects the coagulation and coalescence processes and thus leads to smaller particles.

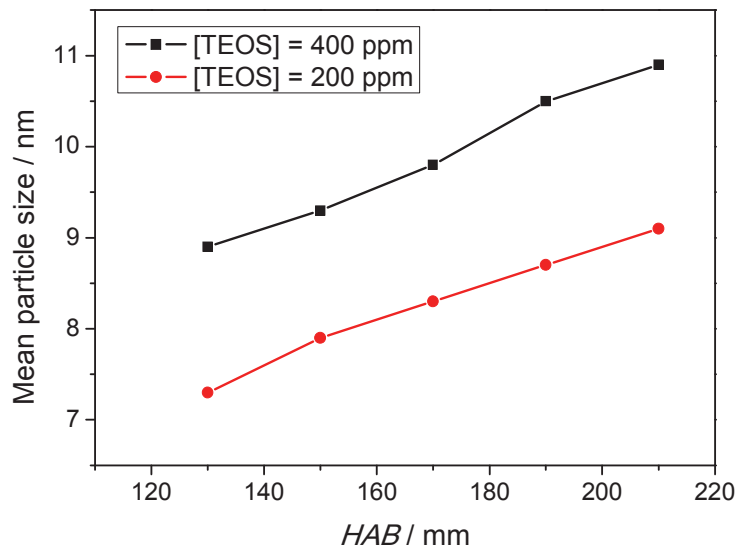


Figure 5.50: Mean particle size as a function of HAB at TEOS concentrations of 200 and 400 ppm. $\phi = 0.3$

5.3.1.3. Influence of the equivalence ratio ϕ on the mean particle size

Varying the hydrogen/oxygen ratio in the range of stoichiometric combustion has a strong influence on the flame temperature, flame velocity and flame length at constant mass flow rates of the inlet gases and reactor pressure. This will change the temperature time history along the reactor, which influences the kinetics of particle formation and growth and hence the mean particle size at the end of the reactor. The equivalence ratio ϕ was varied between 0.3 and 0.77 at 190 mm HAB to explore its influence on the mean particle size. The variation of equivalence ratio was achieved by altering both hydrogen and oxygen flow rates whilst keeping the total flow rate constant. Figure 5.51 shows that the mean particle size decreases when ϕ rises from 0.3 up to 0.77. This can be explained by two factors. Firstly, the rise in equivalence ratio at a constant total mass flow and pressure increases the flame temperature as well as the flame velocity and decreases the residence time in the reactor chamber. Secondly, at a higher flame temperature a stable nucleus will form further away from the burner, where the gas temperature is lower. This can increase the number of nuclei until the critical cluster size is reached resulting in a higher number of particles that are smaller in size.

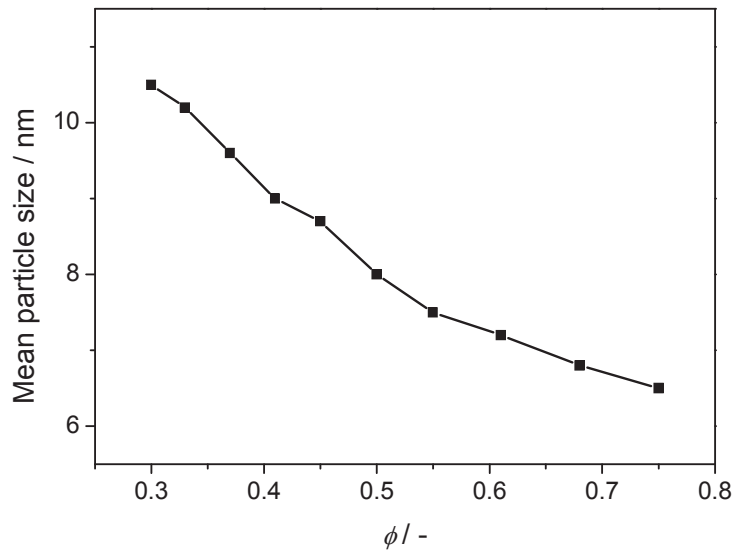


Figure 5.51: Mean particle size as a function of flame equivalence ratio ϕ . [TEOS] = 400 ppm, $HAB = 190$ mm

A comparison between two different flame equivalence ratios, $\phi = 0.3$ and 0.75 , is presented in Figure 5.52. It shows that with both equivalence ratios the particle size increases as a function of HAB due to the longer characteristic times for coagulation and coalescence. Figure 5.52 also illustrates that both profiles increase in an almost parallel fashion, whereas the profile of $\phi = 0.3$ is located at a higher particle size range than of $\phi = 0.75$. The results indicate that temperature plays a significant role in the formation process by controlling chemical kinetics.

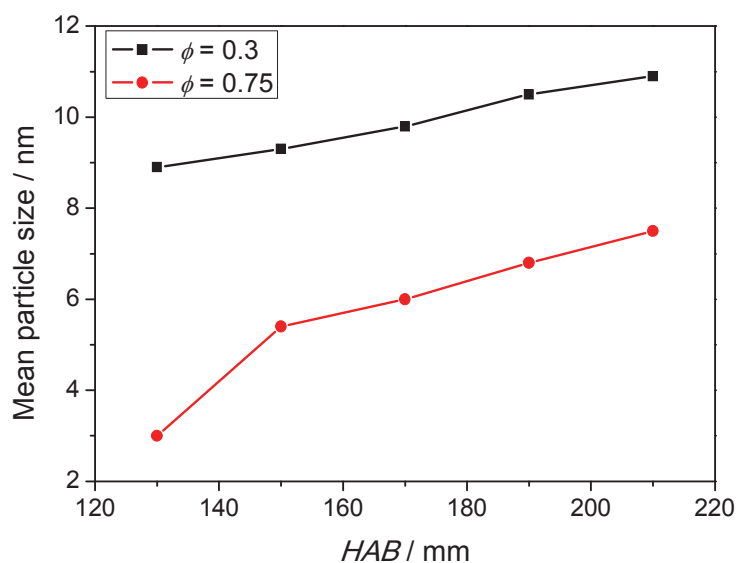


Figure 5.52: Mean particle size as a function of HAB at two different flame equivalence ratios of 0.33 and 0.75. [TEOS] = 400 ppm

These results indicate that the particle growth can be controlled through changes in temperature, precursor concentration and residence time.

5.3.2. Investigation of silica particle formation in the H₂/O₂/Ar flame reactor with HMDSO

The formation of silica nanoparticles from HMDSO was investigated under a variety of the main parameters in the low-pressure premixed H₂/O₂/Ar flame reactor with means of the particle mass spectrometer (PMS). The standard conditions for these experiments with HMDSO in the flame reactor are presented in Table 5.7. The main parameters were then systematically investigated with respect to the resulting particle size.

Table 5.7: Process parameters for silica synthesis in the H₂/O₂/Ar flame reactor

Parameter	Variation range	Standard condition	Unit
Height above burner (HAB)	110–210	130 – 210	mm
HMDSO concentration	67–150	100	ppm
Ar mass flow rate	400–600	400	sccm
O ₂ mass flow rate	280–500	400	sccm
H ₂ mass flow rate	300–520	400	sccm
Equivalence ratio ϕ	0.3–0.77	0.5	-
Reactor pressure	30	30	mbar

An example of the PMS signal is shown in Figure 5.53a. The maximum current of 0.26 pA was detected at a deflection voltage of 95 V for silica nanoparticles synthesized under the standard conditions and at *HAB* of 190 mm. The PMS signal of the experiments with HMDSO is about 30% weaker in comparison to the experiments with TEOS and the signal-to-noise ratio is therefore higher. The standard conditions used for TEOS could not be used for HMDSO because the signals were too weak. Therefore, a different set of standard conditions for HMDSO were defined, as shown in Table 5.7, since these provided the highest PMS signal. It seems that in this case a higher portion of charged silica nanoparticles is produced from TEOS than from HMDSO. It must be noted that the particles are charged by the particle synthesis process itself and not from any external source. The particle size distribution was determined using the information from Figure 5.53a, the bulk density of silica material (2.2 g/cm³) and the particle velocity that was measured previously. Figure 5.53b shows the probability density function (*PDF*) parameters that are obtained from a log-normal fit. The mean particle

size, which is equivalent to the count median diameter (*CMD*), was 11 nm with a standard deviation of $\sigma_g = 1.34$.

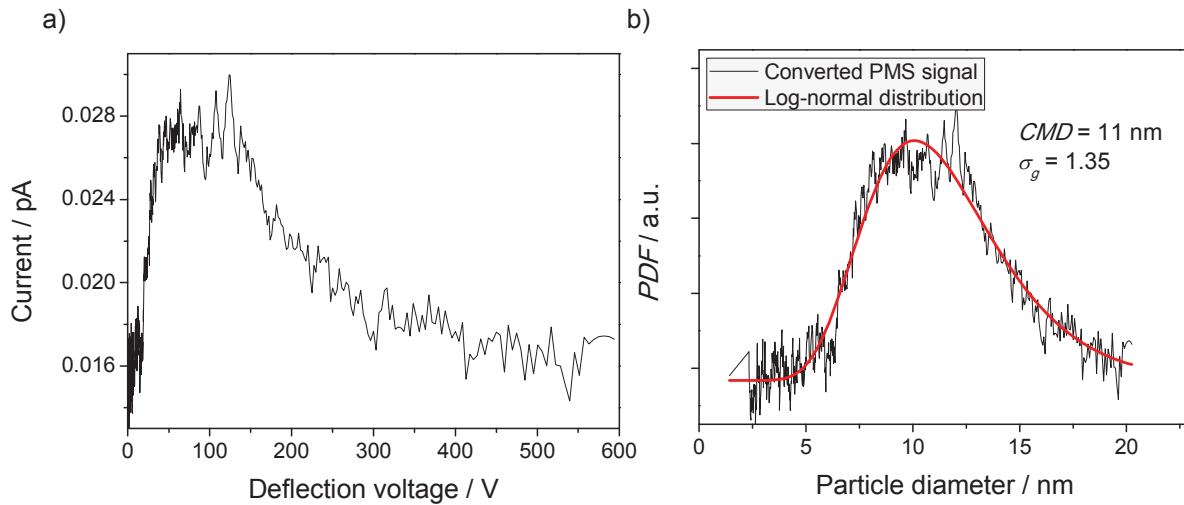


Figure 5.53: a) PMS current/voltage signal at 190 mm *HAB* and 100 ppm HMDSO, b) *PDF* of particle diameter determined from the log-normal fit of the measured signal yields $d_p = 11$ nm and $\sigma_g = 1.34$

5.3.2.1. Influence of the height above burner (*HAB*) on the particle size and the particle size distribution

The influence of the height above burner (*HAB*) on the mean particle size was investigated under the standard conditions. Figure 5.54 shows that with increasing *HAB* from 110 to 210 mm a progressive increase in the mean particle size from 10 to 11 nm was observed. This increase in particle size is because of the longer characteristic time for coagulation and coalescence of the suspended particles in the synthesis chamber. Despite the weaker PMS signal, the experiments with HMDSO show an earlier particle formation, here at 110 mm, in contrast with the experiments with TEOS. It can also be seen that beyond 190 mm *HAB* no further particle growth takes place.

It was also observed that the *HAB* has an influence on the geometric standard deviation σ_g , as seen in the log-normal fitting of the particle size distribution presented in Figure 5.55. This figure shows that σ_g rises from 1.25 to 1.35 with increasing *HAB* due to the temperature time history of the particles in the synthesis chamber. Figure 5.55 also shows that the particle size distribution approaches the self-preserving value of 1.35 at 190 mm *HAB* and remains constant for further increases in *HAB*. This result of the self-preserving size distribution of $\sigma_g = 1.35$ is in a good agreement with the studies of Friedlander et al. [143] and Lai et al. [144].

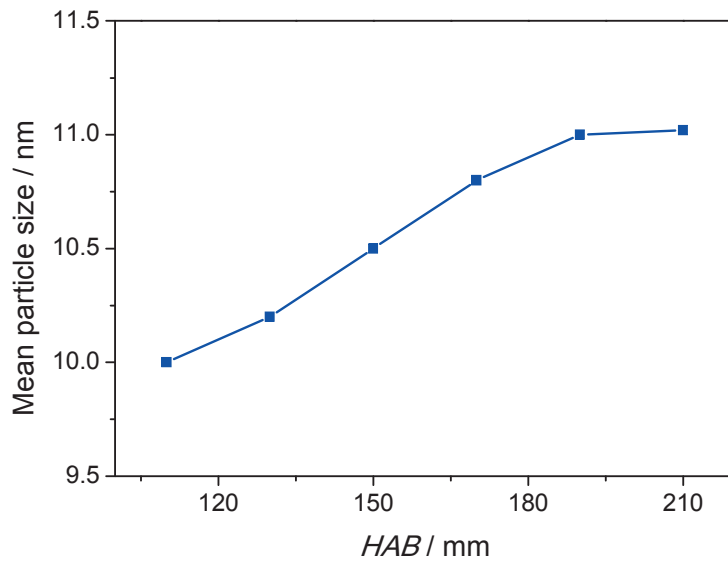


Figure 5.54: Influence of HAB on the mean particle size of silica nanoparticles synthesized in the low-pressure flame reactor under the standard conditions. $[HMDSO] = 100 \text{ ppm}$, $\phi = 0.5$

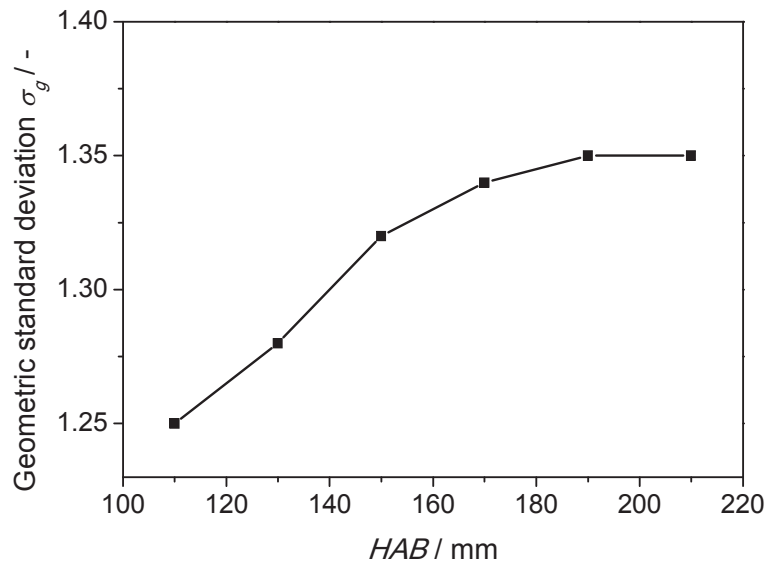


Figure 5.55: Geometric standard deviation σ_g as a function of HAB . $[HMDSO] = 100 \text{ ppm}$, $\phi = 0.5$, $p = 30 \text{ mbar}$

5.3.2.2. Influence of the HMDSO concentration on the mean particle size

The investigation of the influence of HMDSO concentration on the mean particle size was carried out in the same manner as done for TEOS by varying the flow rate of the precursor mixture (0.2 % HMDSO in Ar) from the mixing vessel into the reactor. The difference of the precursor flow rate was compensated by adjusting the argon flow rate to maintain a constant total volumetric flow rate. For this investigation the HMDSO concentration was varied between 67 and 150 ppm at 190 mm *HAB*. Figure 5.56 shows that with increasing HMDSO concentration the mean particle size increases significantly from 8.2 to 11.8 nm. This is due to the increase in frequency of collisions, coagulation and coalescence, as a result of elevated monomer concentration.

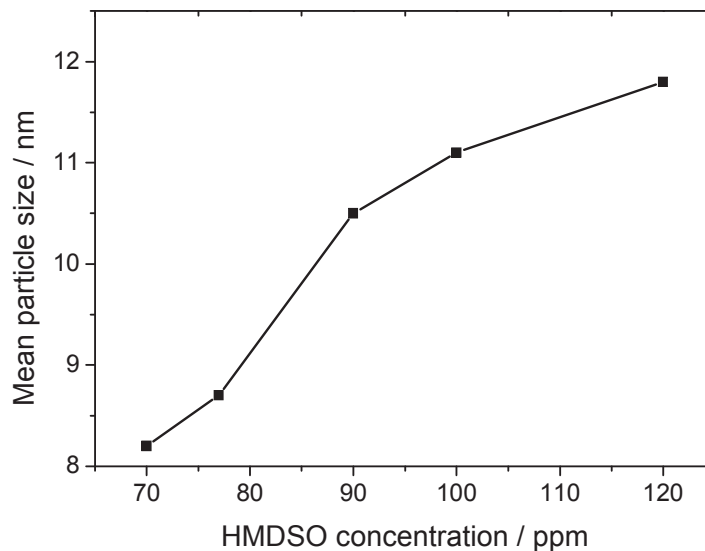


Figure 5.56: Influence of the HMDSO concentration on the particle size. *HAB* = 190 mm, $\phi = 0.5$, $p = 30$ mbar

In order to compare the influence of the concentration on the residence time history the mean particle size as a function of *HAB*, for three different HMDSO concentrations of 70, 77 and 100 ppm, was investigated. Figure 5.57 shows that the mean particle size increases with rising HMDSO concentration as well as with increasing *HAB*.

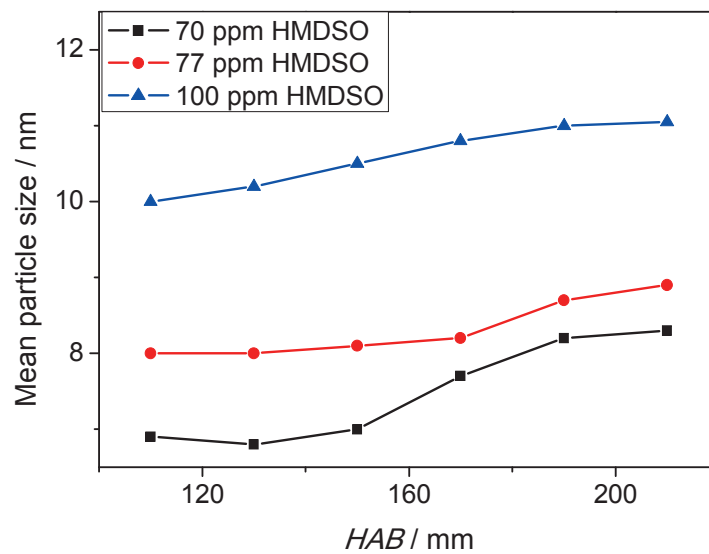


Figure 5.57: Particle size as a function of HAB for different HMDSO concentrations

5.3.2.3. Influence of the equivalence ratio on the mean particle size

The influence of the flame temperature on the particle formation was investigated by varying the equivalence ratio ϕ , between 0.3 and 0.77. It is known that ϕ affects the temperature time history along the reactor. Figure 5.58 shows that the mean particle size decreases with increasing ϕ from 0.3 up to 0.77.

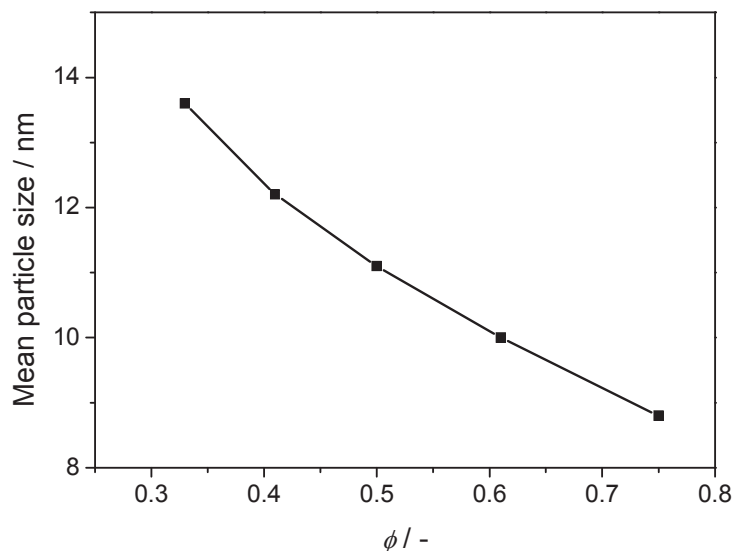


Figure 5.58: Mean particle size as a function of equivalence ratio ϕ . $HAB = 190$ mm, $[HMDSO] = 100$ ppm, $p = 30$ mbar

The influence of ϕ on the mean particle size as a function of HAB was observed. For this investigation three cases with $\phi = 0.3, 0.5$ and 0.77 were chosen. Details about the experimental conditions of this investigation are described in Table 5.8. Figure 5.59 shows that for $\phi = 0.3$ and 0.5 cases used, the slope of the particle growth appears to be almost similar, whilst the particle size is in different ranges for each case. However, for $\phi = 0.77$ case the particle size increases steeper in the colder zone of the flame.

Table 5.8: Experimental conditions for investigating the influence of the flame equivalence ratio on the particle size (cf. Figure 5.49)

$\phi / -$	Mass flow rates / slm			[HMDSO] / ppm	HAB / mm
	Ar	O ₂	H ₂		
0.3	400	480	320	100	130–210
0.5	400	400	400	100	130–210
0.77	400	320	480	100	130–210

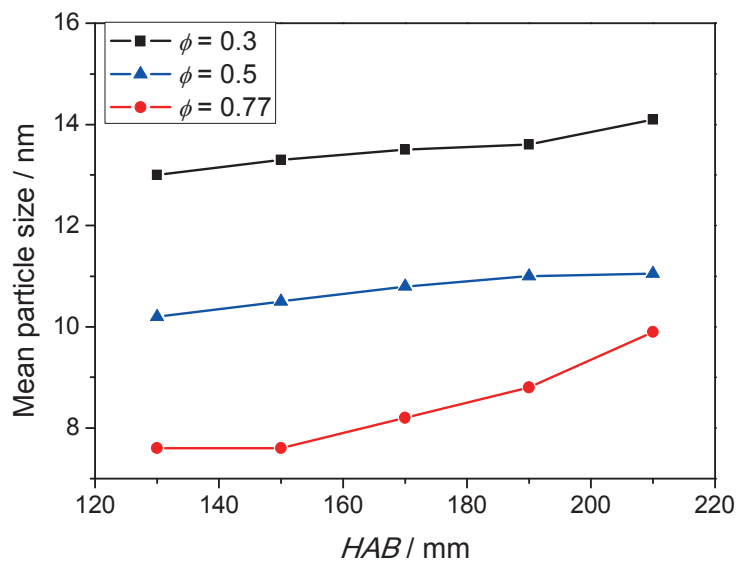


Figure 5.59: Influence of equivalence ratio ϕ on the particle size along the reactor axis from 130 to 210 mm HAB . [HMDSO] = 100 ppm, $p = 30$ mbar

5.4. Gas-dynamically induced particle synthesis (GIP reactor)

Several experiments were carried out in the GIP reactor by EVONIK in Hanau, Germany, using TEOS as well as HMDSO. Experiments with TEOS showed that under a wide range of parameters the silica nanoparticles in the reaction volume are polydisperse (cf. Figure 5.60a). However, at the absolute filter they are highly agglomerated and this is similar to the results from the microwave-plasma reactor (cf. Figure 5.60b). Particle aggregation in the filter is also due to the hydroxyl-group on the surface of the particles. Moreover, the high level of moisture in the initial gas mixture may additionally increase the hydroxyl-group number on the particles' surface.

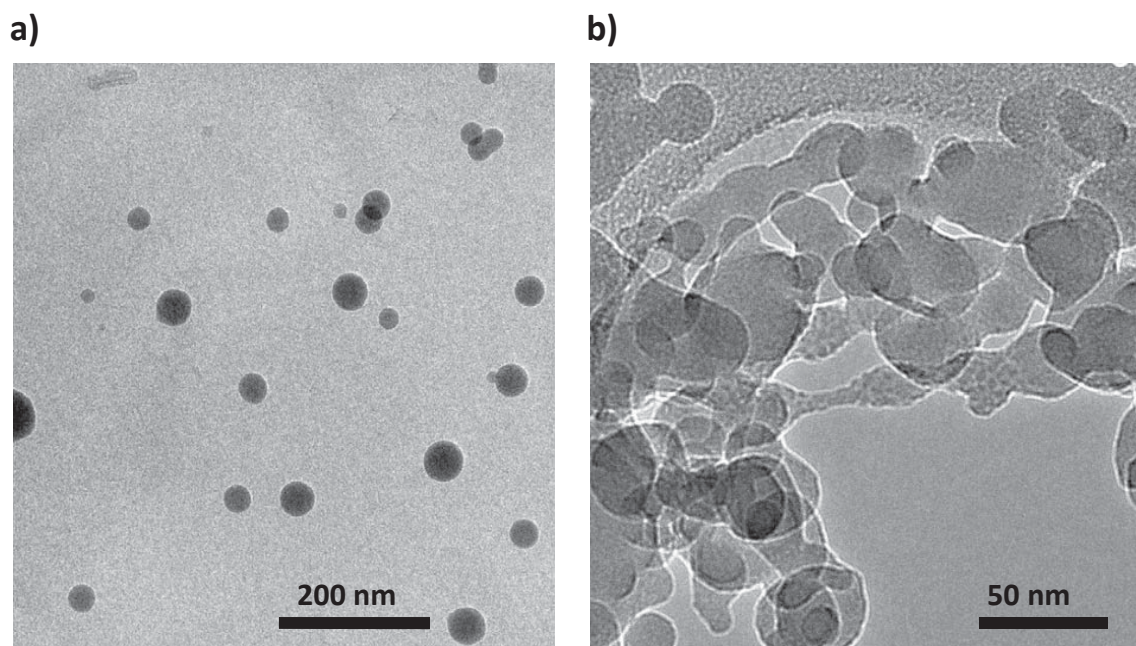


Figure 5.60: TEM-images of the particles sampled from a) the reaction volume of the GIP reactor and b) the filter located downstream of the GIP reactor. TEOS flow rate 0.5 kg/h

Furthermore, a few experiments were carried out in the GIP reactor using HMDSO as the precursor. Due to the lack of detailed kinetics data, similar experimental conditions were used for the experiments with TEOS and HMDSO. Only the concentration of HMDSO used was lower than that of TEOS. Figure 5.61 shows a TEM image of particles sampled from the reaction volume. The image shows dispersed particles are mixed with some form of liquid. It is still not clear, exactly what kind of liquid it is. It seems to be some type of carbon compound that has been formed due to incomplete combustion of all HMDSO species. The ignition delay times of HMDSO under this condition (1200 K) is almost 10 ms (see section 5.1.2.4), which consumes most of the residence time beyond the shock wave in the reaction volume. This GIP reactor was designed for TEOS. For it to be used with HMDSO a higher initiation temperature and/or extended reactor length would be required. These results also

support the assumption that it is the shock wave, and not the temperature at the nozzle, that initiates the reactions.

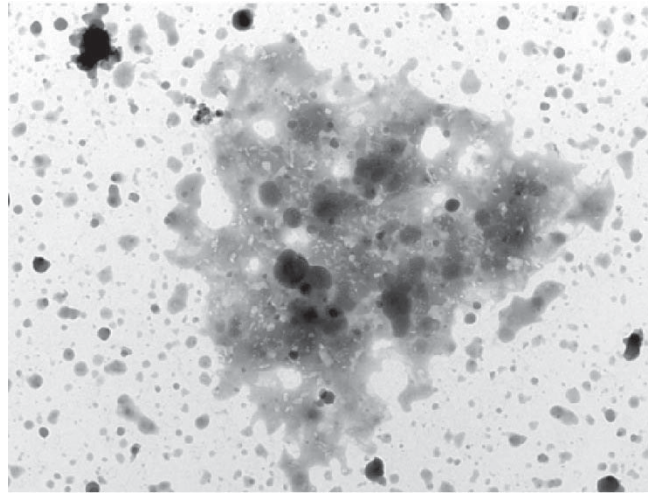


Figure 5.61: TEM-image from the particles sampled from the reaction volume of the GIP reactor. HMDSO flow rate is 0.18 kg/h

5.5. Comparison between TEOS and HMDSO

The comparison of results from TEOS and HMDSO can illustrate the extent to which the choice of the precursor can affect the mechanism of particle formation and growth.

5.5.1. Ignition delay times

Comparison between the ignition delay times of TEOS and HMDSO provides useful information for choosing the right precursor for the synthesis. This also depends on the type of reactor and the range of the initiation temperature. For example, in the microwave plasma reactor ignition delay times in dry synthetic air should be considered. Figure 5.62 shows the ignition delay times of TEOS and HMDSO in moist and dry synthetic air. The ignition delay times of HMDSO are longer than those of TEOS in dry synthetic air for the entire temperature range investigated. However, the ignition delay times of HMDSO exhibit a steeper slope than for TEOS in moist synthetic air. The lines fitted to the ignition delay time data for TEOS in moist synthetic air and for HMDSO cross each other at $T = 1530$ K. In the colder region the ignition delay times of HMDSO are evidently longer. This can also provide the information needed for the synthesis of nanoparticles in the GIP reactor, where high levels of moisture and shock wave temperatures below 1300 K are present. Furthermore, the choice of the precursor as well as the gas temperature behind the shock wave in the colder region of the ignition delay times play a crucial role on the length of the reaction volume in the GIP reac-

tor. However, at high temperatures beyond 1500 K the ignition delay time plays a negligible role due to the very short time required for the precursor reactions. This means the choice of precursor will only affect the mechanisms of the particle formation and growth at high temperatures.

The gas temperature at the precursor injector in the GIP reactor is limited to 1300 K due to the temperature stability of the wall material. This means using TEOS for the GIP reactor will limit the distance between the first nozzle and shock wave. On the other hand, the long ignition delay time of HMDSO requires a longer reaction volume. Therefore, TEOS was found to be preferred for the post shock wave regime, where it is possible to reduce the distance between the nozzle and shock wave.

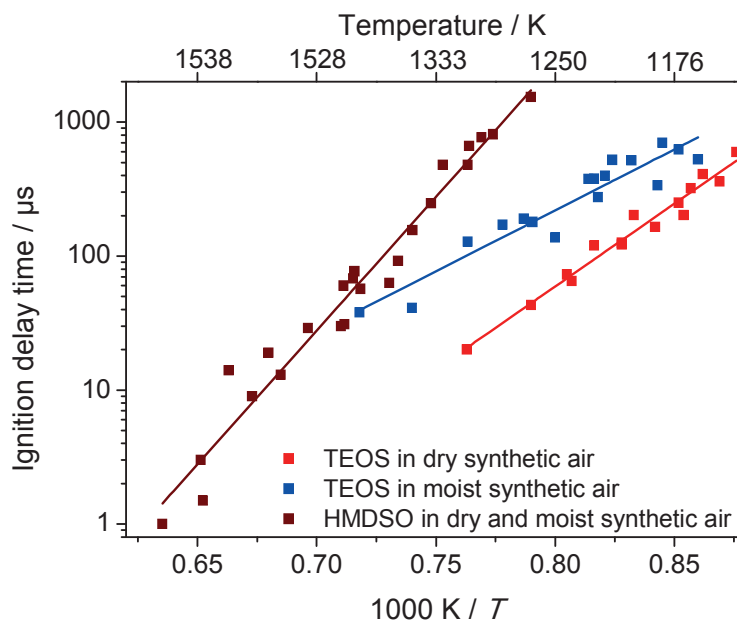


Figure 5.62: Comparison between the ignition delay times of HMDSO and TEOS in dry and moist synthetic air

5.5.2. Investigation of the particle formation in the flame reactor

The most interesting part of this work is to compare TEOS and HMDSO in the final product properties. Figure 5.63 shows the mean particle size as a function of HAB using TEOS and HMDSO. To achieve a similar Si atom concentration in the flame reactor the TEOS concentration used was double the HMDSO concentration. It can be clearly seen in Figure 5.63 that the particles formed using HMDSO are about 5 nm bigger than those formed using TEOS. This is also in good agreement with Kraft et al. [38] who state that silicic acid is the final stable product from TEOS decomposition. This means that the formation of SiO_2 from TEOS is achieved by the combustion of $\text{Si}(\text{OH})_4$, while HMDSO still has Si-O-Si bonds.

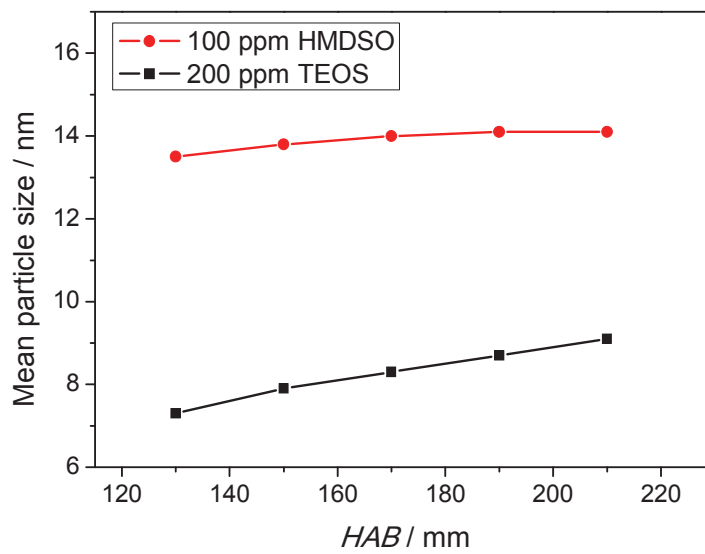


Figure 5.63: Comparison of the particle size as a function of HAB between TEOS and HMDSO. [Si] = 200 ppm, $\phi = 0.3$, $p = 30$ mbar

6. Conclusions

Silica nanoparticles are considered to be one of the most industrially produced nanomaterials. Due to the increasing number of applications that require highly specified silica nanoparticles, more control of the reactions and particle growth is needed. Moreover, the industrial interest in silica particle formation from metal-organic precursors has increased. However, to use these precursors more kinetics data are required for designing the suitable reactors. An example of where such detailed kinetics data has been required is for realization of the novel concept of gas-dynamically induced particles for continuous production of silica nanoparticles in the gas phase [90, 91]. This reactor, for which some work has been carried out in this thesis, relies on instantaneous heating and cooling rates for fast and homogeneous initiation and freezing of the reactions. This behavior allows highly dispersed nanoparticles with a narrow particle size distribution to be produced.

For this work tetraethoxysilane (TEOS) and hexamethyldisiloxane (HMDSO) as halide-free and inexpensive precursor materials were chosen. Due to the lack of the kinetics data of TEOS and HMDSO, kinetic studies of the precursor decomposition, ignition delay times as well as the study of particle formation and growth are essential.

The precursor chemistry and the particle formation were studied in this thesis individually. The kinetics of TEOS and HMDSO decomposition and oxidation were studied in shock tube facilities. Investigation of the precursor decomposition was carried out by utilizing a high-repetition time-of-flight mass spectrometer at the shock tube for online measurements. The mass spectra show that a wide range of species between $m/z = 12$ and 46 are produced from TEOS decomposition. The data also show that the strongest peak is at $m/z = 28$ which represents ethylene as the main product of TEOS decomposition. In addition to ethylene, a substantial amount of ethanol was observed. The concentration-time history of ethylene and ethanol show a good agreement with the study of Herzler et al. [36]. It was also found that Si(OH)_4 is formed from the decomposition of TEOS. This result supports the estimation of Kraft et al. [38].

Furthermore, the results showed a wide range of species, between $m/z = 12$ and 73 constituting both organic as well as Si-containing species, from the decomposition of HMDSO behind the reflected shock-wave. The strongest peak was observed at $m/z = 28$ which is indicative of ethylene and free Si atoms. The formation of Si atoms from the decomposition of HMDSO was verified with means of absorption resonance atomic spectroscopy (ARAS) in the temperature range between 1350 and 1993 K. It was concluded from the TOF-MS results that several monomers are produced from the decomposition of HMDSO. They are mainly Si atoms, SiO and Si-O-Si. They can be found as free atoms and molecules or joined with one or



more hydrogen atoms and/or methyl groups. The concentration of each species depends strongly on the temperature.

The ignition delay times of TEOS and HMDSO were investigated in shock-tube facilities as well. The ignition delay times of TEOS and HMDSO in dry as well as moist synthetic air were measured by observing the OH* emission signal behind the reflected shock wave. The results show that the ignition delay times of TEOS and HMDSO depend strongly on the temperature and they can follow the Arrhenius behavior. The presence of water vapor in the initial gas mixture showed a strong influence on decreasing the ignition delay times of TEOS whereas the moist atmosphere did not exhibit any effect on the ignition delay time of HMDSO.

For the investigation of silica-particle formation and growth, a hybrid microwave-plasma hot-wall reactor was constructed. Initially the plasma temperature behind the microwave-antenna was measured using the multi-line NO-LIF temperature imaging technique. The results showed the progressive influence of the microwave power and reactor pressure on the temperature. The temperature increases linearly with rising microwave power (from 100 to 500 W) whereas a temperature saturation can be observed for pressures above 60 mbar. Furthermore, the results show that adding TEOS to the initial gas mixture dramatically alters the gas temperature outside the antenna. It was understood from the behavior of the temperature profile that TEOS decomposes almost completely in the microwave antenna and combustion of the decomposition products such as ethylene and ethanol cause a temperature increase just after the antenna exit.

Particle synthesis in the microwave-plasma reactor was studied with varied TEOS concentrations between 580 and 7000 ppm and microwave powers between 150 and 450 W. Results showed that the greatest particle size is achieved with a TEOS concentration of around 4000 ppm. The microwave power, which clearly influenced the temperature in the plasma, did not affect the particle size in the power range studied. A hot-wall furnace was added to the microwave-plasma reactor in order to extend the residence time at high temperatures. It was found that for a furnace temperature higher than 400°C thermionization greatly hinders the particle growth. Furthermore, the reactor pressure or residence time showed a linear relationship with particle growth. Moreover, the particle morphology was observed from the reactor chamber and the collected particles in the filter with means of transmission electron microscopy (TEM). The results showed that the particles in the gas phase were polydisperse but not agglomerated, whereas the particles from the filter were highly agglomerated. FTIR spectroscopy exhibited that the silica particles from the combustion of TEOS contain a high number of OH groups on the particle surface. This is the reason for the sintering at room temperature. This is in support of the fact that silicic acid is a main monomer that is produced from TEOS decomposition.



Silica nanoparticles were also synthesized in a low-pressure premixed $H_2/O_2/Ar$ flame reactor from TEOS and HMDSO. Utilizing a particle mass spectrometer (PMS) allows the particle growth and the change in particle size distribution to be studied. The results showed that the particle size rises with increasing height above burner (*HAB*) and precursor concentration. However, the particle size decreases at higher temperatures. A comparison between both precursors in the flame reactor showed that silica nanoparticles from HMDSO are about 40% bigger in size than from TEOS. This demonstrates the strong influence of the different decomposition intermediates on the particle size and even particle size distribution.

The present research work provides data and more understanding of TEOS and HMDSO decomposition kinetics and particle formation and growth in different gas-phase reactors. These data were used to design the novel reactor for gas-dynamically induced particles as a practical application. However, they can also be used for the design of any other gas-phase reactors.



7. Recommendation for future work

The knowledge gained from this work can be utilized to extend the research of the gas-phase kinetics of the decomposition of tetraethoxysilane (TEOS) and hexamethyldisiloxane (HMDSO) and the formation and growth of silica nanoparticles. Some of the research recommendations are given below. Most of the studies in the literature assumed single-step reactions or are based on kinetics information from stable products. Detailed kinetics mechanisms are rudimentary without species concentration validation.

In this work, the kinetics study was carried out in shock-heated gases with species concentration measurements by high-repetition-rate time-of-flight mass spectrometry. Further experiments are recommended to enable building a detailed kinetics model, especially for HMDSO.

A study of the initial phase of silica particle formation is also highly recommended. This can be achieved by employing the light scattering/extinction technique in shock-tube experiments. This method has been used to measure the soot and silicon particle formation, where visible light is strongly attenuated after the inception of particles due to absorption and scattering. However, for silica nanoparticles shock-tube experiments are much more difficult due to the very limited absorption of the resulting white powder. These measurements will require the selection of a suitable wavelength that prevents interference from absorption of precursor molecules and intermediate species.

The presence of water vapor in the initial gas mixture has shown a clear influence on the ignition delay times of TEOS. For future work, the impact of water vapor influence on the gas-phase chemistry, particle formation and growth especially in the microwave plasma reactor should be further elucidated. Species concentration measurements should be employed on new classes of precursors.



8. References

1. Kusters KA, Pratsinis SE. Strategies for control of ceramic powder synthesis by gas-to-particle conversion. *Powder Technology* 1995,82:79-91.
2. Sumiya H, Irifune T. Synthesis of High-Purity Nano-Polycrystalline Diamond and Its Characterization. *Most* 2000,3:52-59.
3. Juehne T. Nanomaterials for Advanced Applications. In: *ChemFiles*. St. Luis.: Sigma-Aldrich Corp; 2005.
4. Gutsch A, Mühlenweg H, Krämer M. Tailor-Made Nanoparticles via Gas-Phase Synthesis. *Small* 2005,1:30-46.
5. Grassian VH. When Size Really Matters: Size-Dependent Properties and Surface Chemistry of Metal and Metal Oxide Nanoparticles in Gas and Liquid Phase Environments†. *The Journal of Physical Chemistry C* 2008,112:18303-18313.
6. Tsantilis S, Pratsinis SE. Soft- and Hard-Agglomerate Aerosols Made at High Temperatures. *Langmuir* 2004,20:5933-5939.
7. Slowing II, Trewyn BG, Giri S, Lin VSY. Mesoporous Silica Nanoparticles for Drug Delivery and Biosensing Applications. *Advanced Functional Materials* 2007,17:1225-1236.
8. Bonacchi S, Genovese D, Juris R, Montalti M, Prodi L, Rampazzo E, Sgarzi M, Zaccheroni N. Luminescent Chemosensors Based on Silica Nanoparticles Luminescence Applied in Sensor Science. In. Edited by Prodi L, Montalti M, Zaccheroni N: Springer Berlin / Heidelberg; 2011. pp. 93-138.
9. Mueller R, Kammler HK, Pratsinis SE, Vital A, Beaucage G, Burtscher P. Non-agglomerated dry silica nanoparticles. *Powder Technology* 2004,140:40-48.
10. Pitkänen A, Mäkelä JM, Nurminen M, Oksanen A, Janka K, Keskinen J, Keskinen H, Liimatainen JK, Hellstén S, Määttä T. Numerical Study of Silica Particle Formation in Turbulent H₂/O₂ Flame. *Journal of the International Flame Research Foundation* 2005.
11. Nakaso K, Han B, Ahn KH, Choi M, Okuyama K. Synthesis of non-agglomerated nanoparticles by an electrospray assisted chemical vapor deposition (ES-CVD) method. *Journal of Aerosol Science* 2003,34:869-881.
12. Du J, Tu H, Wang L. Non-agglomerated silicon nanoparticles on (001) silicon substrate formed by PLA and their photoluminescence properties. *Materials Science and Engineering: B* 2009,159–160:61-65.
13. Pratsinis SE, Mastrangelo SVR. Material synthesis in aerosol reactors. *Chemical Engineering Progress* 1989,85: 62-66.



14. Chen C, Cheng J, Yu S, Che L, Meng Z. Hydrothermal synthesis of perovskite bismuth ferrite crystallites. *Journal of Crystal Growth* 2006,291:135-139.
15. Gutsch A, Krämer M, Michael G, Mühlenweg H, Pridöhl M, Zimmermann G. Gas-Phase Production of Nanoparticles. *KONA powder and particle journal* 2002,20:24 - 37.
16. Kruis FE. Synthesis of nanoparticles in the gas phase for functional applications. Duisburg: Universität Duisburg-Essen; 2001.
17. Sotiris E P. Flame aerosol synthesis of ceramic powders. *Progress in Energy and Combustion Science* 1998,24:197-219.
18. Giglmaier M, Al-Hasan NS, Adams NA. 3-D Simulation of the Production of Gas-phase synthesized Non-aggregated Spherical Nano-particles in Continuous Gasdynamic Flow In: *7th International Conference on Multiphase Flow*. Tampa, FL.; 2010.
19. Al-Hasan NS, Schnerr GH. 3-D Modeling of Shock-induced Precursor Decomposition and Nano-Particle Growth. *PAMM* 2008,8:10581-10582.
20. Wegner K, Pratsinis SE. Scale-up of nanoparticle synthesis in diffusion flame reactors. *Chemical Engineering Science* 2003,58:4581-4589.
21. Iler R. The Chemistry of Silica. John Willey and Sons, New York 1979.
22. Huang Y, Kinloch AJ. Modelling of the toughening mechanisms in rubber-modified epoxy polymers. *Journal of Materials Science* 1992,27:2763-2769.
23. Sangermano M, Messori M. Scratch Resistance Enhancement of Polymer Coatings. *Macromolecular Materials and Engineering* 2010,295:603-612.
24. Quercia G, Brouwers HJH. Application of nano-silica (nS) in concrete mixtures. In: *8th fib PhD Symposium in Kgs. Lyngby, Denmark*; 2010.
25. DeMuth P, Hurley M, Wu C, Galanie S, Zachariah MR, DeShong P. Mesoscale porous silica as drug delivery vehicles: Synthesis, characterization, and pH-sensitive release profiles. *Microporous and Mesoporous Materials* 2011,141:128-134.
26. Giri S, Trewyn BG, Lin VSY. Mesoporous silica nanomaterial-based biotechnological and biomedical delivery systems. *Nanomedicine* 2007,2:99-111.
27. Grieve K, Mulvaney P, Grieser F. Synthesis and electronic properties of semiconductor nanoparticles/quantum dots. *Current Opinion in Colloid & Interface Science* 2000,5:168-172.
28. Trindade T, O'Brian P, Pickett. Nanocrystalline semiconductors: Synthesis, properties, and perspectives. *Chem. Mater.* 2001,13.



29. Murray CB, Kagan CR, Bawendi MG. Synthesis and characterization of monodisperse nanocrystals and closed-packed nanocrystal assemble. *Annual Review of Materials Science* 2000,30:545-610.
30. Kammler HK, Mädler L, Pratsinis SE. Flame Synthesis of Nanoparticles. *Chemical Engineering & Technology* 2001,24:583-596.
31. Swihart MT. Vapor-phase synthesis of nanoparticles. *Current Opinion in Colloid & Interface Science* 2003,8:127-133.
32. Strobel R, Alfons A, Pratsinis SE. Aerosol flame synthesis of catalysts. *Advanced Powder Technology* 2006,17:457-480.
33. Biskos G, Vons V, Yurteri CU, Schmidt-Ott A. Generation and Sizing of Particles for Aerosol-Based Nanotechnology. *KONA powder and particle journal* 2008,26:13-35.
34. Athanassiou EK, Grass RN, Stark WJ. Chemical Aerosol Engineering as a Novel Tool for Material Science: From Oxides to Salt and Metal Nanoparticles. *Aerosol Science and Technology* 2010,44:161-172.
35. Pratsinis SE. Aerosol Science and Technology: History and Reviews. In. Edited by Ensor DS: RTI Press; 2011.
36. Herzler J, Manion JA, Tsang W. Single-Pulse Shock Tube Study of the Decomposition of Tetraethoxysilane and Related Compounds. *The Journal of Physical Chemistry A* 1997,101:5500-5508.
37. R. J. Kee, Rupley FM, Miller JA, Coltrin ME, Grcar JF, Meeks E, Moffat HK, Lutz AE, Dixon-Lewis G, Smooke MD, Warnatz J, Evans GH, Larson RS, Mitchell RE, Petzold LR, Reynolds WC, Caracotsios M, Stewart WE, Glarborg P, Wang C, Adigun O. CHEMKIN, Reaction Design Inc. In. San Diago, CA; 2000.
38. Shekar A, Sander S, Rahiel RC, Smith AJ, Braumann A, Kraft M. A novel pathway for flame synthesis of silica nanoparticles. *Cambridge Center for Computational Chemical Engineering* 2010.
39. Phadungsukanan W, Shekar S, Shirley R, Sander M, West RH, Kraft M. First-Principles Thermochemistry for Silicon Species in the Decomposition of Tetraethoxysilane. *The journal of physical chemistry A* 2009,113:9041-9049.
40. Phadungsukanan W, Shirley R, Sander M, Kraft M. Development of a Detailed Kinetic Model to Study the Ignition Delay Time of Tetraethoxysilane (TEOS) in a Shock Tube. *Cambridge Center for Computational Chemical Engineering* 2008.
41. Chu JCS, Soller R, Lin MC, Melius CF. Thermal Decomposition of Tetramethyl Orthosilicate in the Gas Phase: An Experimental and Theoretical Study of the Initiation Process. *Journal of Chemical Physics* 1995,99:663-672.



42. Takeuchi H, Izumi H, Kawasaki A. Decomposition Study of TEOS in Thermal CVD. In: MRS Proceedings; 1993. pp. 45-59.
43. Chagger HK, Hainsworth D, Patterson PM, Pourkashanian M, Williams A. The formation of SiO₂ from hexamethyldisiloxane combustion in counterflow methane-air flames. *Symposium (International) on Combustion* 1996,26:1859-1865.
44. Wavhal DS, Zhang J, Steen ML, Fisher ER. Investigation of Gas Phase Species and Deposition of SiO₂ Films from HMDSO/O₂ Plasmas. *Plasma Processes and Polymers* 2006,3:276-287.
45. Carles S, Le Garrec JL, Mitchell JBA. Electron and ion reactions with hexamethyldisiloxane and pentamethyldisiloxane. *The Journal of Chemical Physics* 2007,127:144308-144307.
46. Burkert A, Müller D, Paa W. Si and SiO detection in a HMDSO/propane/air flame using spatially resolved optical emission spectroscopy (OES). *Journal of Quantitative Spectroscopy and Radiative Transfer* 2013,114:101-108.
47. Ulrich GD. Theory of Particle Formation and Growth in Oxide Synthesis Flames. *Combustion Science and Technology* 1971,4:47-57.
48. Ulrich GD, Subramanian NS. III. Coalescence as a Rate-Controlling Process. *Combustion Science and Technology* 1977,17:119-126.
49. Ahn KH, Jung CH, Choi M, Lee JS. Particle Sampling and Real Time Size Distribution Measurement in H₂/O₂/TEOS Diffusion Flame. *Journal of Nanoparticle Research* 2001,3:161-170.
50. Jang HD. Generation of Silica Nanoparticles from Tetraethylorthosilicate (TEOS) Vapor in a Diffusion Flame. *Aerosol Science and Technology* 1999,30:477-488.
51. Goortani BM, Mendoza N, Proulx P. Synthesis of SiO₂ Nanoparticles in RF Plasma Reactors: Effect of Feed Rate and Quench Gas Injection. *International Journal of Chemical Reactor Engineering* 2006,4.
52. Abdali A, Moritz B, Gupta A, Wiggers H, Schulz C. Hybrid microwave-plasma hot-wall reactor for synthesis of silica nanoparticles under well-controlled conditions. *Journal of Optoelectronics and Advanced Materials* 2010,12:440 - 444.
53. Hecht C, Abdali A, Dreier T, Schulz C. Gas-Temperature Imaging in a Microwave-Plasma Nanoparticle-Synthesis Reactor Using Multi-Line NO-LIF Thermometry. *Zeitschrift für Physikalische Chemie* 2011,225:1225-1235.
54. Zachariah MR, Semerjian HG. Experimental and Numerical-Studies on Refractory Particle Formation in Flames. *High Temperature Science* 1989,28:113-125.



55. Briesen H, Fuhrmann A, Pratsinis SE. The effect of precursor in flame synthesis of SiO₂. *Chemical Engineering Science* 1998,53:4105-4112.
56. Xiong Y, Pratsinis SE, Mastrangelo SVR. The effect of ionic additives on aerosol coagulation. *Journal of Colloid and Interface Science* 1992,153:106-117.
57. Schiel A, Weber AP, Kasper G, Schmid H-J. In-Situ Determination of the Charging of Nanometer and Submicron Particles at High Temperatures. *Particle & Particle Systems Characterization* 2002,19:410-418.
58. Reuter K, Meyer J, Kasper G. Investigation on the precipitation of particles charged by thermionic emission. In: *PARTEC*. Nürnberg; 2007.
59. Ehrman SH, Friedlander SK, Zachariah MR. Characteristics of SiO₂/TiO₂ nanocomposite particles formed in a premixed flat flame. *Journal of Aerosol Science* 1998,29:687-706.
60. Xiong Y, Kamal Akhtar M, Pratsinis SE. Formation of agglomerate particles by coagulation and sintering—Part II. The evolution of the morphology of aerosol-made titania, silica and silica-doped titania powders. *Journal of Aerosol Science* 1993,24:301-313.
61. Goertz V, Weis F, Keln E, Nirschl H, Seipenbusch M. The Effect of Water Vapor on the Particle Structure and Size of Silica Nanoparticles During Sintering. *Aerosol Science and Technology* 2011,45:1287-1293.
62. Lifshitz A. *Shock waves in chemistry*: M. Dekker; 1981.
63. Ho P, Melius CF. Theoretical study of the thermochemistry of molecules in the Si-O-H-C system. *Journal Name: Journal of Physical Chemistry; (United States); Journal Volume: 99:7* 1995:Medium: X; Size: Pages: 2166-2176.
64. Friedlander SK. *Smoke, Dust, and Haze: Fundamental of Aerosol Dynamics*. 2 ed. New York, Oxford: Oxford University Press; 2000.
65. Pratsinis SE, Vemury S. Particle formation in gases: A review. *Powder Technology* 1996,88:267-273.
66. Kodas TT, Hambden-Smith M. *Aerosol Processing of Materials*: WILEY-VCH; 1999.
67. Schubert U, Hüsing N. *Synthesis of Inorganic Materials*: John Wiley & Sons; 2012.
68. Schmelzer J. *Nucleation theory and applications*: Wiley-VCH; 2005.
69. Ibach H. *Physics of surfaces and interfaces*: Springer; 2006.
70. McDonald JE. Homogeneous Nucleation of Vapor Condensation. II. Kinetic Aspects. *American Journal of Physics*. 1963,31:31-41.
71. Kowalik A. Modellierung und Simulation der Synthese von Eisen-Nanopartikeln in Gasphasenreaktoren. Duisburg: Universität Duisburg-Essen; 2007.



72. Kingery WD, Bowen HK, Uhlmann DR. *Introduction to ceramics*: Wiley; 1976.
73. Helble JJ, Sarofim AF. Factors determining the primary particle size of flame-generated inorganic aerosols. *Journal of Colloid and Interface Science* 1989,128:348-362.
74. Buggele AE, Center LR. *Better vacuum by removal of diffusion-pump-oil contaminants*: National Aeronautics and Space Administration; 1975.
75. Redhead PA. *Vacuum Science and Technology: Pioneers of the 20th Century*: American Inst. of Physics; 1997.
76. Boer HJ. Liquid-injection system based on mass flow controllers. *Solid State Technology* 1996:149-152.
77. Bae SH, Shin HD. Generation of Silica Nanoparticles in Turbulent Non-premixed Flames with Oxygen Enrichment. *Energy & Fuels* 2009,23:5338-5348.
78. Vollath D. Plasma Synthesis of Nanoparticles. *KONA powder and particle journal* 2007,25:39-55.
79. Leins M. Development and Spectroscopic Investigation of a Microwave Plasma Source for the Decomposition of Waste Gases. Stuttgart: Universität Stuttgart; 2010.
80. Fristrom RM. *Flame structure and processes*: Oxford University Press; 1995.
81. Hippler R, Pfau S, Schmidt M, Schoenbach KH. *Low temperature plasma physics: fundamental aspects and applications*. Berlin: Wiley-VCH; 2001.
82. van der Mullen J, de Regt J. An active spectroscopical study on the plasma parameters of an ICP. *Fresenius' Journal of Analytical Chemistry* 1996,355:532-537.
83. Conrads H, Schmidt M. Plasma generation and plasma sources. *Plasma Sources Science and Technology* 2000,9:441.
84. Jankowski KJ, Reszke E, Barnett NW. *Microwave Induced Plasma Analytical Spectrometry*: Royal Society of Chemistry; 2010.
85. Brown SC. *Basic Data of Plasma Physics*. Cambridge: MIT Press; 1959.
86. Wegner K, Pratsinis SE. Nozzle-quenching process for controlled flame synthesis of titania nanoparticles. *AIChE Journal* 2003,49:1667-1675.
87. Ifeacho P, Huelser T, Wiggers H, Schulz C, Roth P. Synthesis of SnO_{2-x} nanoparticles tuned between $0 \leq x \leq 1$ in a premixed low pressure H₂/O₂/Ar flame. *Proceedings of the Combustion Institute* 2007,31:1805-1812.
88. Pauly H. *Atom, Molecule, and Cluster Beams*: Springer Verlag; 2000.
89. Roth P, Hospital A. Design and test of a particle mass spectrometer (PMS). *Journal of Aerosol Science* 1994,25:61-73.



90. Grzona A, Weiß A, Olivier H, Gawehn T, Gülhan A, Al-Hasan N, Schnerr GH, Abdali A, Luong M, Wiggers H, Schulz C, Chun J, Weigand B, Winnemöller T, Schröder W, Rakel T, Schaber K, Goertz V, Nirschl H, Maisels A, Leibold W, Dannehl M. Gas-phase synthesis of non-agglomerated nanoparticles by fast gasdynamic heating and cooling. In: *26th International Symposium on Shock Waves*. Edited by Hannemann K, Seiler F. Göttingen: Springer Berlin Heidelberg; 2007. pp. 857-862.
91. Al-Hasan NS. Numerische Untersuchung der Nanopartikelbildung in transsonischer Strömung" Dissertation under preparation. Munich: Technical University of Munich; 2010.
92. Al-Hasan NS, Giglmaier M, Schnerr GH. Numerical Investigation of the 3-D Unsteady Reactive Flow within a Gas Dynamic Particle Reactor. In: *Proc. World Congress on Particle Technology (WCPT6 2010)*. Nürnberg; 2010.
93. Kruis FE, Kusters KA, Pratsinis SE, Scarlett B. A Simple Model for the Evolution of the Characteristics of Aggregate Particles Undergoing Coagulation and Sintering. *Aerosol Science and Technology* 1993,19:514-526.
94. Mohri K, Luong M, Vanhove G, Dreier T, Schulz C. Imaging of the oxygen distribution in an isothermal turbulent free jet using two-color toluene LIF imaging. *Applied Physics B: Lasers and Optics* 2011,103:707-715.
95. Mohri K, Wohler A, Weigand B, Schulz C. Toluene laser-induced fluorescence (LIF) imaging of supersonic flow within a diverging duct. In: *28th International Symposium on Shock Waves*. Manchester; 2011.
96. Wohler A, Mohri K, Schulz C, Weigand B. Flow structures in subsonic-to-supersonic mixing processes using different injector geometries. In: *EUCASS*. St. Petersburg; 2011.
97. Rakel T, Schaber K. Rapid quenching by supersonic expansion and injection of water. *Chemical Engineering Science* 2011,66:1622-1630.
98. Goertz V, Korp D, Al-Hasan N, Giglmaier M, Nirschl H. Experimental study of gas-dynamically induced nanoparticle synthesis by use of adapted sampling probes. *Chemical Engineering and Processing: Process Intensification* 2011,50:836-845.
99. Menter FR, Egorov Y. A scale adaptive simulation model using two-equation models. In: *AIAA*; 2005. pp. 83624-83624.
100. Bhaskaran KA, Roth P. The shock tube as wave reactor for kinetic studies and material systems. *Progress in Energy and Combustion Science* 2002,28:151-192.
101. Cancino LR. Development and Application of Detailed Chemical Kinetics Mechanisms for Ethanol and Ethanol Containing Hydrocarbon Fuels: Federal University of Santa Catarina; 2009.



102. Rathakrishnan E. *Applied Gas Dynamics*. Singapore: John Wiley & Sons (Asia) Pte Ltd; 2010.
103. Zel'dovich IAB. *Physics of shock waves and high-temperature hydrodynamic phenomena*: Dover Publications; 2002.
104. Carrington T. Electronic Quenching of OH ($^2\Sigma^+$) in Flames and its Significance in the Interpretation of Rotational Relaxation. *The Journal of Chemical Physics*; 1959,30: 1087-1095.
105. Kaskan W.E. Abnormal Excitation of OH in H₂/O₂/N₂ Flames. *The Journal of Chemical Physics*; 1959, 31: 944-956.
106. Hidaka, Y, Takahashi S, Kawano H, Suga M, Gardiner C, Shock-tube measurement of the rate constant for excited hydroxyl(A₂SIGMA.+) formation in the hydrogen-oxygen reaction. *The Journal of Physical Chemistry*; 1982, 86: 1429-1433.
107. Hall JM, Petersen EL, An optimized kinetics model for OH chemiluminescence at high temperatures and atmospheric pressures. *International Journal of Chemical Kinetics*; 2006, 38: 714-724.
108. Durrstein SH, Aghsaei M, Jerig L, Fikri M, Schulz C. A shock tube with a high-repetition-rate time-of-flight mass spectrometer for investigations of complex reaction systems. *Review of Scientific Instruments* 2011,82:084103-084107.
109. Hall JM, Petersen EL. An optimized kinetics model for OH chemiluminescence at high temperatures and atmospheric pressures. *International Journal of Chemical Kinetics* 2006,38:714-724.
110. Tamura M, Berg PA, Harrington JE, Luque J, Jeffries JB, Smith GP, Crosley DR. Collisional Quenching of CH(A), OH(A), and NO(A) in Low Pressure Hydrocarbon Flames. *Combustion and Flame* 1998,114:502-514.
111. Igra O, Ben-Dor G, Elperin T, Lifshitz A. *Handbook of shock waves*: Academic Press; 2001.
112. Guilhaus M, Mlynski V, Selby D. Perfect Timing: Time-of-flight Mass Spectrometry†. *Rapid Communications in Mass Spectrometry* 1997,11:951-962.
113. Grotheer H-H, Pokorny H, Barth K-L, Thierley M, Aigner M. Mass spectrometry up to 1 million mass units for the simultaneous detection of primary soot and of soot precursors (nanoparticles) in flames. *Chemosphere* 2004,57:1335-1342.
114. Faccinetto A. High sensitivity detection of Polycyclic Aromatic Hydrocarbons desorbed from soot particles using Laser Desorption/Laser Ionisation/Time-Of-Flight Mass Spectrometry. An approach for studying the soot growth process in flames: Université Lille 1; 2009.



115. Cotter RJ. Time-of-flight mass spectrometry for the structural analysis of biological molecules. *Analytical Chemistry* 1992,64:1027A-1039A.
116. Mamyrin BA. Time-of-flight mass spectrometry (concepts, achievements, and prospects). *International Journal of Mass Spectrometry* 2001,206:251-266.
117. Aghsaee M, Abdali A, Duerrstein SH, Schulz C. A shock-tube with high-repetition-rate time-of-flight mass spectrometry for the study of complex reaction systems. In: *28th International Symposium on Shock Waves*. Manchester; 2011.
118. Kern RD, Singh HJ, Wu CH. Thermal decomposition of 1,2 butadiene. *International Journal of Chemical Kinetics* 1988,20:731-747.
119. Singh HJ, Kern RD. Pyrolysis of benzene behind reflected shock waves. *Combustion and Flame* 1983,54:49-59.
120. Kiefer JH, Zhang Q, Kern RD, Yao J, Jursic B. Pyrolyses of Aromatic Azines: Pyrazine, Pyrimidine, and Pyridine. *The Journal of Physical Chemistry A* 1997,101:7061-7073.
121. Kronemayer H, Ifeacho P, Hecht C, Dreier T, Wiggers H, Schulz C. Gas-temperature imaging in a low-pressure flame reactor for nano-particle synthesis with multi-line NO-LIF thermometry. *Applied Physics B: Lasers and Optics* 2007,88:373-377.
122. Kronemayer H. Laser-based temperature diagnostics in practical combustion systems: Ruprecht-Karls-Universität Heidelberg; 2007.
123. Gilmore FR. *Potential energy curves for N₂, NO, O₂, and corresponding ions*: Rand Corporation; 1966.
124. Bessler WG, Schulz C, Sick V, Daily JW. A versatile modeling tool for nitric oxide LIF spectra. In: *Third Joint Meeting of the U.S. Sections of The Combustion Institute*. Chicago; 2003.
125. Ifeacho P. Semi-conducting metal oxide nanoparticles from a lowpressure premixed H₂/O₂/Ar flame: Synthesis and Characterization: Universität Duisburg-Essen; 2008.
126. Stein SE. Mass Spectra. In: *NIST Chemistry WebBook, NIST Standard Reference Database Number 69*, Eds. P.J. Linstrom and W.G. Mallard. Gaithersburg MD, 20899: National Institute of Standards and Technology.
127. Dürrstein S. Untersuchung komplexer Reaktionsmechanismen durch zeitaufgelöste Massenspektrometrie hinter reflektierten Stoßwellen [PhD]. Karlsruhe: Karlsruhe Institute of Technology (KIT); 2009.
128. Abdali A, Fikri M, Wiggers H, Schulz C. Shock-tube study of the ignition delay time of tetraethoxysilane (TEOS). In: *Shock Waves*. Edited by Hannemann K, Seiler F: Springer Berlin Heidelberg; 2009. pp. 781-785.



129. Basner R, Foest R, Schmidt M, Becker K, Deutsch H. Absolute total and partial electron impact ionization cross sections of hexamethyldisiloxane. *International Journal of Mass Spectrometry* 1998,176:245-252.
130. P. Smith DMG, Michael Frenklach, Nigel W. Moriarty, Boris Eiteneer, Mikhail Goldenberg, C. Thomas Bowman, Ronald K. Hanson, Soonho Song, William C. Gardiner, Jr., Vitali V. Lissianski, and Zhiwei Qin GRI mechanism V 3.0. In: http://www.me.berkeley.edu/gri_mech/; 2011.
131. Aghsaee M, Dürrstein SH, Böhm H, Fikri M, Schulz C. Influence of Molecular Hydrogen on Acetylene Pyrolysis: Experiment and Modeling *Combustion and Flame*, Submitted.
132. Mick HJ, Matsui H, Roth P. High-temperature kinetics of silicon atom oxidation by nitric oxide based on silicon, nitrogen, and oxygen atom measurements. *The Journal of Physical Chemistry* 1993,97:6839-6842.
133. Matheis J. Numerische Sensibilitätsanalyse eines Mikrowellenplasmareaktors zur Synthese von Nanopartikeln. Munich: TU Munich; 2011.
134. Knipping J, Wiggers H, Rellinghaus B, Roth P, Konjhodzic D, Meier C. Synthesis of High Purity Silicon Nanoparticles in a Low Pressure Microwave Reactor. *Journal of Nanoscience and Nanotechnology* 2004,4:1039-1044.
135. Vemury S, Pratsinis SE. Corona-assisted flame synthesis of ultrafine titania particles. *Applied Physic Letters* 1995,66:3275 - 3277.
136. Cleaver JAS, Tyrrell JWG, The Influence of Relative Humidity on Particle Adhesion - a Review of Previous Work and the Anomalous Behaviour of Soda-lime Glass. *Kona*; 2004,22:9-22.
137. Cleaver JAS, Tyrrell JWG. The Influence of Relative Humidity on Particle Adhesion – a Review of Previous Work and the Anomalous Behaviour of Soda-lime Glass. *Kona*; 2004,22:9-22.
138. Kaliszewski MS and Heuer HA, Alcohol Interaction with Zirconia Powders. *Journal of the American Ceramic Society*; 1990, 73: 1504-1509.
139. Milekhin A, Friedrich M, Hiller K, Wiemer M, Gessner T, Zahn DRT. Infrared study of Si surfaces and buried interfaces. In: AVS; 1999, 1733-1737.
140. Gondorf A. Optische Eigenschaften von Silizium-Nanopartikeln [Diplomarbeit]. Duisburg: Universität Duisburg-Essen; 2006.
141. Lee KW, Chen J, Gieseke JA. Log-Normally Preserving Size Distribution for Brownian Coagulation in the Free-Molecule Regime. *Aerosol Science and Technology* 1984,3:53-62.



142. Heine MC, Pratsinis SE. Polydispersity of primary particles in agglomerates made by coagulation and sintering. *Journal of Aerosol Science* 2007,38:17-38.
143. Friedlander SK, Wang CS. The self-preserving particle size distribution for coagulation by brownian motion. *Journal of Colloid and Interface Science* 1966,22:126-132.
144. Lai FS, Friedlander SK, Pich J, Hidy GM. The self-preserving particle size distribution for Brownian coagulation in the free-molecule regime. *Journal of Colloid and Interface Science* 1972,39:395-405.

9. List of own publications

Peer reviewed articles

- **A. Abdali**, A. Faccinetto, H. Orthner, H. Wiggers, C. Schulz, “*Study of silica particle growth in a low pressure premixed H₂/O₂/Ar flame reactor using tetraethoxysilane and hexamethyldisiloxane*“, Journal of Aerosol Science, In preparation.
- **A. Abdali**, M. Fikri, H. Orthner, H. Wiggers, C. Schulz, “*Ignition delay times of shock-heated tetraethoxysilane, hexamethyldisiloxane, and titaniumtetrakispropoxide*“, Chemical Physics Letters, accepted.
- Y. Sehlleier, **A. Abdali**, S. Schnurre, H. Wiggers, C. Schulz, “*Surface functionalization of gas-phase synthesized silica nanoparticles for enhancing stability of dispersions*“, Journal of Nanoparticle Research, submitted.
- C. Hecht, **A. Abdali**, T. Dreier, C. Schulz, „*Gas-temperature imaging in a microwave-plasma nanoparticle-synthesis reactor using multi-line NO-LIF thermometry*“, Zeitschrift für Physikalische Chemie 225 (2011), p. 1225-1235.
- **A. Abdali**, B. Moritz, A. Gupta, H. Wiggers, C. Schulz „*Hybrid microwave-plasma hot-wall reactor for synthesis of silica nanoparticles under well-controlled conditions*“, Journal of Optoelectronics and Advanced Materials 12 (2010) 440.

Conference articles

- Y. H. Sehlleier, **A. Abdali**, T. Hülser, H. Wiggers and C. Schulz, “*Functionalization of SiO₂ nanoparticles and their superhydrophobic surface coating*“, NanoFormulation, (2012) 113 – 120.
- M. Aghsaee, **A. Abdali**, S.H. Dürrstein, C. Schulz, „*A shock-tube with high-repetition-rate time-of-flight mass spectrometry for the study of complex reaction systems*“, 28th Int. Symp. Shock Waves, (2012) 191-196.
- **A. Abdali**, B. Moritz, H. Wiggers, C. Schulz, “*Gas-phase synthesis of silica nanoparticles in a hybrid microwave-plasma hot-wall reactor*“, proceeding paper by Nanotech 1 (2010) 334.
- **A. Abdali**, M. Fikri, H. Wiggers, C. Schulz „*Shock-tube study of the ignition of tetraethoxysilane (TEOS) and subsequent SiO₂ particle formation*“, 26th Int. Symp. Shock Waves 1 (2009) 781 – 785.



- Grzona, A., **A. Abdali** et al., *Gas-phase synthesis of non-agglomerated nanoparticles by fast gasdynamic heating and cooling*, in *Shock Waves*, K. Hannemann and F. Seiler, Editors. 2009, Springer Berlin Heidelberg. p. 857-862.



Name	Ali Abdali
Date of Birth	09.03.1976
Place of Birth	Muharraq, Bahrain
Nationality	Bahraini
E-mail:	ali.abdali@uni-due.de

Professional record

05/2012-present	Process Engineer, EVONIK Industries AG, Hanau
01/2006 – 12/2011	Research Associate at the Institute for Combustion and Gasdynamics
09/2005 – 12/2005	Process Engineer, H.C. Starck GmbH, Goslar

Education

10/1998 – 04/2005	Dipl.-Ing. in Chemical Engineering at the Technical University of Clausthal
02/1995 – 07/1997	Chemical Engineering at the University of Bahrain
07/1994	Secondary School General Certificate, Bahrain



